Cavity quantum electrodynamics with quantum dots in microcavities

Morten P. Bakker

Cavity quantum electrodynamics with quantum dots in microcavities

---

PROEFSCHRIFT

ter verkrijging van
de graad van Doctor aan de Universiteit Leiden,
op gezag van Rector Magnificus prof. mr. C. J. J. M. Stolker,
volgens besluit van het College voor Promoties
te verdedigen op woensdag 17 juni 2015
klokke 15:00 uur

door

Morten Peter Bakker

geboren te Groningen, Nederland
in 1987

Promotor:

Prof. dr. D. Bouwmeester	Universiteit Leiden en University of California Santa Barbara

Co-promotor:

Dr. M. P. van Exter	Universiteit Leiden

Promotiecommissie:

Prof. dr. B. D. Gerardot	Heriot-Watt University, Edinburgh, UK
Prof. dr. A. Fiore	Universiteit Eindhoven
Dr. M. Blaauboer	Universiteit Delft
Prof. dr. M. A. G. J. Orrit	Universiteit Leiden
Prof. dr. E. R. Eliel	Universiteit Leiden
Dr. M. J. A. de Dood	Universiteit Leiden

The research reported in this thesis was conducted at the 'Leids Instituut voor Onderzoek in de Natuurkunde' (LION). This work is part of the research program of the Foundation for Fundamental Research on Matter (FOM), which is part of the Netherlands Organization for Scientific Research (NWO).

An electronic version of this dissertation is available at the Leiden University Repository (https://openaccess.leidenuniv.nl).

Casimir PhD series, Delft-Leiden, 2015-15

ISBN: 978-90-8593-224-6

"If it bleeds, we can kill it."

Arnold Schwarzenegger

"We are all just prisoners here, of our own device."

Don Henley

Voor mijn ouders en Lene.

Contents

Introduction

In this introductory chapter, we will motivate our work and discuss future applications of cavity quantum electrodynamics (QED). We will also provide a theoretical description of cavity QED, including the important concepts of dressed states and avoided crossing. Next, we will compare various cavity QED systems, first the non-semiconductor based systems and then various semiconductor cavity architectures, and motivate the choice for our system. We conclude with an overview of the chapters in this thesis and the relationship between them.

1.1 Towards deterministic spin–photon entanglement

As a general motivation for the work presented in this thesis, we will present a scheme on how to generate deterministic spin–photon entanglement using cavity quantum electrodynamics (QED). In this thesis significant progress will be presented towards realizing this experiment, which could form the basis of much future research and several novel applications.

Cavity QED deals with the interaction between light confined in a cavity, and a single atom or other emitter. One manifestation is that a transmittive cavity can be turned into a reflective one by coupling a single atomic dipole transition to it [1–3]. We aim to use this property to create entanglement between light and matter.

Figure 1.1 shows the generic geometry of a cavity together with an atom that has two ground states that couple to dipole transitions of different energy and/or polarization. These two states can be for example the hyperfine split states of an atom, or the Zeeman split spin states of a singly charged quantum dot (QD). We want to realize the latter and will thus refer to these ground states as the spin up $|\uparrow\rangle$ and spin down $|\downarrow\rangle$ states. Depending on the spin state, the incoming photon will couple to an optical transition or not, and subsequently will be reflected or transmitted. If the atom is now prepared in a superposition state $|\Psi\rangle_{atom} = \alpha\,|\uparrow\rangle + \beta\,|\downarrow\rangle$ with $|\alpha|^2 + |\beta|^2 = 1$, the cavity mediated interaction results in an entangled output state $|\Psi\rangle_{out}$ between the photon and the atom:

$$|\Psi\rangle_{in} = |\phi\rangle_{photon} \otimes |\Psi\rangle_{atom} \quad \rightarrow \quad |\Psi\rangle_{out} = \alpha\,|R,\uparrow\rangle + \beta\,|T,\downarrow\rangle\,, \tag{1.1}$$

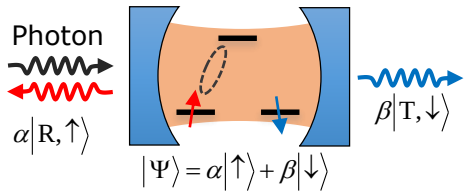

Figure 1.1: Scheme for the creation of deterministic spin–photon entanglement. The atom (or QD) is prepared in a superposition of two ground states, which for a QD are the spin up/down states of a confined single-charge. An incident photon, with a frequency and polarization that only couples to one of the two transitions, is subsequently reflected and transmitted depending on the spin state. This operation creates entanglement between the spin state and the spatial degree of freedom of the photon.

where $|\phi\rangle_{photon}$ denotes the photon being initially in the input port, and $|R/T\rangle$ denotes the photon being in the reflection/transmission mode. This process thus creates deterministic spin-photon entanglement. The entanglement protocol can be verified by interfering, for example, the two possible photon paths on a beamsplitter; the output port of the photon will then depend on the value of α and β.

Light-matter entanglement has been realized using atoms [4], and solid–state spin systems such as NV-centers [5] and QDs [6, 7]. In these systems the (artificial) atom is first excited and then relaxes to one of the two spin–split ground states. As these ground states are typically non-degenerate the polarization as well as the frequency of the emitted photon becomes entangled with the ground-state spin. This implies that either the polarization or the frequency information of the photon needs to be 'erased' in order to eliminate the 'which-path' information, and this postselection operation limits the success probability. Postselection on spontaneously emitted photons can be used to entangle two qubits at a distance [8, 9], but as these protocols are of a probabilistic nature many experiments need to be performed in order to select the desired outcome. Nevertheless, experiments have been demonstrated that remotely entangle two atoms [10], two NV-centers [11], or even teleport a quantum state [12]. A deterministic protocol however, as the one we describe here, will increase the success rate and is especially favorable, if needed, for further scaling up to multipartite entangled qubit systems.

The work presented in this thesis has a dual motivation. On the one hand, it is driven by curiosity whether the intriguing effects predicted by quantum mechanics can be realized in a (solid-state) system in the lab. These experiments can form a fundamental test of textbook physics on the interaction between atoms and single light quanta, and non-local quantum entanglement.

On the other hand, our system shows promise for new applications and technologies based on the principles of quantum mechanics. We will discuss these applications in the next session.

1.2 Applications of cavity QED

Various applications of cavity QED can be envisioned, which motivates many research groups both inside and outside of academia to work in this interesting field. In the following we will mention some applications, even though some may seem to lie far ahead in the future.

1.2.1 Quantum information applications

Many quantum information processing (QIP) applications can be realized that rely on (deterministic) spin-photon entanglement. Schemes to entangle a single spin with a single photon can be extended to entangle multiple spins, and to form a quantum network [13, 14]. Such a quantum network would consist of spins in cavities where quantum states are stored and manipulated, which are connected by optical channels that distribute quantum information.

A quantum network enables to perform cluster state quantum computing [9, 15, 16]. The creation of deterministic entanglement can also be used to realize a quantum repeater, which is essential to deal with losses in long-distance transport of quantum information via photons possible [8, 17, 18]. Finally, it could be used for quantum metrology [19], and for example enhance the sensitivity of gravitational wave detectors [20]

1.2.2 Non-classical light sources

A cavity QED system can be used to generate non-classical states of light, which could realize a whole range of technologies that make use of the quantum mechanical properties of photons [21]. Quantum cryptography can for example be realized with single-photon [22], or entangled-photon sources [23]. See for a review Ref. [24]. Single-photon sources and detectors, and linear optical networks can make photonic linear quantum computation possible [25]. A recent proposal describes how a cavity quantum electrodynamics scheme can in principle be used to realize an emitter of so-called N-photon bundles [26]. These could be used to create so-called NOON states [27], and for quantum lithography and metrology [28].

A cavity with an emitter coupled to it can ensure the efficient generation and collection of such (quantum) light. For practical applications an electrically driven room temperature cavity QED system would be ideal, but has not yet been realized. Significant progress has been realized with semiconductor QD systems, albeit limited to cryogenic temperatures. Some examples include

an electrically driven single-photon source with QDs in a p-i-n junction [29], electrically driven single-photon emission from a QD-micropillar system [30], optically pumped emission of entangled photon pairs through the biexciton decay of a neutral QD [31], and an ultrabright source of entangled photon pairs using a bimodal photonic molecule consisting of two coupled microcavities [32].

1.2.3 Optical interconnects

Optical interconnects aim to combine electronics and photonics in the same device. They are of great interest, among others because the high frequency transfer of signals is much more energy consuming for electrical signals compared to optical signals [33, 34]. Converting an electrical signal into an optical signal, and vice versa, relies on strong light-matter interactions. For this purpose cavity QED could be of interest, as it enables optical non-linearities at small photon numbers. Large-scale applications probably require a room temperature on-chip system, most likely one that is compatible with the current industry standard of Silicon photonics technology.

1.3 Theory of cavity quantum electrodynamics

The research field of cavity QED deals with the interaction between light confined in a cavity and matter, typically in the form of atoms or 'artificial' atoms like quantum dots. In section 1.3.1, we will first introduce the semiclassical approach for an atom in a cavity, a description that perfectly suffices throughout most of this thesis. In section 1.3.2, we will discuss the Jaynes-Cummings model, which incorporates the quantum nature of photons and the atom/emitter. Two important concepts of this model are the occurrence of dressed states and the avoided crossing. We will introduce these in section 1.3.3 and show how they appear in our measurement results.

1.3.1 Semiclassical approach of a two-level atom in a cavity

A schematic picture of a two-level atom in a Fabry-Perot type cavity is shown in Fig. 1.2. The cavity has an in-coupling efficiency η, equal mirrors with an intensity loss rate κ_m through each mirror, and an absorption/scattering loss rate κ_s. The two level atom is introduced as a dielectric medium with a normalized electric susceptibility proportional to $2C/(1-i\Delta')$, where $\Delta' = (\omega - \omega_a)/\gamma$ is the difference between the laser and the atom angular frequency relative to the atom dephasing rate γ. The cooperativity C can be intuitively seen as the ratio between the atom absorption rate, and a function of the total absorption and loss rate of the cavity. Following the standard approach of calculating the transmission amplitude of a Fabry-Perot

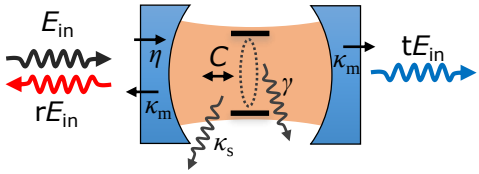

Figure 1.2: Schematic picture of a two-level atom in a cavity. An incoming photon with electric field strength E_{in} is reflected and transmitted with relative amplitudes r and t, respectively. The cavity has an incoupling efficiency η, mirrors with equal loss rates κ_m and an internal loss rate κ_s. The two-level system has a cooperativity C and a dephasing rate γ.

cavity with a dielectric medium, we find:

$$t = \eta \frac{1}{1 - i\Delta + \frac{2C}{1-i\Delta'}}, \tag{1.2}$$

where $\Delta = 2(\omega - \omega_c)/\kappa$ is the difference between the laser and cavity angular frequencies divided by the total cavity decay rate $\kappa = 2\kappa_m + \kappa_s$. The total transmission is now given by $T = |t|^2$ and the reflectivity is given by $R = |1 - t|^2$.

This model describes the time-averaged optical properties of the system in the low intensity limit (less than 1 photon per cavity lifetime), where no single emitter/absorber effects play a role. It can be easily expanded for multi-level atomic systems with different polarized transitions, as will be described in Ch. 6.

1.3.2 Jaynes-Cummings model

The Jaynes-Cummings model was introduced in 1963 by Edwin Jaynes and Fred Cummings [35]. Neglecting the vacuum energy and losses, and applying the rotating wave approximation, they described the Hamiltonian of a two-level atom coupled to a cavity by:

$$\begin{aligned} H &= H_{field} + H_{atom} + H_{interaction} \\ &= \hbar\omega_c a^\dagger a + \hbar\omega_a \sigma_z^\dagger \sigma_z + \hbar g(a^\dagger \sigma_- + \sigma_+ a), \end{aligned} \tag{1.3}$$

where $a(a^\dagger)$ and $\sigma_-(\sigma_+)$ are lowering (raising) operators of the optical field and atom, respectively. The coupling strength g between the cavity and atom is given by: $g = g_0\sqrt{n+1}$, where n are the number of photons in the cavity and $g_0 = \sqrt{C\kappa\gamma}$. The case $n = 0$ corresponds to the situation where the system contains one excitation, either in the cavity or in the atom.

We now consider a single excitation of the system in the case where the cavity and atom are resonant $\omega = \omega_c = \omega_a$ and no losses of the system are taken

into account yet. For the uncoupled case ($g_0 = 0$), the system can be described by the degenerate energy eigenstates $|\Psi_+\rangle = |e\rangle\,|n\rangle$ and $|\Psi_-\rangle = |g\rangle\,|n+1\rangle$ that describe either an excitation in the cavity field or in the atom. Here $|g\rangle$ and $|e\rangle$ denote the atom being in the ground and excited state, respectively, and $|n\rangle$ denotes the number of photons in the cavity. However, when the system is coupled, the eigenstates $|\Psi_\pm\rangle$ with eigenenergies $E^n_\pm$ are given by:

$$|\Psi_\pm\rangle = \frac{1}{\sqrt{2}}(|e,n\rangle \pm |g,n+1\rangle), \qquad E^n_\pm = (n+1)\hbar\omega \pm \hbar g_0\sqrt{n+1}. \tag{1.4}$$

These so-called dressed states contain simultaneously an excitation in the optical field and in the atom. The phenomenon that the bare states are split into dressed states with energy splittings $\Delta E^n = E^n_+ - E^n_- = 2\hbar g_0\sqrt{n+1}$, is referred to as the Jaynes-Cummings ladder. When the detuning between the cavity and atom is gradually decreased, a gradual transition from bare states, which would cross in energy at zero detuning, to dressed states, which are split in energy, occurs. In the next session we will demonstrate how this avoided crossing appears in our system.

In order to take losses into account, the system can be generically described using the Heisenberg picture, where the equation of motion of any operator Θ becomes:

$$\frac{d\Theta}{dt} = -\frac{i}{\hbar}[\Theta, H] + L(\Theta). \tag{1.5}$$

Here $L(\Theta)$ is the Markovian loss operator. The loss rates of the cavity and atom can again be introduced as κ and γ. The solution of the energy eigenstates $E^n_\pm$ of the coupled system, with angular frequency $\omega^n_\pm$ and dephasing rate $\Gamma^n_\pm$, is given by:

$$E^n_\pm = \hbar\omega^n_\pm - i\Gamma^n_\pm = \frac{1}{2}((2n+1)\hbar\omega_c + \hbar\omega_a) - \frac{i}{2}((2n+1)\kappa + \gamma) \pm\sqrt{(n+1)g^2 + \frac{1}{4}[(\hbar\omega_c - \hbar\omega_a) - i(\kappa-\gamma)]^2}. \tag{1.6}$$

This equation shows that in the low excitation intensity limit $n = 0$ for $g > \gamma, \kappa$ and $\omega_c = \omega_a$, the dephasing rate Γ becomes approximately equal to the average of κ and γ, which demonstrates the mixing of the cavity and atom character for the dressed states. For $n > 0$ the bare states contain either $n+1$ photons in the cavity, and the total decay rate equals $(n+1)\kappa$, or the bare state contains n photons in the cavity and one excitation of the atom, and the decay rate equals $n\kappa + \gamma$. Subsequently, for $g > \gamma, \kappa$ the dephasing rate of the dressed states are approximately the average of these decay rates $\Gamma \approx \frac{1}{2}((2n+1)\kappa+\gamma)$

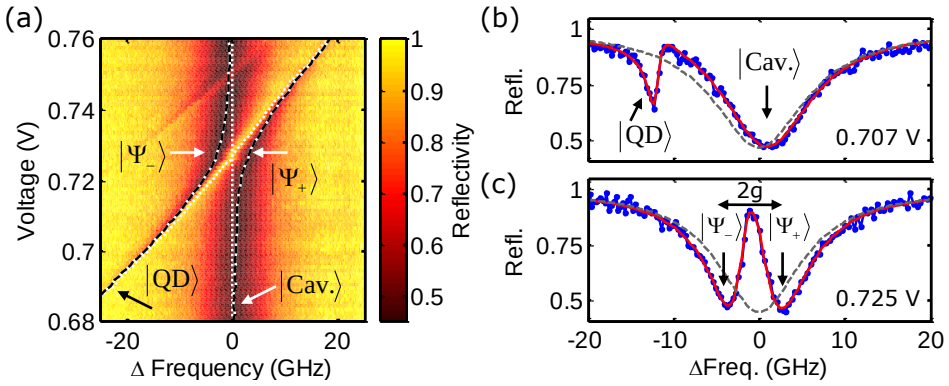

Figure 1.3: Signatures of dressed states and avoided crossing. (a) shows a reflectivity color map as function of the frequency detuning of a laser, scanned across the QD-cavity system, and the bias voltage. White dashed lines are QD and cavity frequencies, black-white lines are the frequencies of the two dressed states. (b,c): cross-sections of the reflectivity scans when the QD is detuned (b) and when the QD is in resonance (c). Grey dashed lines show the empty cavity resonance.

Finally, the input-output formalism can be used to calculate the reflection and transmission [36–39]. In the low excitation intensity limit, this yields the same results as for the semiclassical model. For larger excitation intensities calculating the reflectivity and transmittivity spectrum becomes non-trivial as the input state is a superposition of Fock states, and numerical methods such as provided by the Quantum Optics toolbox can be used [40].

In the literature two regimes are typically defined:

- Intermediate coupling regime, also called weak coupling or Purcell regime. This regime is defined as $\kappa > g > \gamma$. The Purcell effect, the enhancement of the spontaneous emission rate, is associated with this regime.
- Strong coupling regime, for $g > \gamma, \kappa$. Coherent oscillations of the cavity and atom excitation take place before light leaks out of the cavity.

1.3.3 Dressed states and avoided crossing

In this subsection we will demonstrate how dressed states and the avoided crossing are visible in our measurements. Low intensity ($P_{in} = 1$ pW) reflectivity measurements, such that the system contains maximally one excitation ($n = 0$), are presented in Fig. 1.3. In these scans a QD transition is tuned through the (stationary) cavity resonance, as function of applied bias voltage through the DC Stark effect. A low reflectivity corresponds with the laser

being resonant with an optical transition, either from the cavity, the QD, or the dressed state. The white dashed lines in Fig. 1.3 (a) represent the QD and cavity resonance frequencies, and black-white dashed lines, which nicely follow the reflectivity minima, represent the frequencies of the dressed states.

When the QD and cavity resonances are detuned from one another, as is the case in Fig. 1.3 (b), the QD is characterized by a much narrower transition compared to the broad cavity resonance, since $\gamma \ll \kappa$. When the QD is now tuned towards the cavity resonance, an avoided crossing is visible in Fig. 1.3 (a) and the eigenstates are now the dressed states $|\Psi_-\rangle$ and $|\Psi_+\rangle$. Figure 1.3 (c) shows the reflectivity spectrum when the QD is tuned at the exact cavity resonance. The dressed states are now visible as resonances that have FWHMs that are the average of the FWHM of the QD and the cavity resonance; this clearly indicates the mixed character of these states. Since the splitting $2g/2\pi$ between the two states is larger than the $(2\gamma/2\pi)$ FWHM of the QD resonance, but is smaller than the $(\kappa/2\pi)$ FWHM of the cavity resonance, $\kappa > g > \gamma$ and the system is in the intermediate coupling regime.

1.4 Non-semiconductor cavity QED systems

In this section we will briefly introduce three cavity QED systems: (i) atoms in cavities, which historically were first studied, (ii) atoms in nanophotonic structures, which in recent years follows up on the previous system, and (iii) superconducting circuit QED, which is one approach for realizing cavity QED in the solid-state. In the next session we will continue with a description of the other solid-state approach, semiconductor based systems, which includes our system.

Atoms in cavities

A system with an atom in a cavity has been realized with microwave and optical cavities. Two examples are shown in Figure 1.4 (a,b). Atoms are placed in a Fabry-Perot cavity either by applying a transient flux of atoms, as is the case in the two examples, or by using an optical trap.

These systems enabled for the first time cavity QED and lots of other new physics to be explored. One early investigated manifestation is the change of the spontaneous emission rate of atoms; it can be accelerated when placed in a resonant cavity [49, 50], or it can be suppressed [51], depending on whether the local density of states is increased or decreased, respectively. A review of early work (already from the 80s) is provided by Ref. [52]. The experiments were extended to other ground-breaking work such as the non-destructive manipulation of single-atoms with photons (Wineland, [53]), and the manipulation of single-photons with atoms (Haroche, [54]). This and other work led

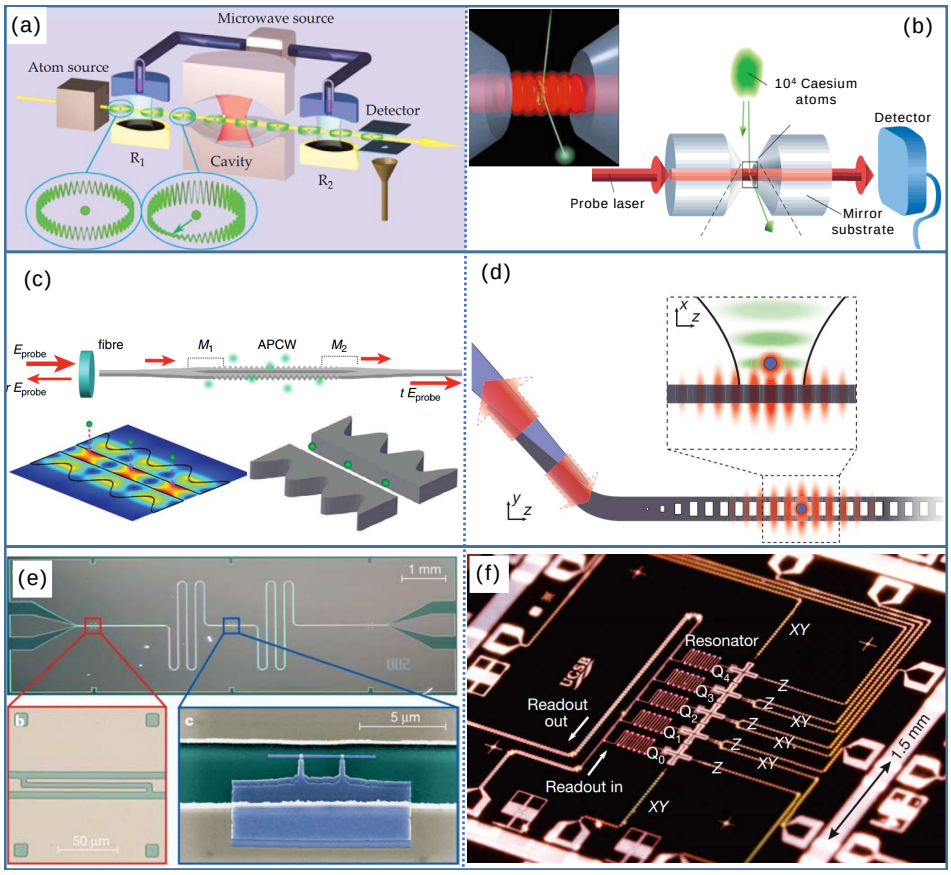

Figure 1.4: Examples of various non-semiconductor cavity QED systems. (a) Schematic illustration of atoms that are sent through a microwave cavity [41] and (b) an optical cavity [42, 43] (modified image). (c) Schematic image of atoms (green dots) in a fiber-coupled 'alligator' photonic crystal waveguide (APCW) [44]. (bottom-left) shows finite-element-method simulation of the guided mode electric field magnitude [45]. (d) Schematic drawing of a single-atom trapped in the evanescent field from a one-dimensional photonic crystal that is attached to a tapered optical fibre [46]. The inset shows the trapping lattice (green), formed by the interference of a set of optical tweezers and its reflection from the photonic crystal. (e) Electron microscope images of coplanar waveguide resonator (top) with capacitive couplers (bottom-left) to feed lines and (bottom-right) a Cooper pair box, which were used for the first circuit QED demonstration [47]. (f) Optical image of a device with 5 transmon qubits (Q_0-Q_4) coupled via nearest-neighbour coupling, controlled using the microwave/DC lines XY/Z, and read-out using resonators [48].

to the 2012 Noble prize being awarded to S. Haroche and D. Wineland "for ground-breaking experimental methods that enable measuring and manipulation of individual quantum systems". Other research highlights up to now include among others the realization of strong coupling with a single-atom in an optical cavity [55], demonstration of a quantum phase gate [56], and the demonstration of the photon blockade effect [1] by the Kimble group, and recent work in the Rempe-Ritter group, such as the realization of a single-atom quantum memory [57], the nondestructive detection of an optical photon [58], and a quantum gate between a flying optical photon and a single trapped atom [59].

In general, atoms are well suitable for quantum information applications as they are naturally identical and highly coherent, even though coherence times are typically limited to values on the order of ∼200 ms [60] due to electric or magnetic field = variations in the environment of the trapped atom. However, large and complex setups are required, for example combining complicated atom trap and optical cooling techniques. This is a major challenge for scaling these experiments further up to many distant qubit networks.

Atoms in nanophotonic structures

An interesting approach towards on-chip atom-photon manipulation is provided by trapping atoms in nanophotonic structures. Several systems have been realized, see Fig. 1.4 (c,d), such as an atom trapped in the evanescent field of a tapered optical nanofibre [61], an atom trapped in the guided mode of a double-beam photonic crystal waveguide [44, 45], and an atom trapped using an optical tweezer near a photonic structure [46, 62]. Some research highlights up to now include the realization of a quantum phase switch [46] and the all-optical routing of single photons by a one-atom switch controlled by a single-photon [63]. It is an emerging technology and promises many more great results in the near future.

Superconducting circuit QED

Superconducting circuits are one of the most promising candidates to form a qubit in a future quantum computer, as they combine on-chip integrability and scalability, electronic control, and ever increasing coherence times (see for a review [64–66]). Coupling these circuits to microwave photons confined to a resonator has proven to form an excellent platform for cavity (also called circuit) QED experiments. Figure 1.4 (e) shows the first system with which strong coupling was achieved. In a future quantum computer architecture, resonators will most likely have an important role, either to read-out individual qubits, or to create entanglement between separate qubits in the same

cavity [67]. A state-of-the-art system with 5 neighbouring qubits is shown in Fig. 1.4 (f). A drawback of superconducting circuits is that they require a working temperature of typically < 100 mK, and < 100 GHz qubit frequencies, which therefore restricts the system to microwave photons which require relative large system dimensions (many mm's).

1.5 Semiconductor cavity QED systems

Semiconductor systems are an attractive candidate for cavity QED as they promise scalability an on-chip integration. In this section, we will first mention some advantages and some of the main challenges. Next, we will present an overview of various cavity architectures. Based on the requirements for applications in quantum information processing, we will discuss the advantages and disadvantages of the several systems, and motivate the choice for our own particular system.

1.5.1 Advantages of semiconductor based cavity QED systems

A major motivation to work with semiconductor systems is that the semiconductor industry offers a well-developed 'toolbox' for nanophotonics, which promises scalable and on-chip integrated systems. Furthermore, compared to for example superconducting circuits, systems can be realized at optical frequencies. This offers a promise to be integrated with existing optical fiber communication technology, but it is also practical to work at optical frequencies in a lab.

Challenges

In order to enable quantum information processing applications, a semiconductor cavity QED system has to be realized with on the one hand coherent, identical qubits, and on the other hand a cavity that enables access to the intermediate or strong coupling regime, and a high in- and out-coupling efficiency. This has remained a major challenge for the various types of semiconductor systems, especially the necessity to combine these two requirements.

Qubits realized in III-V semiconductor materials, such as the InAs quantum dots in an $Al_xGa_{1-x}As$ structure which are the main topic in this thesis, have the disadvantage that they suffer from fast <10 μs decoherence due to coupling with nuclear spins and only operate at cryogenic temperatures due to coupling with phonons (see for various reviews for example [68–71]). The decoherence rate might seem fast, but picosecond coherent optical manipulation rates still enable many operations to be performed [72–74], and also 4 K cryogenic temperatures are nowadays easily accessible with many commercial cryostat systems. Various cavity architectures suitable for cavity QED can be

realized in III-V semiconductor material, as we will discuss in the next session.

Qubits have also been realized in various other nuclear spin-free semiconductor materials that do show long coherence times, even at room temperature. Room temperature coherence times have been reported of 40 μs for defect spins in SiC [75], more than 1 s for the nuclear spin of an ^{13}C atom coupled to an NV-centers in diamond [76], and even more than 39 minutes for ionized P donors in purified ^{28}Si [77]. Fabrication of cavities and scalable architectures in these materials offers great future promise, but has yet to be demonstrated for these highly coherent qubits.

1.5.2 Overview of semiconductor cavity architectures

Several semiconductor cavity architectures have been realized, of which several examples are shown in Fig. 1.5. We focus here on cavity systems realized with III-V semiconductor material ($Al_xGa_{1-x}As$) in which InAs self-assembled QDs are embedded, but some cavity architectures are also applicable for other materials. As every system has its advantages and disadvantages, we will compare them based on the requirements necessary for quantum information applications, which are:

- Charge control by externally applied potential in order to use singly charged QDs.
- Access to the intermediate or strong-coupling regime.
- Good cavity in- and out-coupling efficiencies.

Additionally, some system parameters that are not strictly crucial, but would still be of great benefit:

- Polarization degenerate cavity modes, to utilize the polarization degree of freedom of photons next to the spatial and frequency degree of freedom.
- Spatial and spectral alignment possibility, and/or the possibility to tune cavity or QD properties.

We will briefly introduce the various cavity designs and discuss these criteria.

(a) Photonic crystal cavities

Photonic crystal cavities consist of a defect in a 2D photonic crystal lattice, which is typically a $\lambda/2$ thick slab perforated with holes and underetched by removing a sacrificial layer. Light is typically confined to an extremely small volume $V < \lambda^3$, while still allowing reasonably high Q-factors of $\sim 10^4$. The top of Fig. 1.5 (a) shows an example of an H1 cavity (1 hole missing in a

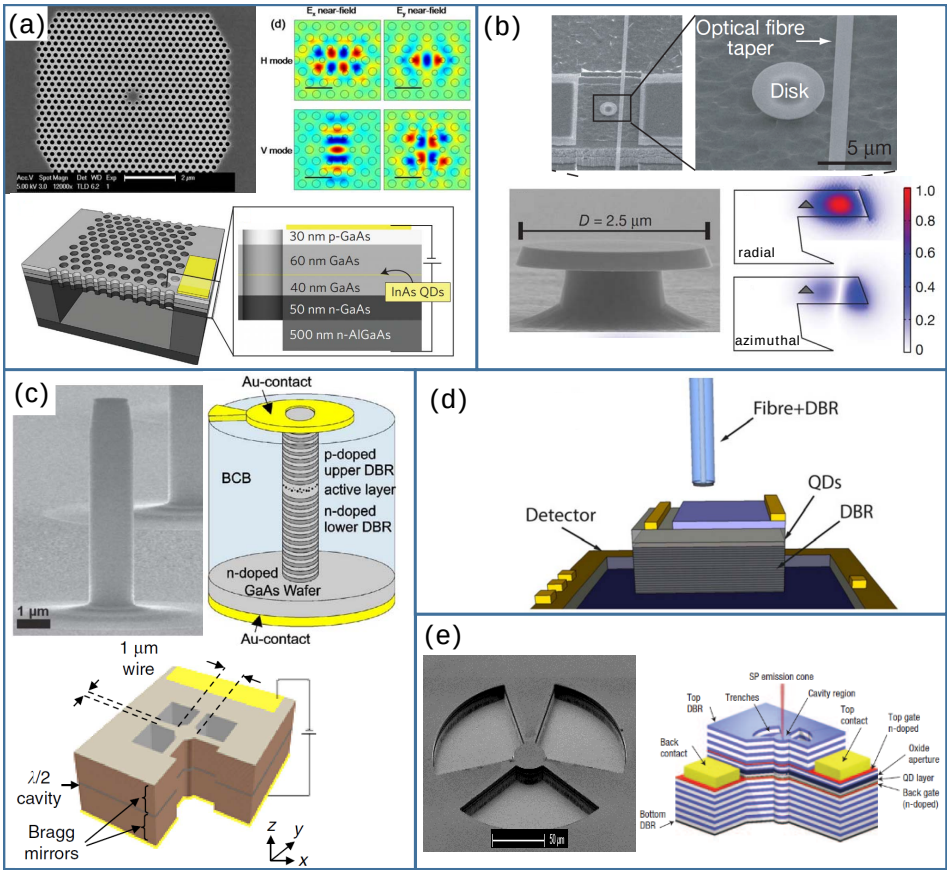

Figure 1.5: Various semiconductor cavity QED systems. (a) *Photonic crystal cavities*: (top-left) SEM image of far-field optimized H1 cavity, (top-right) FDTD simulated near-field electric field amplitudes [78], (bottom) illustration and layer thicknesses of an electrically contacted L3-type cavity [79]. (b) *Microdisk cavities*: SEM images of a microdisk coupled to a tapered fiber, and (bottom-right) finite-element-method simulations of the radial and azimuthal electric field components. (c) *Micropillar cavities*: SEM image of a freestanding MP (top-left) [80], and schematic images of electrically controlled MPs (top-right) [81] and (bottom) [82]. (d) *Combined fiber-tip and DBR Fabry-Perot cavity*, schematically shown [83]. (e) *Oxide-aperture micropillar cavity* (this thesis): (left) SEM image and (right) schematic drawing.

hexagonal lattice), of which the collection efficiency of the far-field has been optimized [78]. The bottom of Fig. 1.5 (a) shows an electrically contacted L3 cavity (3 missing holes in a row), which was used to study a single QD spin [79]. Properties of photonic crystal cavities are:

- Voltage contacts can be incorporated [79, 84].
- Strong coupling regime has been realized [85].
- The in- and out-coupling to external fields is typically poor (1-10%). On-chip coupling to waveguides is possible with near-unity efficiency [86].
- Polarization degeneracy is challenging to obtain, but can be done with AFM nano-oxidation [87].
- Deterministic spectral and spatial matching is possible [88][89]. In situ QD–cavity tuning can be performed by, among other techniques, temperature tuning [85], gas adsorption [88], and strain tuning [90].

(b) Microdisk resonator

A microdisk resonator as shown in Fig. 1.5 (b) consists of an etched torus that balances on a central post. First a mesa-type structure is produced through electron beam lithography and plasma dry etching, which is followed by a wet undercut etching step. Due to total internal reflection, a whispering gallery mode exists in the microresonator, which typically has a large $V \sim 100\lambda^3$ mode volume and very large Q-factor $Q \sim 10^6$. Coupling to external fields can be (in principle ideally) done via nearby waveguides, for example in the form of a tapered fiber. Advantages and disadvantages of microdisk resonators are:

- Voltage contacts are not possible.
- Strong coupling regime has been realized [3].
- In- and out-coupling can be performed on-chip to tapered fibers.
- Polarization control is not possible.
- Cavity tuning is possible for example through gas adsorption.

(c) Freestanding micropillar

Freestanding micropillars (MPs) consist of two distributed Bragg reflectors (DBRs) made from GaAs and $Al_xGa_{1-x}As$ (typically $x = 0.90$) that embed a λ-thick GaAs region containing QDs. A circular MP is then etched to define the transverse mode confinement. The top–left corner of Fig. 1.5 (c)

shows an example of a freestanding MP [80], which was used to demonstrate photon antibunching in the strong coupling regime. The other two figures show examples of electrically contacted MPs [81, 82]. Characteristics of micropillar devices are:

- Voltage contacts are challenging to realize [81, 82], and a deterministically singly–charged QD has yet to be realized.
- Strong coupling regime has been realized [91].
- In- and out-coupling to external fields is excellent.
- Polarization degeneracy can be achieved by controlling the micropillar shape with great accuracy [32].
- Deterministic spectral and spatial matching is possible [92]. Tuning can be performed by varying the temperature.

(d) DBR and fiber tip cavities

Figure 1.5 (d) shows a Fabry-Perot cavity consisting of a bottom DBR with a layer containing QDs on top of it, and a fiber tip on which a concave DBR has been coated. The spatial position of the cavity, and the length of the cavity (and thereby its resonance) are controlled by tuning the fiber tip position [83]. This cavity configuration holds promise to also realize strongly coupled system with materials that are not easily processed, for example NV-centers in diamond [93]. A major challenge is however the sub-nm mechanical stability that is required. Properties of DBR and fiber tip cavities are:

- Voltage contacts can be incorporated.
- Intermediate coupling regime has been achieved.
- In- and out-coupling efficiency can in principle be near-unity.
- Polarization degeneracy is limited by birefringence and non-perfect concave etching of the fiber tip.
- Deterministic spectral and spatial matching is possible.

(e) Oxide apertured micropillars

These cavities are the main subject of this thesis, and are depicted in Fig. 1.5 (e). The structure consists of two DBRs that embed a λ thick GaAs layer containing QDs in the center. Transverse mode confinement is provided by an oxide aperture, where the the large refractive index difference between the oxide ($n_{ox} \approx 1.5$) and unoxidized AlAs ($n_{AlAs} \approx 2.9$) leads to confinement in the unoxidized center of the micropillar.

We believe the oxide-apertured system is an excellent platform for QIP applications:

- Voltage contacts can be incorporated.
- Intermediate coupling regime achieved. Access to the strong coupling regime is partly limited by the relatively large mode volume (typically $\sim 10\lambda^3$).
- In- and out-coupling efficiencies can in principle be near-unity.
- Polarization degeneracy can be obtained [94–96].
- Deterministic spectral and spatial matching is not possible. Various tuning techniques can be used, such as temperature tuning, DC Stark shift tuning [97], and strain-tuning [94, 95].

To date, the research collaboration between UCSB (USA) and the Leiden University has been at the forefront in using this system as a platform for cavity QED, and we will briefly review several research highlights prior to the work presented in this thesis. Oxide apertured MPs are originally developed for vertical cavity laser applications (for example in the Larry Coldren group at UCSB), but were further developed to form high-quality factor microcavities by Stoltz *et al.* in 2005 [98]. In 2007, Strauf *et al.* developed a high-frequency single-photon source by embedding QDs in the cavity and implementing electrical gates [99]. The great potential for externally mode-matched cavity QED experiments with charge-controlled QDs was further demonstrated by Rakher *et al.* in 2009 [100]. Following this, techniques were developed to tune the cavity birefringence and at the same time tune QD transitions (Bonato *et al.*, 2009 [94], 2011 [95]) by applying laser induced surface defects.

Of the remaining challenges, two are addressed in this thesis and are to more reliably control the sample fabrication process, especially to fabricate the oxide aperture, and to further explore resonant spectroscopy of neutral and charged quantum dots coupled to a polarization degenerate microcavity in the intermediate coupling regime. Some of the remaining challenges, especially towards deterministic spin-photon entanglement, will be discussed in the final outlook Chapter.

1.6 Overview of this thesis

This thesis is organized in four sections: (i) an introductory section that provide a general overview of cavity QED (Chapter 1) and a more technical introduction to the setup, techniques and sample (Chapter 2), (ii) a section (Chapter 3-5) that is devoted to optimizing the oxide aperture, (iii) a section

(Chapter 6-8) on low-temperature cavity QED experiments, (iv) and finally an outlook (Chapter 9).

- In Chapter 2 we first introduce the magneto-optical cryostat setup, briefly explain the applied experimental techniques, the sample structure, and demonstrate quantum dot and sample characterization.

- In Chapter 3-5 we show our work on optimizing the oxide aperture; these chapters have a more engineering character. In Chapter 3 we first introduce a technique to monitor the formation of the oxide aperture in real time, as well as an efficient technique to characterize the samples at room temperature. These techniques are based on off-resonant and resonant reflectivity scans, respectively. For this purpose we developed a novel steam-oxidation furnace integrated with an optical viewport. In Chapter 4 we used the same setup and performed many successive oxidation steps on the same microcavity. We characterize the optical modes at room temperature after each oxidation step and demonstrate that this offers a precise technique to fine-tune the exact amount of oxidation and thereby the cavity mode properties. In Chapter 5 we show that by systematic variations of the size and shape of elliptical oxide apertures the polarization properties of the cavity modes can be controlled, and with this method polarization degenerate microcavities can be produced nearly deterministically.

- In Chapter 6-8 low-temperature cavity QED measurements with QDs coupled to a polarization degenerate microcavity are presented. In Chapter 6 we study both a neutral and a singly–charged QD through resonant reflection and transmission spectroscopy. We demonstrate a polarization resolved analysis that reveals coherent and incoherent dynamics, and introduce models that describe the various findings. In Chapter 7 we study a novel non-linear effect due to the cavity-enhanced feedback between a QD and a charge memory. At the origin lies the excitation of charges by the intracavity field, which are then trapped by the oxide aperture and which cause a blueshift of the QD. We then demonstrate how the cavity can be used as an accurate probe of the $\sim$ms timescale build-up and decay of these charges. In Chapter 8 we present a homodyne detection technique that enables to determine directly the coherence and phase of light that passes through a coupled QD-cavity system. We use this technique as a powerful tool to characterize coherent and incoherent QDs, to study quantum optics textbook physics of the coherent fraction

as function of laser intensity, and to demonstrate a quantum dot induced phase shift.

- In Chapter 9 we conclude with an outlook. During the time of this thesis an unique set of samples was developed with which many more experiments were explored. Furthermore, we will discuss some approaches to further develop coherent charged QDs that can be used for deterministic spin–photon entanglement.

Chapter 2

Experimental setup and sample characterization

In this chapter we will introduce the cryostat and discuss the optical techniques that were used during the low temperature experiments in Chapters 6-8. Next, the sample design and the various design parameters are discussed. Finally, we will discuss the quantum dot growth, energy level schemes and characterization.

2.1 Cryostat

There were 4 key requirements when designing and building-up the cryostat system: (i) have access to both reflection and transmission, as this is required for spatial spin-photon entanglement schemes, (iii) apply an in-plane magnetic field, necessary for spin preparation and manipulation, (iii) have optics outside of the cryostat, as this eases alignment and the micropillars have a small NA < 0.4, (iv) have a closed-cycle system in order to keep the sample cold for longer periods. In the following we will describe the setup that meets all these requirements.

The cryostat that we use is a custom-built *SHI-4XG-S* from Janis Research Co. Drawings of the cryostat and the cryostat mount are displayed in Fig. 2.1. It is a closed cycle exchange-gas vibration isolated cryostat system equiped with a Grifford-McMahon RDK-408D2 Sumitomo cold head, with 1 W cooling power at 4.2 K. It has a cool-down time of about 2 hours to reach the base temperature of 9 K. The 'snout' at the bottom of the cryostat, in which the sample is mounted, is custom-built and has two windows at both sides of the sample with a window–window distance of 19.1 mm and an outer width of 38.1 mm. This window–window distance enables objectives outside of the cryostat to be used at both sides of the sample with working distances of 20 mm, while the outer width of 3 cm makes it possible to place the 'snout' between the poles of an external electromagnet.

The cryostat is mounted on top of an electromagnet (Alpha Magnetics Model 4800 adjustable gap C-frame electromagnet) which, when operated at a maximum current $I_B = 50$ A (Delta Electronics SM45-70D power supply), can produce a maximum in-plane magnetic field of about 1 T at the sample. Vibration isolation is achieved by preventing any rigid mechanical contact

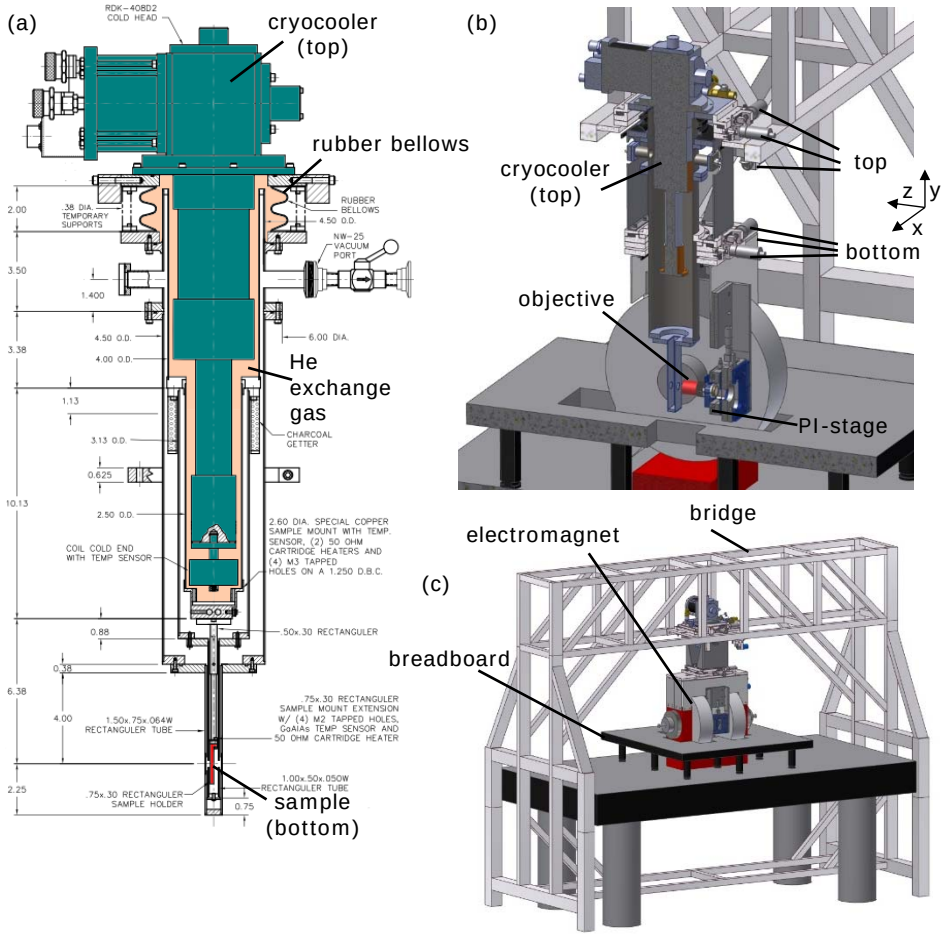

Figure 2.1: Drawings of the cryostat and the cryostat mount. (a) Technical cross-sectional drawing of the cryostat. The cryocooler (top part of the cryostat) and the sample (in the bottom part) are thermally connected with He exchange gas and mechanically only with a rubber bellows. (b) Cross-sectional drawing of a part of the cryostat mount. The cryocooler (top) and the sample (bottom) can be independently displaced in xyz-directions (tuning nobs indicated by lines). Only the front-side objective mounted on a piezo translation (PI) stage is shown. (c) Drawing of the entire cryostat mount, showing the 'bridge' to which the top part of the cryostat is attached, and the electromagnet, breadboard, and optical table on which the bottom part is mounted. [Courtesy of Gijs Verdoes and the Fine Mechanical Department].

between the cryocooler and the sample. Thermal contact is provided by He exchange gas between the cryocooler and the bottom part of the cryostat, which is at atmospheric pressure and enclosed by a flexible rubber bellows that reduces the transfer of vibrations. To reduce pressure changes of the He gas during every ~ 1 Hz cooling cycle, the exchange gas chamber is connected to a He balloon that can easily expand and contract. Furthermore, the bottom part of the cryostat, with the sample, is placed on top of the electromagnet and on the optical table to ensure damping, while the top part of the cryostat, with the cryocooler, is connected via a bridge to the floor of the lab. To study different parts of the sample easily, the bottom and top parts can be independently displaced over several mms in the xyz-directions.

Several low frequency Ph-Br cables are present in order to apply a DC voltage bias (typically 3 wires are used to apply a voltage to two micropillar arrays that share one common ground). A Keithley 2401 sourcemeter is used together with a 7 Hz low-pass filter to prevent high frequency noise to be transferred to the sample. High frequency type-SR coax cables are also present and might be used in future research. As the electromagnet heats up and thermally expands when operated at full power, the cryostat gets vertically displaced. In order to prevent severe misalignment, the frontside objective is mounted directly to the cryostat, such that it gets displaced synchronously. This way, the vertical micrometer-scale displacement takes place in the far field which is less critical than displacements in the near field. The objective is mounted on a PI P–733.3CL stage which enables precise positioning over a xyz $100 \times 100 \times 10$ μm range.

One major disadvantage of the system is that the cryocooler reaches a temperature of 3.5 K and causes He exchange gas to condense. Liquid He then makes a hydraulic contact between the cryocooler and the bottom part, causing vibrations at the sample. Also, He gas then has to be continuously added in order to keep the He exchange gas chamber at atmospheric pressure, otherwise the rubber bellows collapses and causes a rigid mechanical contact. In order to prevent all this the bottom part of the cryostat is kept at a temperature of 9.0 K (Lakeshore 336 temperature controller). In the future we wish to install a heater directly on the cryocooler and keep it at a temperature of 4.5-5 K, hoping that this enables lower sample temperatures. In the original cryostat design, the sample is connected via a relatively long vertical arm to the outside of the cryostat, which is sturdily mounted to the table, and is therefore relatively sensitive to vibrations. We were able to improve this significantly with a thermally isolating, plastic rigid spring between the coldfinger and the inner heatshield. In the future we are considering to

also add a rigid plastic spring between the inner heat shield and the outer heatshield, to further reduce vibrations.

2.2 Optical setup

The sample can be optically studied from two sides (reflection and transmission path) using two objectives (Mutitoyo, 20 mm working distance, 0.40 NA). Several types of experiments were performed throughout this thesis. Photoluminescence measurements and reflectivity measurements, either with a broadband light source or with single-wavelength 1064 nm laser, were performed with a relatively simple confocal setup and, for some experiments, were performed as function of position by spatially scanning the objective. In this section we will discuss four slightly more complicated experiments, namely with one resonant scanning laser, two resonant scanning lasers, one resonant laser and one off-resonant chopped laser, and interference measurements. We will briefly discuss these setups, that are schematically depicted in Fig. 2.2. All experiments are performed with a DAQ card (NI PCI-6259) that controls all the scanning lasers and reads out all the different photodetectors.

2.2.1 One resonant scanning laser

Measuring with one resonant scanning laser is the 'workhorse' technique and results are demonstrated in Chapters 6-8. Also, in order to quickly check whether there are interesting QDs coupled to a specific microcavity, scans with one laser are analyzed on an oscilloscope such that QDs can be viewed as function of bias voltage in 'real-time'.

The setup to perform scans with one resonant laser consists of two modular components, shown in Fig. 2.2 (a,b). The first part, Fig. 2.2 (a), serves to monitor the frequency and intensity of the scanning laser and to set the intensity. A laser (New Focus, Velocity, model 6319, 930-945 nm) is scanned by applying an external voltage. Using beamsplitters part of the laser light is directed to two Fabry-Perot interferometers (FP), with photodetectors (PD) to monitor the transmission, and to a PD to monitor the intensity for normalization purposes. A fine FP (free spectral range 250 MHz , finesse ~ 6) is used to accurately calibrate the frequency scale as function of the external voltage applied to the laser, while the coarse FP (free spectral range 4 GHz, finesse ~ 250) is used to overlay forward and backward frequency scans. A variable attenuation is applied and the light is coupled into a fiber coupler.

The second part of the optical setup, Fig. 2.2 (b), is used to couple the laser into the cavity mode and monitor the reflection and transmission intensities. The light is first coupled out of a fiber coupler, and is coupled in and out of the cavity using free-space optics. The transmitted and reflected light is coupled

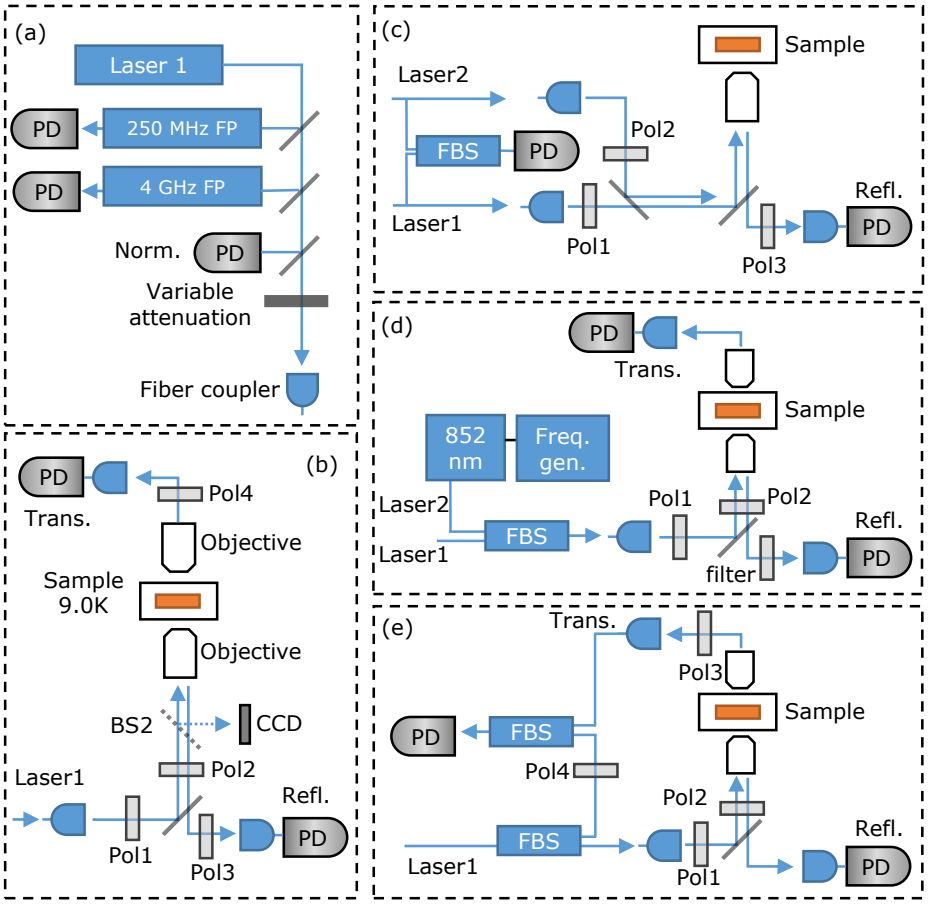

Figure 2.2: Schematic diagrams of the optical setups used throughout this thesis. (a) Setup used when scanning a single laser. PD: photodiode. FP: Fabry-Perot interferometer. Norm: normalization channel. (b) Setup when scanning a single laser and monitoring the reflection and transmission intensities. Pol.: polarizing optics. CCD: CCD-camera. (c) Setup for two lasers experiments. FBS: fiber beamsplitter. (d) Setup used for one resonant laser and one chopped off-resonant (λ =852 nm) laser experiments. Freq. gen.: frequency generator. Filter: 900 nm longpass filter. (e) Setup used for the interference measurements. See main text for more detailed descriptions.

back into a fiber such that it can be easily connected to a high power > 1 μW PD (typically Thorlabs PDA100A Si switchable gain detector), an intermediate power 0.5-8 nW photoreceiver (New Focus 2151 Femtowatt photoreceiver), or a low intensity 1 pW - 100 pW avalanche photodetector (APD). Polarizing optics is used in four places: (i) after the first output fiber coupler (POL1), to control the intensity and match one of the optical axis of the beamsplitter, (ii) in front of the objective (POL2), to set the incoming polarization, and (iii,iv) in the collection paths of the reflected (POL3) and transmitted (POL4) light. In order to image the sample surface we use a CCD camera with in front of it a lens ($f = 100$ mm), together with a beamsplitter (BS2) that can be easily removed.

For alignment purposes it is important to mode match the input and output paths independently, which is not that straight forward as the reflection path forms a confocal setup. Therefore, first the input coupling is optimized by collecting, and maximizing, the transmitted signal with a large area free-space PD. Then, the transmitted light is coupled into a fiber. Finally the reflection channel is mode matched, by exciting the sample with a 852 nm laserdiode (Thorlabs LP852-SF30) and analyzing the photoluminescence (PL) with a fiber coupled spectrometer (resolution 0.019 nm). The PL signal from the fundamental cavity mode is then optimized, and thereby the reflection channel.

For the fibers we typically use APC (angled physical contact) single mode fibers to avoid interference effects due to reflection from the fiber facets, compared to 'flat' PC (physical contact) fibers. Sometimes a multi-mode fiber can also be used in the transmission path, as this fiber is easier to align. For the fiber couplers xyz flexure stages (Elliot Scientific) are used, together with aspheric lenses (typically C240-TME-B, $f = 8.0$ mm).

2.2.2 Two resonant scanning lasers

Scans with two resonant lasers were performed in Chapter 7, where one pump laser was scanned in steps over the cavity resonance and a probe laser was scanned over the whole cavity range during each step. These measurements were crucial in unraveling the dynamical charging effects, but a similar technique could in principle also be used in the future for optical pumping, coherent population trapping, and other experiments.

The setup to perform scans with two resonant lasers is shown in Fig. 2.2 (c). A second laser is added (Toptica, DL Pro, 915-985 nm) that can also be scanned by applying an external voltage. Typically, the Toptica laser is scanned in steps and during each step the Velocity laser is scanned over the full frequency range. In order to have an indication of the relative frequency difference, light from the two lasers is combined using a fiber beamsplitter

(FBS) and the output intensity is monitored with a PD (Thorlabs, PDA-10A, 150 MHz) with a ∼1 kHz high frequency pass filter at the output. Only when the two lasers are detuned less than the PD response frequency a beating signal is produced that is slow enough to be recorded, otherwise there is a 0 V signal due to the high-pass filter. Monitoring the beating signal therefore indicates when the two lasers are resonant.

The two lasers are connected to separate fiber couplers and are superimposed using a beamsplitter, which makes it possible to control the polarization of both lasers independently. When the two lasers are polarized linear and orthogonally, a polarizer in the reflection collection path can be used to monitor only one of them. The intensity of the Toptica laser varies significantly when it is scanned over its full frequency range, and therefore additional polarizing optics is used to keep the intensity constant (not shown in figure).

2.2.3 Resonant and off-resonant chopped laser

Measurements with a resonant and an off-resonant chopped laser are displayed in Chapter 7 and were used to study the build-up and decay time dynamics of charges trapped at the oxide aperture.

In Figure 2.2 (d) we show the setup. Light from the resonant Velocity laser and the 852 nm laserdiode are combined using a FBS. The Velocity laser is first set at the cavity frequency by varying the voltage and then locked to one of the fringes of the 250 MHz FP using a PID control loop. The 852 nm light is continuously modulated by applying a square wave with a frequency generator to the 'MOD IN' input (modulation input/analog control) of the laserdiode controller. In order to record only the resonant laser in the reflection channel, a 900 nm longpass filter is used. In the transmission channel no filter is used and therefore the 852 nm laser is monitored, as typically it is operated at a much larger intensity than the Velocity. The DAQ card unfortunately has a varying time delay between the read-out of the two different APD counter channels, which makes it impossible to directly determine the relative timing of the reflection signal with respect to the 852 nm laser pulses. We solved this problem by applying a couple synchronous gating pulses to both APDs at the start of every measurement, and then determine the time delay from the recorded time traces.

2.2.4 Interference measurements

Interference measurements are the main subject in Chapter 8 and on the one hand demonstrate the coherence of scattered light by a QD as function of intensity and QD detuning, and on the other hand enable the QD induced phase shift to be extracted.

The setup to perform interference measurements is schematically sketched in Fig. 2.2 (e). The setup is identical to the one used for the one laser scans in Fig 2.2 (b), except that additionally the transmitted signal is combined with a reference signal from the scanning laser using a FBS and monitored using an APD. In order to interfere the two signals they must have the same polarization, so an additional 3-paddle polarization controller (Pol4) is used for the reference signal to the polarization to the transmission polarization (Pol3).

2.3 Sample and design

Images of the sample are shown in Fig. 2.3. Fig. 2.3 (a) shows an optical image of the sample holder, on which the sample and pieces of a chip carrier for the wire bonds have been glued. Figure 2.3 (b) displays an optical microscope image of a sample glued on a mount with a slit. The 6×7 micropillar array and voltage contacts to the p- and n-doped layers are visible. In Fig. 2.3 (c) a SEM image of the three etched trenches that define a micropillar are visible.

The oxide apertured micropillar design consists of two distributed Bragg reflectors (DBRs), a λ-thick active region containing QDs, and a $3/4\lambda$-thick aperture region. The sample structure with the refractive indices of the various layers and the simulated field intensities, as a function of the out-of-plane z-direction, are shown in Fig. 2.4 (a,b). The total sample structure with the exact layer thicknesses can be found in the Appendix.

The sample consists of many components and design considerations, of which we will give an overview: (i) First, we will discuss the DBR design considerations, and show how the mirror reflectivities, the cavity length and maximally achievable cavity Q-factor can be calculated. (ii) Next, we will consider the oxide aperture which provides the in-plane transverse mode confinement. (iii) Then, we will discuss the doped layers and show some typical IV-curves. (iv) Finally, we will discuss the QD growth, the energy level schemes, and characterization using macro- and micro-photoluminescence techniques.

2.3.1 DBR design considerations

Each DBR consists of alternating layers of GaAs and $Al_xGa_{1-x}As$ with a thickness of $(0.25 + 0.5m)\lambda$, where m is an integer, and λ is the vacuum wavelength λ_0 divided by the refractive index n. A wave travelling away from the center of the cavity where the QDs are located, will have a positive reflection amplitude $r = (n_{GaAs} - n_{Al_xGa_{1-x}As})/(n_{GaAs} + n_{Al_xGa_{1-x}As}) > 0$ at the GaAs to $Al_xGa_{1-x}As$ interface, as $n_{GaAs} > n_{Al_xGa_{1-x}As}$. This results in a field maximum at this interface and explains the intensity profile shown in Fig. 2.4 (b). The QDs must be located in a field maximum and therefore

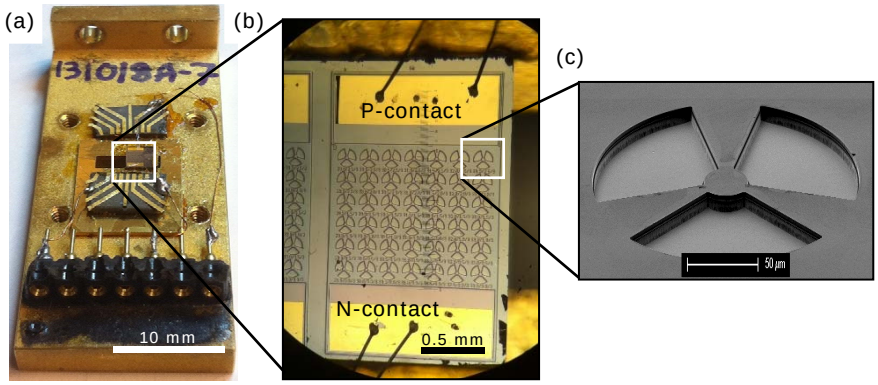

Figure 2.3: Images of a typical sample used for low temperature measurements in this thesis. (a) shows an optical microscope image of the sample on a sample holder, (b) shows the micropillar array and (c) shows a SEM image of a micropillar.

the active region requires a thickness of 1λ. The center of the oxide aperture (consisting of AlAs) is located in a field minimum to minimize light scattering on the oxide, which sets the aperture region thickness to $3/4\lambda$.

The reflectivities of the top R_{top} and bottom R_{bottom} mirrors can be calculated using [101]:

$$R_{top} = \left(\frac{(n_{GaAs})^{2k+1} - n_{vac}(n_{0.9})^{2k}}{(n_{GaAs})^{2k+1} + n_{vac}(n_{0.9})^{2k}} \right)^2$$

$$R_{bottom} = \left(\frac{(n_{GaAs})^{2k+2l+1} - n_{GaAs}(n_{0.9})^{2k}(n_{1.0})^{2l}}{(n_{GaAs})^{2k+2l+1} + n_{GaAs}(n_{0.9})^{2k}(n_{1.0})^{2l}} \right)^2 .$$

The refractive indices at 4 K are given by $n_{GaAs} = 3.478$ for GaAs, $n_{0.9} = 2.979$ for $Al_{0.90}Ga_{0.10}As$, $n_{1.0} = 2.931$ for AlAs, and $n_{vac} = 1$ for vacuum. k, l are the number of $Al_{0.90}Ga_{0.10}As$ and AlAs layers in the top and bottom mirrors. A couple layers of AlAs have been used in the bottom mirror as it gives a larger refractive index contrast and the growth is easier to control than $Al_{0.90}Ga_{0.10}As$ as it is a binary material. It oxidizes much faster than $Al_{0.90}Ga_{0.10}As$, however, and this should be prevented. The sample design that was used in Chapters 5-8 of this thesis consists of $(k = 26, l = 0)$ for the top mirror and $(k = 16, l = 13)$ for the bottom mirror. The number of GaAs layers is equal to $k + l$ for the top mirror and $k + l - 1$ for the bottom mirror, since the top mirror is in contact with vacuum, while the bottom mirror is grown on top of a GaAs substrate. The transmittivity T is simply calculated using $T = 1 - R$, and it follows that $T_{top} = 3.66 \times 10^{-4}$ and $T_{bot} = 3.29 \times 10^{-4}$.

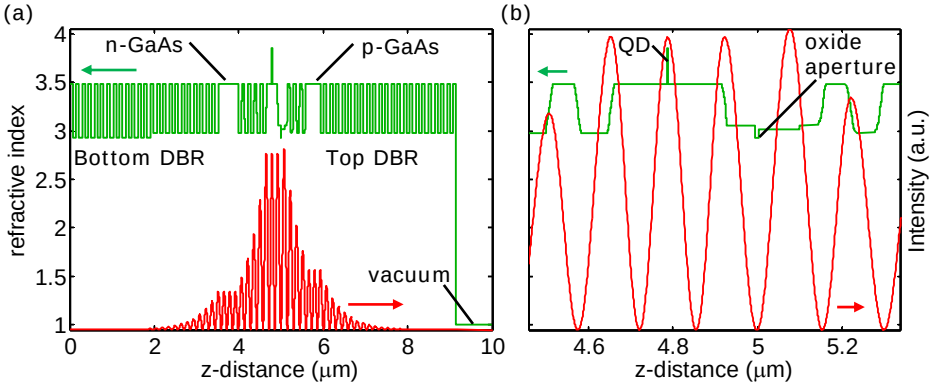

Figure 2.4: Refractive indices and simulated electric field intensities in the sample. (a) shows the total sample structure. The n-GaAs and p-GaAs contact layers are indicated. (b) shows a zoom-in of the central cavity region. Red: electric field intensity. Green: refractive index.

The cavity length is given by: $L = L_{DBR1} + L_{active} + L_{aperture} + L_{DBR2}$, where $L_{DBR1/2}$ is the penetration depth of the top/bottom DBR, L_{active} is the length of the active region and $L_{aperture}$ is the length of the aperture region. The DBR penetration depth is given by [102]: $L_{DBR} = \lambda_0/(4\Delta n)$, where $\Delta n = 0.499$ is the refractive index difference between GaAs and $Al_{0.90}Ga_{0.10}As$. It is more practical to express the cavity length in number of wavelengths $N_\lambda = L\overline{n}/\lambda_0$, where $\overline{n} \approx 3.25$ is the average refractive index. As $L_{active}\overline{n}/\lambda_0 = 1$, $L_{aperture}\overline{n}/\lambda_0 = 0.5$, and $L_{DBR}\overline{n}/\lambda_0 \approx 1.6$, the number of wavelengths is given by $N_\lambda \approx 4.75$.

The mirror loss rate κ_m is calculated using: $\kappa_m = T_{DBR}/t_{round}$, where $t_{round} = 2N_\lambda\lambda_0/c$ is the cavity round trip time. From the above-mentioned values the mirror loss rate is calculated to be $\kappa_{m1} = 12.3$ ns^{-1} for the top mirror and $\kappa_{m2} = 11.1$ ns^{-1} for the bottom mirror. If the cavity Q-factor would only depend on the mirror loss rate, it would be given by $Q = \omega/(\kappa_{m1} + \kappa_{m2}) = 8.6 \times 10^4$.

2.3.2 Oxide aperture

The role of the oxide aperture is schematically depicted in Fig. 2.5 (a). On the one hand it provides in-plane light confinement which, together with the out-of-plane confinement provided by the DBRs (as seen in Fig. 2.4), enables small cavity mode volumes. The confinement potential, which is approximately parabolic, gives rise to Hermite-Gaussian optical modes [103]. These modes can be studied through photoluminescence or reflectivity measurements, both at cryogenic and at room temperatures, as is displayed in

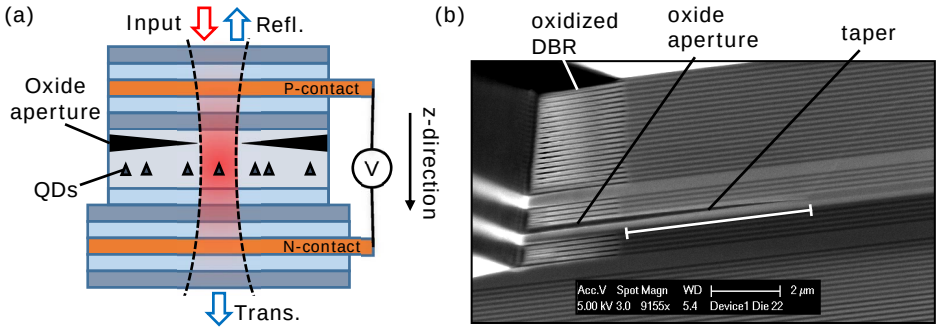

Figure 2.5: Oxide aperture. (a) Schematic drawing of a oxide apertured MP and the Hermite-Gaussian optical mode (number of Bragg pairs and layer thicknesses not to scale). (b) shows a SEM image of the cross-section of an oxidized sample, the tapered oxide aperture and the oxidized $Al_{0.90}Ga_{0.10}As$ in the DBR are indicated.

Chapters 3-5. Additionally, as is displayed in Fig. 2.3 (c), they make it possible to have three 'bridges' that connect the MP to the bulk material in order to enable global voltage contacts.

An oxide aperture is fabricated through the conversion of $Al_xGa_{1-x}As$ to AlO_x during a wet oxidation process. For this, the sample is placed in an oxidation furnace at a temperature of 420 °C and water vapor, carried by N_2 gas, flows around the sample. The wet oxidation is either performed in the home-built oxidation furnace equipped with a viewing port in order to monitor the oxide formation, as is done in Ch. (4,5), or it is performed using the conventional Lindberg furnace in the UCSB cleanroom, as is the case for the samples used in the other chapters. During the conventional UCSB procedure the oxide formation is not monitored, and the exact timing is critical in order to obtain the desired oxide aperture penetration depth. This process is made more accurate by first oxidizing several calibration samples, consisting of etched ridges. The oxidation rate (μm s^{-1}) can then be determined from the SEM image of a cross-section of the sample and is used to determine the oxidation time for the real samples. An example of an image of such a cross-section is presented in Fig. 2.5 (b). As the 10 nm AlAs layer at the center of the aperture region oxidizes faster than the surrounding 66 nm $Al_{0.75}Ga_{0.25}As$ and 95 nm $Al_{0.83}Ga_{0.17}As$ layers, a tapered oxide-aperture is formed, as can be seen in the figure. This taper provides a more gentle confining potential of the transverse optical field compared to a non-tapered aperture, and thereby provides less scattering losses.

2.3.3 Doped layers and voltage contacts

The QDs are embedded inside a PIN diode structure in order to enable deterministic charge control and energy control through the DC Stark shift. The QDs are separated by a 20 nm tunnel barrier from n-doped GaAs and by 110 nm GaAs from p-doped GaAs. For the n-doping Silicon is used and for the p-doping Carbon. Varying doping densities were used as can be seen in the sample structure included in the Appendix.

Countersink etches to the doped GaAs contact layers are made and metal contacts are then applied. The etching occurs through 'Reactive ion etching' during which the reflectivity of a HeNe laser is monitored in order to control the etch depth. To allow some variations in the etch depth, the GaAs contact layers to which the countersink etch is made are thicker, namely $5/4\lambda$ for the p-doped top contact layer and $7/4\lambda$ for the n-doped bottom contact layer. The contact layers are located 3-4 DBR pairs outside of the central cavity region, and therefore both GaAs and $Al_xGa_{1-x}As$ in the DBR are doped. The interface between GaAs and the larger bandgap $Al_{0.90}Ga_{0.10}As$ imposes risk to give rise to a Schottky barrier, which is undesired as it gives an electric field drop that modifies the electric field across the PIN diode as function of the applied bias voltage, and it can act as a charge trap. In order to prevent this the interfaces are graded, meaning that the Al content is linearly or parabolically varied in small steps over ~ 20 nm, and additionally a larger dopant concentration is used at the interfaces.

The metal contact for the p-doped layer consists of Ti-Pt-Au (from bottom to top), and Ni-AuGe-Ni-Au for the n-doped layer. Rapid thermal annealing is used to ensure Ohmic contacts. Figure 2.6 (a,b) shows IV-curves (current measured as function of voltage) of a sample with good contacts made from the 'G130422A' wafer and gives similar results as the 'G131018A' wafer. IV-curves without (blue line) and with (green line) the presence of an additional pump laser are recorded. The pump laser excites charges in the intrinsic region which, in the case of proper Ohmic contacts, are collected and give rise to a more-or-less constant negative current offset. For the blue lines typical diode characteristics are clearly visible. Based on the energy bandgap of GaAs, a turn-on voltage of 1.42 V at room temperature and 1.52 V at 9.0 K is expected. As can be seen in the figure, the obtained values of 0.5 V and 1.0 V are lower, indicating that charges are leaking through the intrinsic region.

The positive voltage bias range, in which QDs are typically optically active, is indicated with the grey shaded area. For smaller voltages, the electric field across the QDs makes optically excited charges tunnel out of the QD before they can optically recombine. For larger voltages, the QD lines appear broader

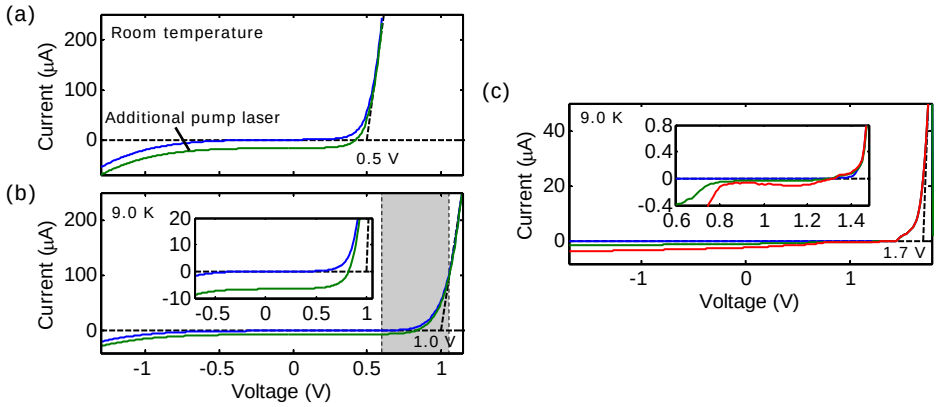

Figure 2.6: IV-characteristics. (a) shows the room temperature IV–curves of a sample from the 'G130422A' wafer without (blue line) and with (green line) the presence of an additional HeNe pump laser. (b) shows the IV–curves of the same sample but cooled down to 9.0 K and using a 780 nm laserdiode pump laser. The grey shaded area indicates the forward bias voltage range where QDs are optically active. (c) demonstrates IV-curves from a sample from the '110207C' wafer without (blue line) and with a 1.2 mW (green line) and 2.3 mW (red line) 852 nm pump laser. The non-uniform current offset that the pump laser induces indicates improper (non-Ohmic) contacts.

and difficult to distinguish from a broadband background photoluminescence, possibly due to the forward bias current.

An example of IV-curves of a sample with improper contacts are shown in Fig. 2.6 (c), which was made from older material ('110207C' wafer). When the sample is not excited (blue line) the IV-curve looks quite typical, albeit with a higher than expected turn-on voltage of 1.7 V. However, the presence of additional pump lasers with increasing intensities (green and red line) give rise to a non-uniform current offset that is strikingly different from what is displayed in Fig. 2.6 (a,b). QDs were still visible in this sample in the voltage range 0.5-1.5 V, but no good charge and energy control was possible. Recording IV-curves without and with the presence of a pump laser therefore serve as a first test on the quality of the contacts, which can be performed before characterizing QD charge and energy tuning.

2.4 Quantum dots

Quantum dots are small semiconductor nanocrystals that confine positive and negative charges in all three dimensions. Charges and excitons therefore exhibit quantum mechanical properties and the allowed energy states are quantized, which leads to discrete optical transitions and QDs are therefore

also called 'artificial atoms'. In the following we will describe their growth, the energy level structure and characterization.

2.4.1 QD growth

Quantum dots are grown by molecular beam epitaxy of In and As on top of a GaAs substrate through a process called Stranski-Krastanov growth, also known as 'layer-plus-island' growth [104]. When less than 1.5 monolayers of InAs are deposited on a GaAs substrate, first a wetting layer is formed. When a thicker layer is deposited, InAs islands are formed to release strain coming from the lattice mismatch between InAs and GaAs. Since we require reasonably high QD densities of $\sim$ 100 μm^{-2}, 1.85 monolayers of InAs are deposited. The growth occurs at a temperature of 500 °C and is accurately monitored using RHEED (Reflection high-energy electron diffraction). Additionally, the partial capping technique is applied, which implies that after the QD growth a $\sim$1 nm GaAs layer is deposited and an annealing step is applied [105]. This ensures a homogeneous $\sim$1 nm QD height and spectral distribution. A STM (scanning tunneling microscopy) image of the cross-section of a QD is shown in Fig. 2.7 (a) and shows how the QD can be seen as a $\sim$ 50 nm diameter lens-shaped InAs droplet inside a GaAs matrix.

In order to determine the QD density and spectral distribution, a calibration sample is grown that contains one layer of encapsulated QDs and on top one layer of uncapped QDs. Figure 2.7 (b) shows an AFM image of the encapsulated QDs on top of a GaAs substrate. From this the QD density is determined to be $\sim$ 110 μm^{-2}. Figure 2.7 (c) shows photoluminescence collected over a large area from the encapsulated QDs. This macro-PL spectrum shows several peaks, of which the largest two are centered at $\lambda = 927$ nm and $\lambda = 950$ nm. These peaks arise most likely from monolayer height fluctuations of the QDs. AFM and macro-PL characterization provides critical information on the spatial and spectral density of the QDs at the cavity mode wavelength, and helps to estimate the chance whether a QD can be found that couples spatially and spectrally with a cavity resonance.

2.4.2 QD level scheme

A QD forms a zero dimensional structure where the energy levels of valence and conduction band electrons are quantized, as InAs has a smaller energy band gap (0.43 eV for bulk InAs at 0 K) compared to the surrounding GaAs matrix (1.52 eV) and because of its small $\sim$nm dimensions. QDs are therefore called 'artificial atoms', as the excitation and recombination of an electron-hole pair, called an exciton, occurs at well-defined energies, while for higher dimensional structures a continuum of energy levels is present. Due to the

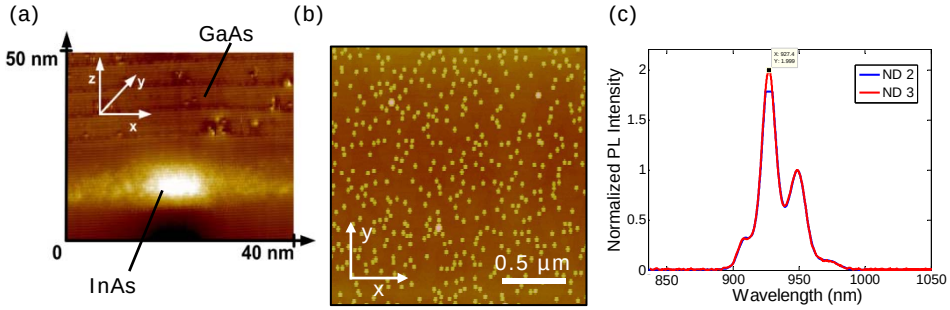

Figure 2.7: Quantum dot characteristics. (a) shows a scanneling tunneling image of the cross-section of a QD [106]. (b) shows an AFM scan of uncapped QDs. (c) shows QD macro-PL. [(b,c) Courtesy of Ajit Barve].

small out-of-plane dimension of the QDs the heavy-hole and light-hole bands are split in energy and the excitation of a heavy-hole spin, which carries spin $S_z = \pm 3/2$, is lowest in energy. By embedding the QDs in a PIN-diode structure, the Fermi energy level E_F, the energy up to which all allowed energy levels are occupied, can be tuned by applying a bias voltage and controls the QD charge occupation.

Figure 2.8 (a) shows the case where the Fermi level is tuned just below the lowest conduction band energy level and the QD is charge neutral. The QD 'empty' ground state $|0\rangle$ can be excited to the $|X^0\rangle$ exciton state. In Fig. 2.8 (b) it is displayed that the exciton has two fine split excited states which can be excited with linearly polarized light (along the xy-direction) of orthogonal polarizations. The fine splitting arises from QD anisotropy in the QD shape, composition, and strain, which leads to electron-hole exchange interaction, and causes the exciton orientation to not be in the out-of-plane direction ($|\uparrow\Downarrow\rangle$ and $|\downarrow\Uparrow\rangle$), but in the in-plane direction.

Figure 2.8 (c) shows the case where the Fermi level is tuned just above the first conduction band level and the QD ground state $|e\rangle$ and excited state $|X^{1-}\rangle$ are singly-charged. Coulomb repulsion energy ensures that the QD is not doubly-charged. In Fig. 2.8 (d) the energy level scheme is displayed in the absence of an external magnetic field. The ground state spin up $|\uparrow\rangle$ and spin down $|\downarrow\rangle$ states, carrying spin $S_z = \pm 1/2$, can be excited with circularly polarized transitions to the corresponding excited states carrying spin $S_z = \pm 3/2$. The relevant energy levels for the case where an in-plane magnetic field B_x is applied is shown in Fig. 2.8 (e), where the spin states are now oriented in the same in-plane x-direction. Even though this configuration was not investigated thoroughly during the time of this thesis, it is important for quantum information applications, as it enables among others high-fidelity

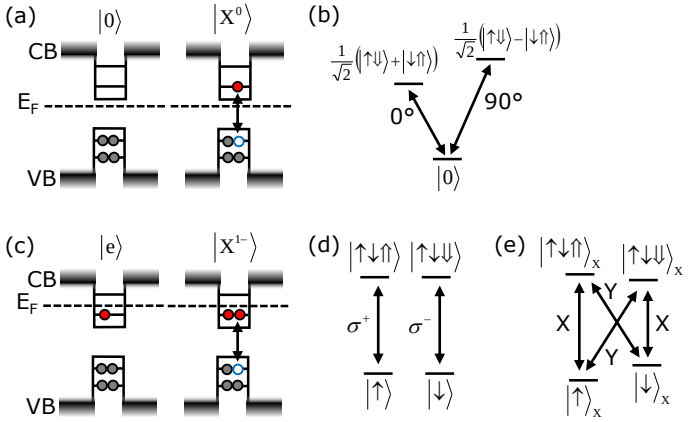

Figure 2.8: Schematics of quantum dot energy levels. (a) shows schematically the ground state $|0\rangle$ and excited state $|X^0\rangle$ of a charge neutral QD. E_F: Fermi level, CB: conduction band, VB: valence band. (b) shows the relevant energy level scheme, where the fine split excited states can be excited with orthogonally linearly polarized transitions. (c) displays schematically the ground state $|e\rangle$ and excited state $|X^{1-}\rangle$ of a singly-charged QD. (d) displays the energy levels without an external magnetic field and (e) shows the case where an in-plane magnetic field B_x along the x-direction is applied. The ground and excited states are coupled by circularly polarized transitions (σ^+, σ^-) or linearly polarized transitions in the x- or y-direction (X,Y).

spin state preparation [107, 108], coherent population trapping [106, 109], and optical manipulation [72–74].

2.4.3 QD characterization

In order to characterize the charge and DC Stark shift tuning of individual QDs, the sample is excited non-resonantly with a $\lambda = 852$ nm laser and photoluminescence is collected as function of wavelength from a small spot size (micro-PL) on a contacted sample. An excellent area to probe micro-PL in a micropillar sample is the region around the top metal contact, as here the top mirror is almost completely etched away and a low Q cavity provides a wide spectral window to view individual QDs. Spatial scans of micro-PL collected at different wavelengths is shown in Fig. 2.9 (a,b), where single QDs are clearly visible as point-like emitters. Figure 2.9 (c) shows micro-PL recorded as function of voltage. Individual QD lines are visible that show a DC Stark shift and charge tuning. In the voltage range 0.65-0.85 V the QDs are neutral, while above 0.85 V the QDs are singly negatively charged. The charged state of the QDs can be determined by analyzing the PL as function of the collected polarization. As is shown in Fig. 2.9 (d) for a charge neutral

QD, two fine-split transitions with linear orthogonal polarizations are visible. PL from a singly charged QD, presented in Fig. 2.9 (e), does not display this fine-splitting.

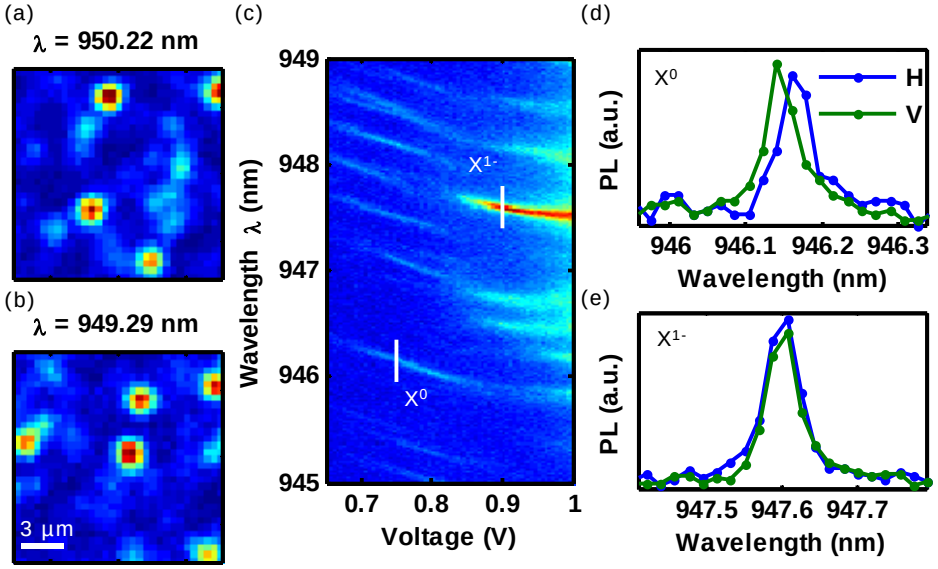

Figure 2.9: Micro-photoluminescence using off-resonant excitation (λ = 852 nm) on individual quantum dots. (a, b) show spatial scans at collection wavelengths labelled in the title. (c) shows the PL intensity as function of the applied bias voltage and the spectrometer wavelength. (d) shows PL at a fixed voltage as function of two linear orthogonal polarizations, showing the fine structure splitting of a neutral QD (X^0). (e) shows the PL for the same two polarizations for a singly-charged QD. White lines in (c) indicate the voltage and wavelength range that (d,e) are recorded.

Chapter 3

Monitoring the formation of oxide apertures in micropillar cavities

An imaging technique is presented that enables monitoring of the wet thermal oxidation of a thin AlAs layer embedded between two distributed Bragg reflector mirrors in a micropillar. After oxidation we confirm by white light reflection spectroscopy that high quality optical modes confined to a small volume have been formed. The combination of these two optical techniques provides a reliable and efficient way of producing oxide apertured micropillar cavities for which the wet thermal oxidation is a critical fabrication step.

M. P. Bakker, D. J. Suntrup III, H. Snijders, T.-A. Truong, P. Petroff, M. P. van Exter, and D. Bouwmeester, Applied Physics Letters **102**, 101109 (2013).

3.1 Introduction

Wet thermal oxidation is a widely used technique that allows for optical (electrical) confinement by making use of the large difference in effective refractive index (resistivity) between oxidized and unoxidized regions[110]. It is an important fabrication step in the production of vertical cavity surface emitting lasers (VCSELs) [111] and of certain optical microcavities [98]. Embedding self-assembled quantum dots (QDs) in such microcavities enabled the study of cavity quantum electrodynamics in solid state systems [100]. Such devices are of interest for single-photon sources [99] and for hybrid quantum-information devices [112].

A real challenge, however, is to obtain a high fabrication reliability in the wet oxidation process, since the oxidation rate depends strongly on parameters which are difficult to reproduce, such as the roughness of the etched sidewalls or the Al composition to within an $\sim 1\%$ accuracy. As repetitive calibrations can be costly, techniques to monitor the oxide formation in situ are important. All three techniques reported so far make use of the change in the reflectivity spectrum as one or more Al containing layers are being oxidized. The average change in reflectivity of a large patterned area can be monitored [113]. The reflectivity contrast between a fully oxidized distributed Bragg reflector (DBR) mirror and unoxidized areas can be directly viewed through a charge coupled device (CCD) camera using broadband light [114]. Finally a buried,

thin oxide aperture layer can be imaged [115], but this technique is delicate as the applied wavelength interval has to be tuned carefully such that the reflectivity contrast allows for sufficient spatial resolution.

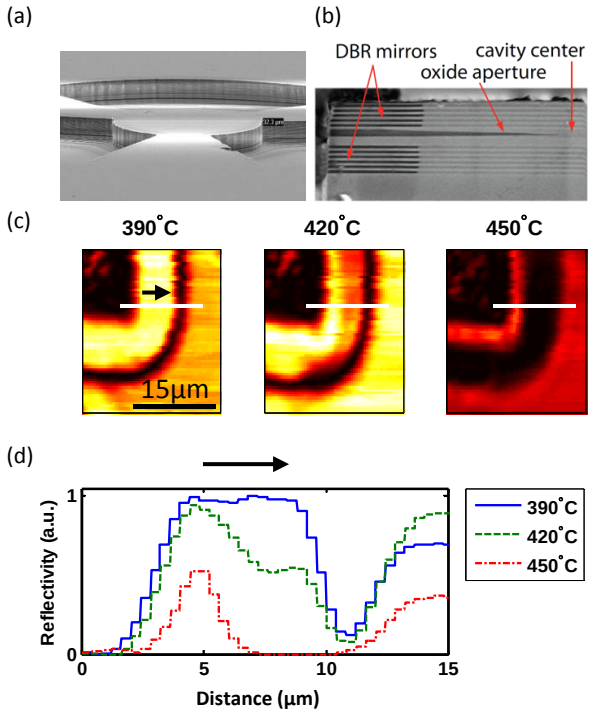

Figure 3.1: (a) SEM image of the three etched trenches that form a micropillar mesa connected to the bulk material. (b) SEM cross-sectional image of the center of a micropillar. Al_xO_y is darker than the $Al_xGa_{1-x}As$ layers. (c) Reflection scans (light: high reflectivity) taken with a 1064 nm laser for different temperatures at the corner of an etched trench (white box in Fig. 3.3 shows this corner for a different micropillar). (d) Reflectivity as a function of the distance along the white lines in (c).

In this Chapter, we present a new imaging technique based on measuring the reflectivity, while scanning with a monochromatic beam over an etched micropillar structure. We use a wavelength on the red side of the photonic stopband, such that absorption in the semiconductor material is low for temperatures up to 450°C. For an oxidized sample we are able to clearly identify three regions: unoxidized regions, regions where only a thin aperture layer has been oxidized and regions where both the aperture region and the DBR mirror are oxidized. We then monitor a sample while it is being oxidized and stop the oxidation when only a small unoxidized area is left at the center of a micropillar structure. After oxidation, we perform an in situ characterization at room temperature of the optical modes defined by the optically

confining oxide aperture.

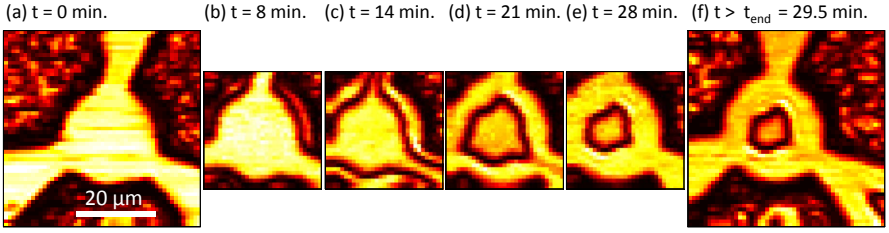

Figure 3.2: (a) Reflectivity scan (light: high reflectivity) of a 1064 nm laser on an etched micropillar before the oxidation was started. (b-e) Reflectivity scans for different times after the oxidation was started. Every scan takes about 1.5 minutes. (f) Reflectivity scan taken after the oxidation was stopped after 29.5 minutes.

The sample is grown by molecular beam epitaxy on a GaAs [100] substrate and is constructed as follows: two DBR mirrors, comprising alternating $\lambda/4$-thick layers of GaAs and $Al_{0.9}Ga_{0.1}As$, embed an aperture layer, consisting of a thin 10 nm AlAs layer in between $Al_{0.75}Ga_{0.25}As$ and $Al_{0.83}Ga_{0.17}As$, and an active layer containing InGaAs/GaAs self-assembled quantum dots inside a PIN diode structure. Trenches are etched down to the bottom DBR using reactive ion etching, leaving a 30 μm circular micropillar connected by three narrow unetched channels to the bulk material (see Fig. 3.1a). Global electrical contacts to the doped layers allow for control of the electrical field inside every micropillar in an array of 42 micropillars.

3.2 Monitoring the oxide formation

The conversion of $Al_xGa_{1-x}As$ into Al_xO_y takes place by applying H_2O vapor to the sample at a typical process temperature of 400-450°C. Special care is taken to prevent dry oxidation with oxygen, as it has been reported that this can prevent further wet oxidation [110]. First native oxide is removed from the $Al_xGa_{1-x}As$ by dipping the sample for 20s in NH_4OH, then it is rinsed with demineralized water and placed in isopropanol. The sample is finally clamped to a holder, equipped with a heater and a thermocouple, inside an oxidation chamber fitted with a viewport. Isopropanol is maintained on the sample surface until the chamber has been filled with nitrogen gas, in order to prevent exposure to oxygen. Steam is applied by flowing nitrogen carrier gas through a water-filled bubbler heated to 95°C.

In Fig 3.1(b) a SEM cross sectional image shows that the oxide penetration depth varies for different layers. Our goal is to view and monitor the growth of the oxidized layers in situ with a non-invasive optical technique.

A NA=0.40 and 20 mm working distance objective is used to image the sample surface on a CCD camera and to focus incident light to a diffraction limited spot size. In order to differentiate between regions with a different extent of oxidation, we monitor the reflectivity of a focused Nd:YAG 1064 nm laser beam that we scan across the sample. In order to find the operating temperature that yields the best reflectivity

contrast, we take spatial reflectivity scans of an already oxidized sample at the edge of an etched trench (see Fig 3.1(c)). The reflectivity change with refractive index is temperature dependent. In Fig. 3.1(d) the reflection intensities along the white lines in Fig 3.1(c) are presented. Starting from the left side of the graph where the etched trench is, the reflectivity rapidly changes from low to high when the oxidized DBR is reached. In the middle a constant reflectivity is visible, corresponding to an oxide layer with a constant thickness. On the right side the gradient in the oxide layer, at the end of the oxide aperture, causes a varying reflectivity after which the reflectivity of the unoxidized region is more or less constant.

When performing a monitored oxidation with this specific wafer material, a temperature of 420°C is chosen. At this temperature the contrast between the oxide aperture and the unoxidized regions is larger than at higher temperature, and the oxidation rate is fast enough to complete the oxidation in about 30 minutes. In order to monitor the oxidation at a different temperature with similar contrast, a light source with a different wavelength could be used.

First we take an unoxidized sample and perform a spatial reflectivity scan of the micropillar center. Fig. 3.2 (a) shows a homogeneous reflectivity for the unetched regions and a lower reflectivity for the etched parts. Once the oxidation process is started, continuously scans are recorded, which take about 1.5 minutes each. Several of these scans are shown in Fig 3.2 (b-e).

The front of the oxide aperture, in this case characterized by a lower reflectance, starts to penetrate towards the micropillar center. After 29.5 minutes the oxide taper has advanced to within 3 μm of the pillar center and we stop the oxidation by shutting off the water vapor flow and purging the oxidation chamber with nitrogen. Several minutes after the oxidation was stopped a final scan is taken (Fig. 3.2 (f)).

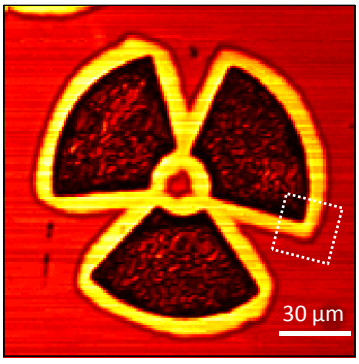

Figure 3.3: Reflectivity scan (light: high reflectivity) of the same micropillar as in Fig. 3.2, taken over a larger region at room temperature.

Once the sample has cooled down to room temperature, a large spatial reflectivity scan is taken, see Fig. 3.3. The unoxidized center, having the same reflectivity as regions far away from the etched trenches, is seen to have the same size and shape as

the center of the scan in Fig. 3.2(f), which was recorded at 420°C.

3.3 Room-temperature characterization

In order to characterize the confined optical modes of the device, the center of the micropillar is illuminated using a superluminescence diode (Superlum, 920-980nm), with a wavelength range covering the optical modes, and the reflection spectra are recorded with a spectrometer as a function of position [116]. Fig. 3.4(a) shows spatial scans of the reflected intensity at the resonance wavelengths of the first six Hermite-Gaussian modes. Fig. 3.4(b) shows the reflection spectra at six positions, marked in Fig. 3.4(a) with black dots and numbers. These positions correspond to the minima in the reflection spectra and demonstrate a clear spatial separation of the different modes. In order to determine the Q-factor, we fit a Lorentzian reflection dip to the Ψ_{00} mode and find a Q-factor 10,000-12,000. For the average wavelength splitting $\Delta\lambda$, between the fundamental Ψ_{00} and first order Ψ_{10} and Ψ_{01} modes, we find $\Delta\lambda \approx 0.62$ nm.

An important figure of merit of microcavities is the Purcell factor $P = \frac{3}{4\pi^2}(\frac{\lambda_0}{n})^3 \frac{Q}{V}$, where λ_0 is the cavity wavelength, n is the refractive index, Q is the quality factor and V is the mode volume. Assuming there is a quadratic confining potential present, giving rise to Hermite-Gaussian optical modes, this can be rewritten as: $P = \frac{12}{\pi} F(\frac{\Delta\lambda}{\lambda_0})$ [103]. Here $F = \frac{\lambda_0 Q}{2nL_{eff}}$ is the cavity finesse and L_{eff} is the effective cavity length. By combining the measured Q-factor 10,000-12,000, $\Delta\lambda \approx 0.62$ nm with $n \approx 3$ and $L_{eff} \approx 1.4$ μm estimated from the device structure, we find an estimated Purcell factor $P = 2.8 - 3.4$.

Higher Purcell factors can be obtained by performing the oxidation longer and thereby reducing the cavity volume. Also the $Q-$factor, limited by absorption in the doped layers, can be further increased by cooling the device to a temperature of 4K, where such micropillars containing quantum dots are typically operated. The difference in the wavelength splitting, between the fundamental Ψ_{00} and either one of the first order Ψ_{10} and Ψ_{01} modes, is a result of elipticity arising from preferential oxide formation rates and can be compensated for by etching elliptical micropillars. Finally we would like to note that the fundamental cavity mode in micropillars is typically polarization non-degenerate due to birefringence, although we were limited by the resolution of the spectrometer of 0.019 nm and could not characterize this. Permanent tuning to compensate for this birefringence has been demonstrated [94] and could be used as a final step in the fabrication process.

3.4 Conclusion

In conclusion, we have developed a procedure that allows for the fabrication and characterization with high accuracy of high quality micropillar cavities that, operating at cryogenic temperatures, are of interest for quantum information applications.

This work was supported by NSF under Grant No. 0901886, the Marie-Curie Award No. EXT-CT-2006-042580 and FOM-NWO Grant No. 08QIP6-2. We thank Cristian Bonato for useful discussions.

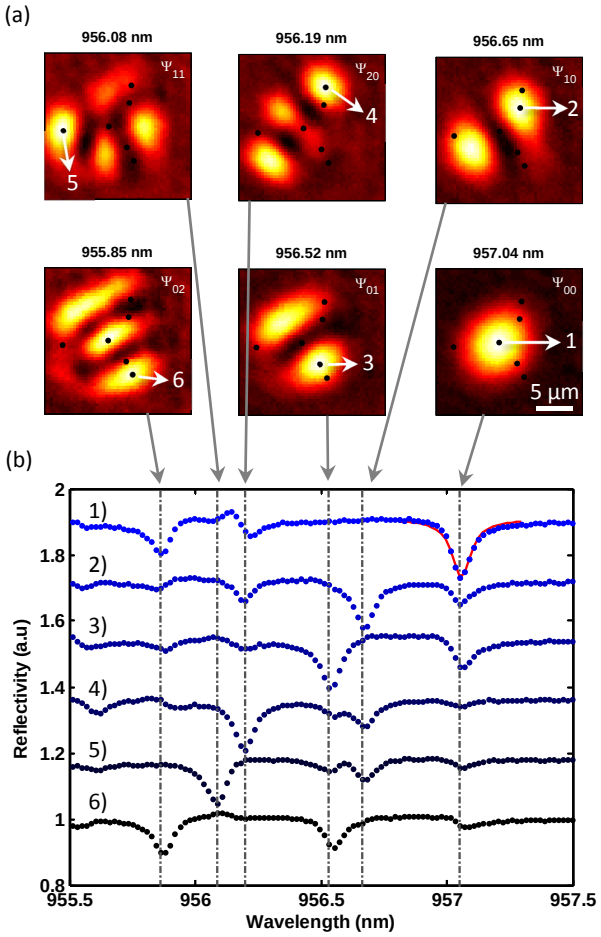

Figure 3.4: (a) Reflectivity scans (light: lower reflectivity) for the indicated wavelengths, between 955.5-957.5 nm, as a function of position in the center of a micropillar. (b) Reflection spectra at the six positions that are marked with a black dot and labelled with numbers 1-6. An offset is added between each trace. The red line in curve 1 is a fit to determine the Q-factor of the Ψ_{00} mode.

Chapter 4

Fine tuning of micropillar cavity modes through repetitive oxidations

Repetitive wet thermal oxidations of a tapered oxide aperture in a micropillar structure are demonstrated. After each oxidation step the confined optical modes are analyzed at room temperature. Three regimes are identified. First, the optical confinement increases when the aperture oxidizes towards the center. Then, the cavity modes shift by more than 30 nm, when the taper starts to oxidize through the center, leading to a decrease in the optical path length. Finally, the resonance frequency levels off, when the aperture is oxidized all the way through the micropillar, but confined optical modes with a high quality factor remain. This repetitive oxidation technique therefore enables precise control of the optical cavity volume or wavelength.

M. P. Bakker, D. J. Suntrup III, H. Snijders, T.-A. Truong, P. Petroff, D. Bouwmeester, and M. P. van Exter, Optics Letters **38**, 3308 (2013).

4.1 Introduction

Semiconductor optical microcavities have found many applications [117]. To obtain optical confinement one commonly used technique is wet thermal oxidation, which makes use of the large difference in effective refractive index between oxidized and unoxidized regions [98, 110]. By embedding self-assembled quantum dots (QDs) in etched micropillar cavities combined with an oxide aperture, high-frequency single-photon sources have been realized [99]. Moreover, by combining a large Purcell factor with a high mode-matching efficiency to external fields, such microcavities enabled the study of cavity quantum electrodynamics in solid state systems [100], which can lead to hybrid quantum information devices [112].

It is a challenge however to obtain reproducible oxidation results, since the wet thermal oxidation process depends strongly on difficult-to-reproduce parameters, such as the roughness of etched sidewalls or the Al composition to within $\sim 1\%$ accuracy. One approach is to monitor the formation of oxide layer(s) in real time. This has been demonstrated using several techniques [113–115, 118]. However controlling the size of the oxide aperture, and thereby the exact optical confinement with submicrometer precision, can be challenging by imaging the aperture alone. An alternative method would then be, once the desired amount of confinement has nearly been reached,

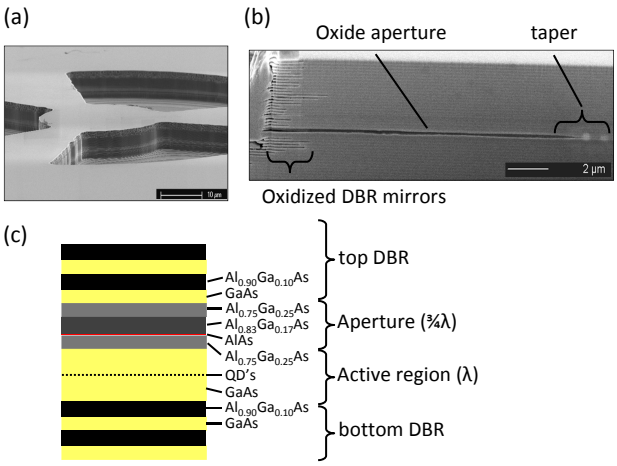

Figure 4.1: (a) SEM image of the three etched trenches that form a micropillar mesa connected to the bulk material. (b) SEM image of the FIB cross section of the sidewall of an etched trench. Al_xO_y is darker than the $Al_xGa_{1-x}As$ layers. [Courtesy to Hozanna Miro (Kavli NanoLab Delft)] (c) The different $Al_xGa_{1-x}As$ layers that make up the aperture and the active region in the center of the micropillar structure. Of the top and bottom DBR mirrors, typically consisting of 30 layer pairs, only a couple $\lambda/4$ layers are shown. InAs self-assembled quantum dots are located in the center of the GaAs active region in an anti-node of the intracavity intensity, while the AlAs layer in the aperture is located at a node .

to repeat the oxidation in small steps and characterize the device in between until desired optical properties have been achieved.

In this Chapter we report such a repetitive oxidation technique. We perform in total 56 oxidation steps of varying duration on the same micropillar and characterize the device after each step at room temperature. We analyze the optical modes with a resonant reflectance technique to determine the wavelengths of the modes and the modesplitting between fundamental and first-order modes. Also by scanning a focused 1064 nm laser and monitoring the reflectance across the sample, we obtain an indication of the advancement of the oxide front inside the micropillar. We demonstrate that the exact optical confinement can be accurately controlled. Also, by oxidizing the aperture throughout the micropillar, we find that the overall wavelengths of the modes can be tuned by up to 30 nm.

4.2 Sample

The micropillars are constructed as follows [99]: first through molecular beam epitaxy on a GaAs [100] substrate two DBR mirrors are grown, comprising alternating $\lambda/4$-thick layers of GaAs and $Al_{0.9}Ga_{0.1}As$. In between the mirrors are a $3/4\lambda$-thick aperture layer, consisting of a thin 10 nm AlAs layer in between $Al_{0.75}Ga_{0.25}As$ and $Al_{0.83}Ga_{0.17}As$, and a λ-thick active layer containing InGaAs/GaAs self-assembled quantum dots inside a GaAs PIN diode structure. Then, using reactive ion etching,

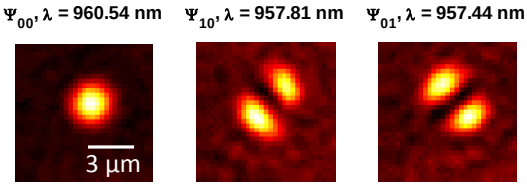

Figure 4.2: Example of position dependent reflectance measurements, obtained after the 18^{th} oxidation and a total oxidation time of 187 minutes. When a cavity resonance is hit the reflectance decreases (light color). The shape of the modes indicate clearly Hermite-Gaussian modes. The titles denote the labels of the modes and the wavelengths selected from the reflectance spectrometer spectra.

trenches are etched down to the bottom DBR leaving a 30 μm circular micropillar connected by three narrow unetched 'spokes' to the bulk material (see Fig. 4.1). Global electrical contacts to the doped layers enable control of the electrical field inside every micropillar in an array of 42 micropillars.

4.3 Repetitive oxidations and room-temperature characterization

The conversion of $Al_xGa_{1-x}As$ to Al_xO_y takes place by applying water vapor to the sample heated to 400°C. First we clamp the sample to a holder equipped with a heater, and place it inside a small oxidation furnace equipped with a viewport. Water vapor is applied by flowing nitrogen through a water-filled bubbler. While heating up or cooling down the sample in between the oxidations, we purge the furnace with nitrogen in order to prevent dry oxidation through exposure to oxygen. We speculate that, by preventing exposure to oxygen while the sample is heated, sealing is prevented and repetitive oxidations are thereby made possible.

At room temperature we characterize the optical modes by scanning a focused superluminescence diode (Superlum, 920-980 nm) over the micropillar center and record the reflectance spectra with a spectrometer [116]. An example of the spatial reflectance at the different wavelengths corresponding to the fundamental Ψ_{00} and first order Ψ_{10}/Ψ_{01} Hermite Gaussian modes is shown in Fig. 4.2.

In Fig. 4.3 we present the wavelengths of the three modes as a function of the total time that oxidation has taken place. A polarization splitting is visible for the different modes due to birefringence.

From the data we calculate the average mode splittings in Fig. 4.4. A difference in the mode splittings $\Delta\lambda_{10}$ and $\Delta\lambda_{01}$ indicates that the center of the oxide front is elliptically shaped. In both figures we can clearly distinguish three regimes (I, II, III) which will be discussed later.

We also scan over the micropillar and monitor the reflectance using a 1064 nm Nd:YAG laser. We use such a wavelength at the red side of the photonic stopband, since here the reflectance spectrum is sensitive to interference of the reflections from the top and bottom DBR mirrors. As a consequence, changes in the optical length of the spacing layer due to the decrease of the effective refractive index during the oxidation change the reflectance. This technique therefore allows to probe which

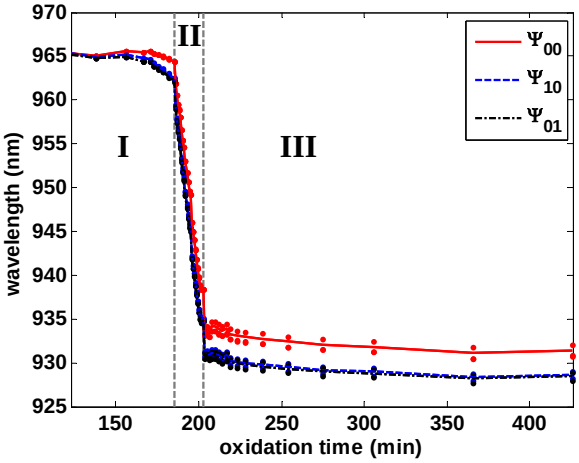

Figure 4.3: The wavelength of the three lowest order Hermite Gaussian modes, determined at room temperature in between every oxidation step, as function of the total preceding oxidation time. The wavelengths for different polarizations are shown by dots, the average is indicated with a line.

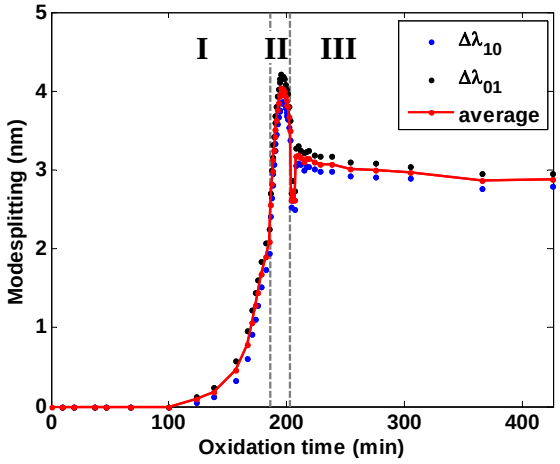

Figure 4.4: The wavelength splitting between the fundamental and first order Hermite Gaussian modes.

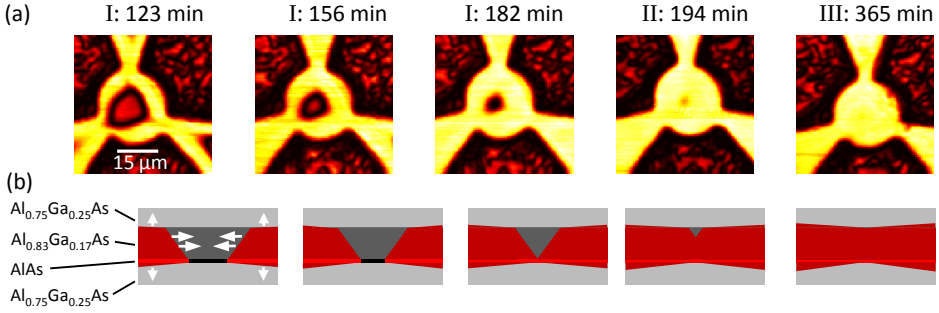

Figure 4.5: (a) Reflection measurements taken at the red side of the DBR stop band using a focused 1064 nm laser that was scanned across the micropillar center. Light (dark) corresponds to a high (low) reflectance. Regions with a similar reflectance have the same amount of oxide in the aperture region. The title of every scan is the regime number and the total time of all the preceding repetitive oxidations (see main text). (b) Schematic of the aperture region with the oxide shown in red. We deduce the oxide extent in the different layers from the reflection measurements in (a) and by analyzing the optical modes. The white arrows indicate that the oxidation proceeds much faster horizontally than vertically.

regions have a similar oxide thickness and can also be used to monitor in real time the oxide penetration towards the micropillar center [118].

Fig. 4.5 shows several reflectance images taken after different oxidation steps and a schematic of the oxide extent. The unoxidized parts have a medium reflectance and it can be seen how the front of the oxide aperture, having a lower reflectance, penetrates towards the micropillar center. Further away from the oxide front the aperture has a high reflectance of constant amplitude, indicating a constant oxide thickness. When the DBR layers are oxidized this typically results in a high reflectance and are therefore more difficult to distinguish.

To confirm these observations we took a SEM image of the FIB cross section of one of the outward sidewalls of the etched trenches as presented in Fig. 4.1 b). An oxide aperture with a more or less constant thickness and a ~ 3 μm taper are visible, in agreement with the reflectance images. Also it is seen that the DBR layers are oxidized less than 2 μm inwards for this samples and the used oxidation conditions. In contrast to previous work [119] the oxidation of these layers provide no additional optical confinement.

4.4 Interpretation of the findings

Through the characterization of the buried oxide layer and the optical modes we are able to identify three regimes (marked with vertical lines at 185 mins and at 203 mins in Fig. 4.3 and Fig. 4.4), that we will discuss now.

I) - The center of the micropillar is initially unoxidized and the oxide taper starts to penetrate inward. Only after six oxidation steps and a total oxidation time of 150

min has the oxide penetrated far enough that confined Hermite-Gaussian modes can be identified. The modes start to blueshift due to increasing optical confinement.

II) - The AlAs layer has oxidized all the way to the center of the micropillar and also the oxide taper in the $Al_{0.83}Ga_{0.17}As$ layer starts to penetrate inward. During this process a gradual blueshift of up to 30 nm is visible. Also a steady increase of the mode splitting and thus of the optical confinement continues until a maximum mode splitting of 4 nm is achieved, but then decreases again. This can indicate that the taper is not perfectly linear but has a larger slope in the center and is flatter at the start and the end of the taper.

III) - The AlAs and $Al_{0.83}Ga_{0.17}As$ layers in the oxide taper have been fully oxidized, but the oxidation in vertical directions still continues in the surrounding $Al_{0.75}Ga_{0.25}As$ layers aided by proximity enhancement effects [120]. The oxidation goes much slower, since it relies on the smaller oxidation rate of $Al_{0.75}Ga_{0.25}As$, but still gives rise to a gradient in the oxide thickness in the horizontal direction and thereby leads to confined modes. Surprisingly, this gradient is not sufficiently large to show up in the 1064 nm reflection scan.

To gain a quantitative understanding of the blueshift of the cavity modes, which we observe to be 32 nm after 205 min, we use the effective refractive index model [121]. For the refractive index of the oxide we use $n = 1.53$. Since the 10 nm AlAs layer is located at a node in the field only a 2.5 nm shift should occur when it is oxidized. The $Al_{0.83}Ga_{0.17}As$ is thicker and partly located at an antinode, giving a calculated shift of 24.9 nm. The $Al_{0.75}Ga_{0.25}As$ below the AlAs layer would give an additional shift of 15.5 nm if fully oxidized. However it is likely that only partial oxidation of this layer occurred, thereby contributing to the wavelength shift and the confining optical potential still present after 205 min.

Assuming a quadratic confining potential is present, the relationship between the waists of the modes and the mode splitting is given by: $\frac{\Delta\lambda_{10,01}}{\lambda_{00}} = \frac{1}{2}(\frac{\lambda_{00}}{n\pi w_{10,01}})^2$, where $\Delta\lambda_{10}/\Delta\lambda_{01}$ are the mode splittings between the Ψ_{10}/Ψ_{01} modes and the Ψ_{00} mode, λ_{00} is the wavelength of the Ψ_{00} mode, $n \approx 3.3$ is the average refractive index estimated from the device structure and w_{10}/w_{01} are the waists of the elliptically shaped fundamental mode. From the mode waists one can calculate the mode area $A = \frac{\pi}{4} w_{10} w_{01}$ and the cavity volume $V = L_{eff} * A$, where $L_{eff} \approx 1.4$ μm is the effective cavity length estimated from the device structure. At the end of regime I: $\Delta\lambda_{10} = 1.9$ nm, $\Delta\lambda_{01} = 2.3$ nm and $\lambda_{00} = 964$ nm. From this we find $A = 2.1$ μm^2 and $V = 2.9$ μm^3.

The quality factor Q of the fundamental optical mode is found by fitting a Lorentzian reflection dip to the reflectance spectra. At the end of regime I we measure quality factors as high as $Q = 14,000$, but this gradually decreases due to increased scattering by the oxide to $Q = 8,000$ at the end of regime II and decreases further to below $Q = 5,000$ after $t = 350$ mins.

An important figure of merit of microcavities is the Purcell factor $P = \frac{3}{4\pi^2}(\frac{\lambda_{00}}{n})^3 \frac{Q}{V}$. At the end of regime I where the quality factor is at a maximum, the estimated Purcell factor would be $P \approx 12$. This would be an optimal point to aim for.

4.5 Conclusion

In conclusion we demonstrated it is possible to repeat the oxidation of a micropillar multiple times, every time adding an extra bit of oxide to the aperture. This technique can be applied to tune the cavity wavelength more than 30 nm or to obtain mode splittings of up to 4 nm. In general this technique can be used to obtain desired optical properties with high accuracy.

This work was supported by NSF under Grant No. 0960331 and 0901886 and FOM-NWO Grant No. 08QIP6-2.

Chapter 5

Polarization degenerate micropillars fabricated by designing elliptical oxide apertures

A method for fabrication of polarization degenerate oxide apertured micropillar cavities is demonstrated. Micropillars are etched such that the size and shape of the oxide front is controlled. The polarization splitting in the circular micropillar cavities due to the native and strain induced birefringence can be compensated by elongating the oxide front in the [110] direction, thereby reducing stress in this direction. By using this technique we fabricate a polarization degenerate cavity with a quality factor of 1.7 $\times 10^4$ *and a mode volume of* 2.7 μm^3*, enabling a calculated maximum Purcell factor of 11.*

M. P. Bakker, A. V. Barve, A. Zhan, L. A. Coldren, M. P. van Exter, and D. Bouwmeester, Appl. Phys. Lett. **104**, 151109 (2014).

5.1 Introduction

Quantum dots in micropillar cavities form an interesting platform for cavity quantum electrodynamics experiments in the solid state [122]. For example, the coupling between the spin in a singly-charged quantum dot (QD) and the polarization of a photon in the Purcell regime holds promise for applications in hybrid quantum information processing [112]. For this purpose oxide apertured micropillars are attractive as they combine simple fabrication of voltage contacts, excellent mode-matching with external fields and access to the Purcell regime[98, 100].

An important challenge however is to obtain polarization degenerate cavity modes. This is an important condition in order to prepare entanglement between an electron spin and the polarization of a photon [6], which is essential for schemes as described in [112]. Several post-processing techniques have been demonstrated to tune the polarization properties. These techniques rely on the application of strain mechanically [123] or on the optical application of surface defects [94, 124]. It is more desirable to obtain close-to polarization degenerate cavities after the wet oxidation processing step and thereby minimize the need of further tuning.

In this Chapter we demonstrate that, by systematically varying the shape of the etched micropillar, the shape of the oxide aperture can be controlled, thereby controlling the spectral properties. Two arrays of micropillars of which the diameter and ellipticity are systematically varied are fabricated and the optical modes are

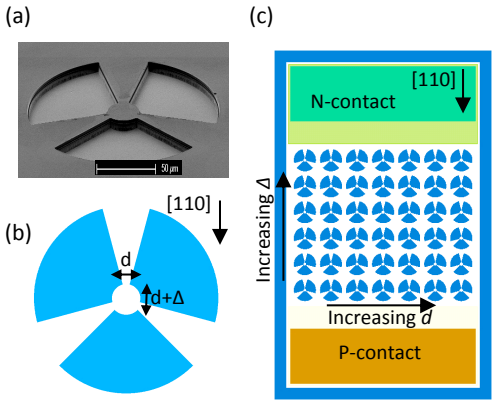

Figure 5.1: (a) SEM image of a micropillar. (b) The micropillars have diameter d and are elongated in the [110] direction by an amount $+\Delta$. (c) Systematic variations of d and Δ are applied over an array.

characterized at 9.0 K. Micropillars with circular oxide fronts exhibit optical modes with a large circular symmetry, but due to birefringence the fundamental mode is polarization non-degenerate. However, for elliptical oxide fronts that are elongated in the [110] direction, the native birefringence is compensated for by strain-induced birefringence and polarization degenerate fundamental modes are obtained.

5.2 Experiment

The samples used in this study are grown by molecular beam epitaxy on a GaAs [100] substrate. First a planar distributed Bragg reflector (DBR) cavity is grown which consists of a spacing layer and 26 pairs of GaAs/$Al_{0.90}Ga_{0.10}As$ layers in the top mirror and 29 pairs in the bottom mirror. The spacing layer consists of a λ GaAs layer, containing a layer of InAs self-assembled QDs in the center [105], and a $\frac{3}{4}\lambda$ $Al_xGa_{1-x}As$ aperture region. The oxidation aperture consists of a 10 nm AlAs layer embedded between 95 nm $Al_{0.83}Ga_{0.17}As$ and 66 nm $Al_{0.75}Ga_{0.25}As$ layers, providing a linearly tapered oxidation upon the wet oxidation. Micropillars are etched such that they are connected to the bulk region via three bridges, to provide global electrical contacts, as shown in Fig. 5.1 (a).

This geometry was found to be an optimum as for two bridges the oxide front is found to be more elliptically shaped, while for more than three bridges the bridges are too thin and the risk increases that the electrical conductance to the micropillar center is insufficient [99]. This geometry, together with the etching process, is however expected to induce in-plane anisotropic strain, which needs to be compensated for together with the native birefringence, that can be present even in perfectly circular mesas.

Figures 5.1 (b,c) schematically show that the micropillar diameter d in the $[1\bar{1}0]$ direction and diameter $d+\Delta$ in the [110] direction are systematically varied in a 6×7 array, with $d = [29, 30, 30.5, 31, 31.5, 32, 33]$ μm and $\Delta = [0, 0.5, 1.0, 1.5, 2.0, 2.5]$ μm. Then a wet thermal oxidation procedure to form an oxide aperture is applied

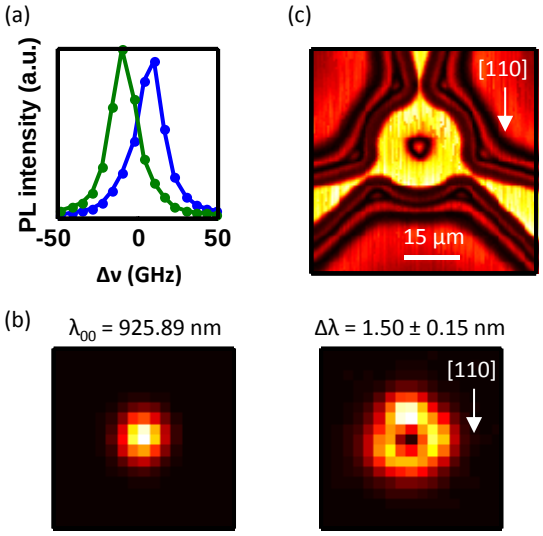

Figure 5.2: (a) PL from the fundamental Ψ_{00} mode at two orthogonal polarizations. (b) Spatial PL scans at the wavelength of the fundamental mode and a wavelength interval overlapping with both first-order modes. Wavelengths are selected using a spectrometer. (c) Spatial reflectivity scan of a focused $\lambda = 1064$ nm laser spot indicates the circular oxide front.

[110]. Finally electrical contacts to the p-doped and n-doped GaAs surrounding the QDs are fabricated.

To characterize the optical properties of the confined optical modes, standard microphotoluminescence techniques are used. The sample is held in a cryostat at 9.0 K and pumped using an 852 nm laser diode to excite QD emission. We characterize the anisotropy of every micropillar in two different ways. First of all, we measure the polarization-splitting of the fundamental mode to characterize the birefringence. Second, we measure the wavelength differences between the first-order transverse modes and the fundamental mode. This transverse mode splitting is linked to the optical confinement, which can be different in the two directions.

Finally, in order to get an indication of the shape of the buried oxide aperture layer, which determines the optical confinement, a spatial reflection scan is performed at room temperature. For this, a laser with a wavelength $\lambda = 1064$ nm located outside of the DBR stopband is used, such that the reflectance depends on interfering reflections from the top and bottom DBR mirrors. This interference is a function of the optical length of the spacing layer and therefore the reflectance depends on the buried oxide thickness [118]. The front of the oxide is clearly visible as a ring with a lower reflectivity.

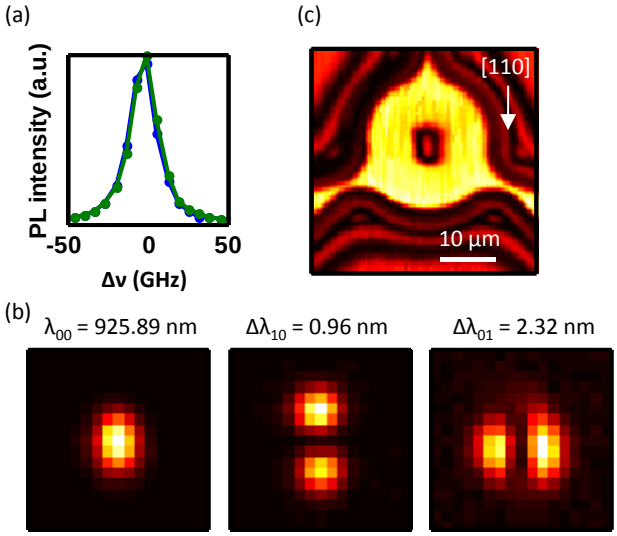

Figure 5.3: (a) PL from a polarization degenerate Ψ_{00} cavity mode. (b) Spatial PL scans of the fundamental Ψ_{00} and the first-order Ψ_{10} and Ψ_{01} modes. (c) Spatial $\lambda = 1064$ nm reflectivity scan that indicates the oxide front is elongated in the [110] direction.

5.3 Results

Figure 5.2 shows a micropillar that was elongated slightly, by 0.5 μm, in the [110] direction. Due to a faster wet oxidation rate in this direction this results in a nearly circular oxidation front as shown in Fig. 5.2 (c). The circular symmetry is apparent as well in the spatial profiles of the confined modes in Fig. 5.2 (b), where the incoherent sum of the two first higher-order Hermite-Gaussian modes resemble a Laguerre-Gaussian transverse mode profile. In Fig. 5.2 (a) however a clear frequency splitting between two linear orthogonal polarization modes of the fundamental mode is visible due to birefringence.

Figure 5.3 shows an even more elliptical micropillar, elongated in the [110] direction by 2 μm. This elongated shape is now also visible in the shape of the buried oxide aperture in Fig. 5.3 (c). In Fig. 5.3 (b) clear Hermite-Gaussian modes are identified that now posses a great difference between the modesplittings $\Delta\lambda_{10(01)} = \lambda_{00} - \lambda_{10(01)}$, owing to a difference in the amount of optical confinement in orthogonal directions. We define $\Delta\lambda_{10}$ to be in the [110] direction. The polarization splitting of the fundamental mode however is about 1 GHz, less than 6% of the FWHM, indicating the birefringence has been strongly reduced.

Figure 5.4 shows the result of a systematic characterization of two arrays, of which array 2 is oxidized slightly further. Figure 5.4 (a) shows the modesplittings between the fundamental and first order modes, averaged over the two linear polarizations. Clearly, the average modesplitting decreases as the size of the micropillar is increased, as expected. Figure 5.4 (b) shows the ratio $\Delta\lambda_{01}/\Delta\lambda_{10}$ between the modesplittings in

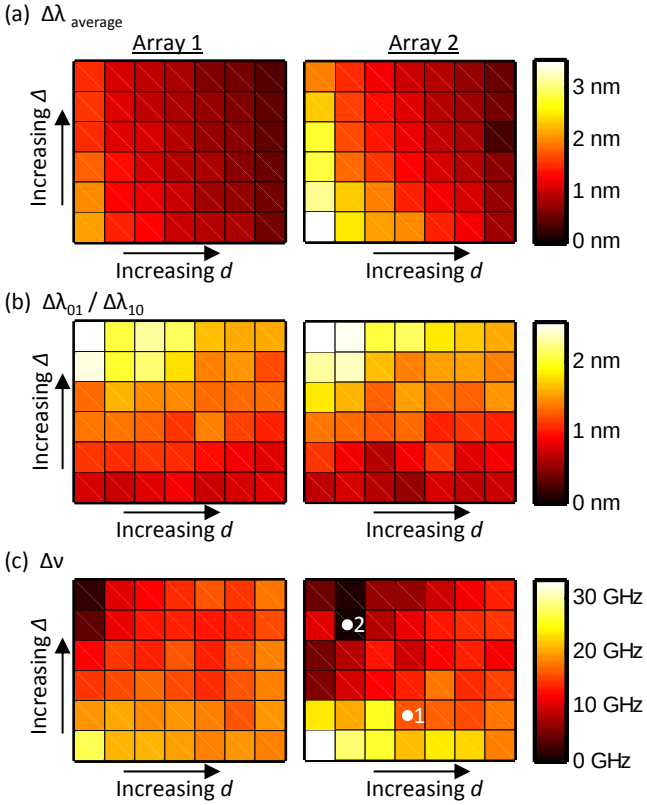

Figure 5.4: Colormaps indicate from two arrays: (a) the average modesplittings $\Delta\lambda_{average}$ between the first order Ψ_{10}/Ψ_{01} modes and the fundamental Ψ_{00} mode, (b) the ratio $\Delta\lambda_{01}/\Delta\lambda_{10}$ of the modesplittings between the Ψ_{01}/Ψ_{10} and the Ψ_{00} modes, and (c) the polarization splitting $\Delta\nu$ of the Ψ_{00} mode. Array 2 exhibits a larger average modesplitting and thus has oxidized slightly further. The dots 1 and 2 denote the cavities displayed in Fig. 5.2 and Fig. 5.3, respectively.

two directions. An increasing ratio $\Delta\lambda_{01}/\Delta\lambda_{10}$ corresponds to less optical confinement in the [110] direction with respect to the [1$\bar{1}$0] direction which arises from a more elongated oxide front. This correlates with increasing Δ. Figure 5.4 (c) displays the polarization splitting $\Delta\nu$ of the fundamental Ψ_{00} mode. A clear relation is visible between $\Delta\lambda_{01}/\Delta\lambda_{10}$ and $\Delta\nu$.

5.4 Discussion

We qualitatively explain our findings by a modification of the birefringence under the influence of uniaxial strain in the [110] direction [124]. Even for the almost circular apertures that remains after oxidation, some uniaxial strain is expected as the oxide layer is more extended in the [110] direction. This can be the result of an anisotropy of the oxidation rate in combination with the location of the three bridges. When the oxide front is more elongated however we expect the strain to be reduced such that the birefringence can be fully compensated for.

An important figure of merit of microcavities is the Purcell factor. For the cavity shown in Fig. 5.3 we find a Q-factor of $Q \approx 1.7 \times 10^4$ and by following methods described in [103] we predict that a maximum Purcell factor of 11 can be achieved.

We would like to remark that shape birefringence due to anisotropic confinement is small (< 1 GHz) in our micropillars and a paraxial (and scalar) description practically suffices. The polarization/vector correction to the scalar wave equation, as calculated from perturbation theory [125, 126], predicts that the shape-induced birefringence of the fundamental mode is a factor $(\Delta\lambda_{01} + \Delta\lambda_{10})/(2\lambda_{00})$ smaller than the shape-induced confinement splitting $(\Delta\lambda_{01} - \Delta\lambda_{10})$, which results in a value of 0.84 GHz for the numbers mentioned in Fig. 5.3.

5.5 Conclusion

In conclusion we have shown it is possible to control the shape of the oxide aperture by the shape of the micropillar. By applying systematic variations in the etched shapes, the strain-induced birefringence is varied and polarization degenerate cavities are obtained. This is an appealing approach towards fabrication of polarization degenerate microcavities with minimal post-processing tuning techniques required.

We thank Thomas Ruytenberg for experimental assistance. This work was supported by NSF under Grant No. 0960331 and 0901886 and FOM-NWO Grant No. 08QIP6-2.

Chapter 6

Polarization degenerate solid-state cavity QED

A polarization degenerate microcavity containing charge-controlled quantum dots (QDs) enables equal coupling of all polarization degrees of freedom of light to the cavity QED system, which we explore through resonant laser spectroscopy. We first measure interference of the two fine-split neutral QD transitions and find very good agreement of this V-type three-level system with a coherent polarization dependent cavity QED model. We also study a charged QD that suffers from decoherence, and find also in this case that availability of the full polarization degrees of freedom is crucial to reveal the dynamics of the QD transitions. Our results pave the way for postselection-free quantum devices based on electron spin–photon polarization entanglement.

M. P. Bakker, A. V. Barve, T. Ruytenberg, W. Löffler, L. A. Coldren, D. Bouwmeester, and M. P. van Exter, Phys. Rev. B **91**, 115319 (2015).

6.1 Introduction

Quantum dots (QDs) embedded inside microcavities are of interest for hybrid optical-solid-state quantum information schemes [127, 128], and long-distance quantum networks [13, 129]. A key ingredient is the realization of entanglement between a QD-spin and a single photon. Several experiments have demonstrated this by utilizing spontaneous emission [6, 7, 130], but these methods require postselection and are therefore not suitable for deterministic approaches. The need for postselection can be eliminated by using the spin-dependent reflection or transmission of a photon by a quantum dot in a cavity QED system. Several protocols have been proposed that either require polarization degenerate microcavities in order to couple with circular polarized light [112, 131], or would be aided in order to match more easily with linear polarized transitions [132]. Further key system requirements are charge controlled QDs and access to the Purcell or strong coupling regimes, which has been realized in photonic crystal cavities [84] and micropillars [100]. Micropillars have the additional benefit of mode-matching to external fields and polarization control of the cavity modes [32, 82, 98, 99, 122, 133].

In this Chapter we report on a system exhibiting all these features, being a charge controlled quantum dot coupled to a polarization degenerate micropillar cavity. The microcavity consist of two distributed Bragg reflectors, a $3/4\lambda$ thick aperture region

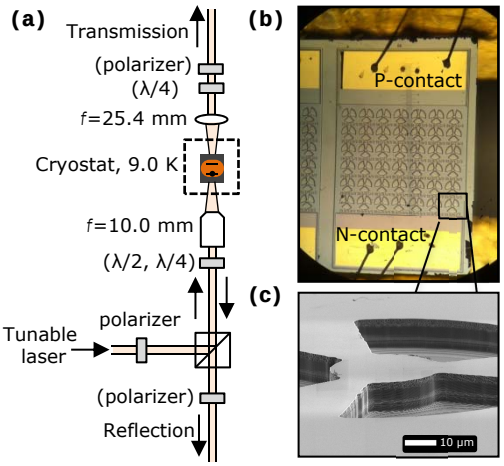

Figure 6.1: (a) Schematic of the setup. Light is coupled into a microcavity mode and the reflection and transmission spectra are recorded using single-photon avalanche photodiodes. The elements with names between brackets can be introduced for polarization analysis with either linear or circularly polarized light. $\lambda/2$ ($\lambda/4$): half- (quarter-) waveplate. (b) Optical microscope image of a sample and (c) Electron micrograph of the cavity region.

for transverse mode confinement, and a λ thick cavity layer, containing InAs self-assembled QDs embedded inside a PIN-diode structure [98, 105]. By systematically varying the size and shape of the oxide aperture, we were able to select on average one polarization degenerate cavity (polarization splitting <3 GHz) out of an (6×7) array [96]. This technique could be combined with a technique to actively tune the polarization properties by applying laser-induced surface defects [94], to enhance the sample yield. We tune the QD transition through the cavity resonance by the quantum confined Stark effect, induced by an applied bias voltage across the active region [134, 135]. In principle this can be combined with other QD tuning techniques, such as strain tuning [90, 95, 136], which would further increase the sample yield. Further details on the sample structure and characterization can be found in the Appendix 6.5. The setup, an optical, and an electron microscope image of the sample are shown in Fig. 6.1.

This system enables polarization resolved studies, which, as we will demonstrate, provides insight in the excitonic coherence of the system. First we study the coherent interaction of charge-neutral quantum dot transitions with resonant laser light and give a theoretical description. Then we investigate a singly charged QD and study its more complex dynamics, which we can describe with a second, decoherent model where all spin-photon entanglement is lost.

6.2 Neutral quantum dot

The lowest energy levels of a neutral QD are depicted in Fig. 6.2 (e). Due to the QD anisotropy, the electron-hole exchange interaction leads to a fine-structure

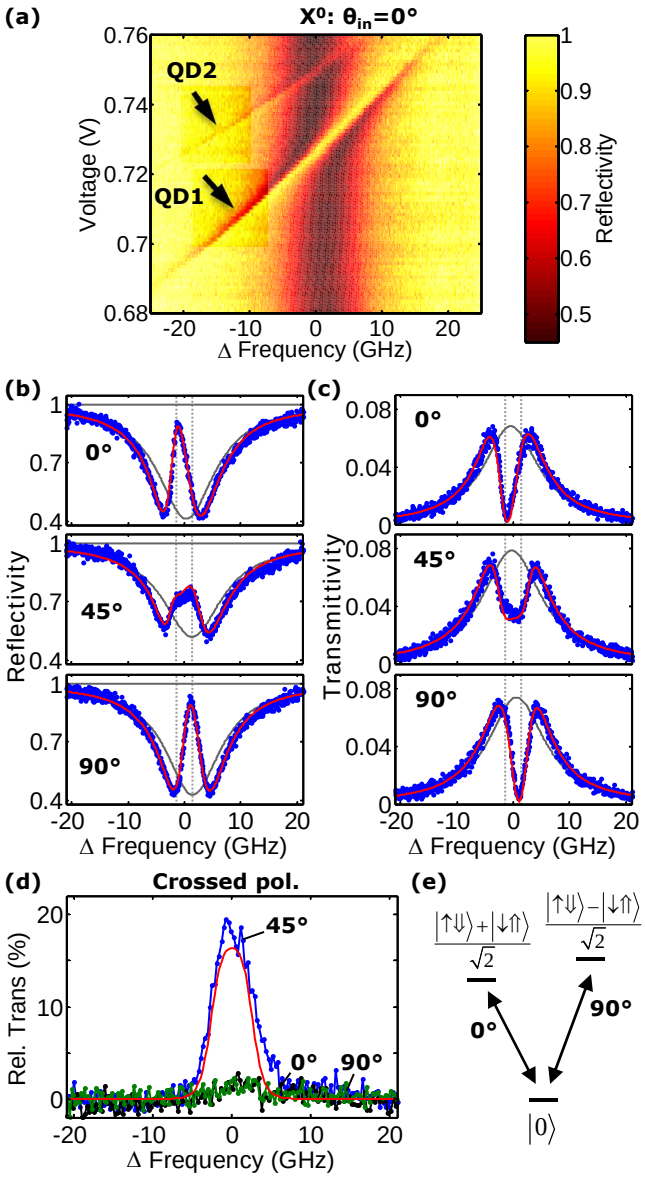

Figure 6.2: (a) Reflectivity measurement of two neutral QDs as function of the scanning laser frequency and applied voltage. The incoming polarization $\theta_{in} = 0°$, $P_{laser} = 1$ pW and $\lambda \approx 940$ nm. Panel (b, c) show reflectivity and transmittivity spectra of QD1 recorded at $V = 0.725$ V for various incoming linear polarizations. Blue points: experimental data. Red line: fitted curve using Eqs. 6.1 and 6.2. Grey curve: empty cavity, calculated from the fits. Vertical dashed lines: frequencies corresponding to the two fine-split transitions. (d) Transmittivity spectra when a crossed polarizer is used with respect to the incoming polarization, relative to the maximum transmittivity of an uncoupled cavity. The red line is calculated using Eqs. 6.1 and 6.2 and the parameters obtained from the fits in (b, c). (e) Energy level diagram of the ground-state and lowest energy excited states of a neutral QD.

splitting of the excited states (~ 3 GHz for the QD under study), the neutral ground state is coupled to two excited states by two linear orthogonally polarized transitions. In the resonant reflection measurements in Fig. 6.2 (a), the QD-cavity anti-crossing, as a hallmark of strong to intermediate QD-cavity coupling, is clearly visible. Low laser power ($P_{laser} = 1$ pW) is used in order to avoid saturation of the QD transition, charging [137] and dynamical nuclear spin polarization effects [138]. Fig. 6.2 (b, c) show reflection and transmission spectra for a voltage V=0.725 V, where QD1 is tuned into resonance with the cavity. The spectra are recorded for three linear polarizations that couple either with the low frequency QD transition ($\theta_{in} = 0°$), or the high frequency QD transition ($\theta_{in} = 90°$), or both QD transitions ($\theta_{in} = 45°$).

For 0° and 90° polarization we observe that the quantum dot is able to restore high cavity reflectivity with near-unity fidelity, but this effect appears to be reduced for 45°. Additionally we show spectra when a crossed polarizer is used in the transmission path in Fig. 6.2 (d). We see that for 0° and 90° the light matches the natural polarization axes of the QD and that this polarization is maintained, resulting in a very low signal. For 45° incoming polarization the transmission is significant however. In the following, we develop a theoretical model to gain insight into the dynamics.

The transmission amplitude through a cavity with a coupled two-level system is given by [37, 133, 139]:

$$t = \eta_{out} \frac{1}{1 - i\Delta + \frac{2C}{1-i\Delta'}}, \tag{6.1}$$

where $\Delta = 2(\omega - \omega_c)/\kappa$ is the relative detuning between the laser (ω) and cavity (ω_c) angular frequencies, $\Delta' = (\omega - \omega_{QD})/\gamma_\perp$ is the relative detuning between the laser and QD transition (ω_{QD}) and η_{out} is the output coupling efficiency. The device cooperativity is $C = g^2/\kappa\gamma_\perp$ where, κ is the total intensity damping of the cavity, $\gamma_\perp$ is the QD dephasing rate and g is the QD-mode coupling strength. We obtain close to perfect mode-matching, and therefore the total transmittivity through the cavity is given by $T = |t|^2$, and the total reflectivity is given by $R = |1-t|^2$. A more detailed description of Eq. (6.1) is provided in Appendix 6.6.

An important figure of merit of the QD-cavity system is the cooperativity parameter C. By fitting our model to the experimental data in Fig. 6.2 for $\theta_{in} = 0°$ and $\theta_{in} = 90°$, we find $C = 2.5 \pm 0.5$, a value similar to previously reported [133]. We also obtain $\gamma_\perp = 2.0 \pm 0.5$ ns^{-1}, which corresponds to a total dephasing time $\tau = 500$ ps, and total cavity damping rate $\kappa = 77$ ns^{-1}, which corresponds to a quality factor of $Q \sim 2.6 * 10^4$, see Appendix 6.6. Since $\gamma_\perp < 2g = 39$ ns$^{-1} < \kappa$, this places the system in the intermediate coupling regime.

The lineshapes corresponding to an empty cavity can be calculated from the fitted curves and are shown by the grey curves in Fig. 6.2 (b,c). The very small dependence of the cavity resonance frequency on the polarization angle confirms the high degree of polarization isotropy of this device.

To account for the fine-structure splitting of the neutral QD transitions in the polarization-degenerate cavity, we write the transmission of the system in terms of a Jones matrix $\mathbf{t}(\omega) = \begin{pmatrix} t_x(\omega) & 0 \\ 0 & t_y(\omega) \end{pmatrix}$. The measured transmittivity therefore depends

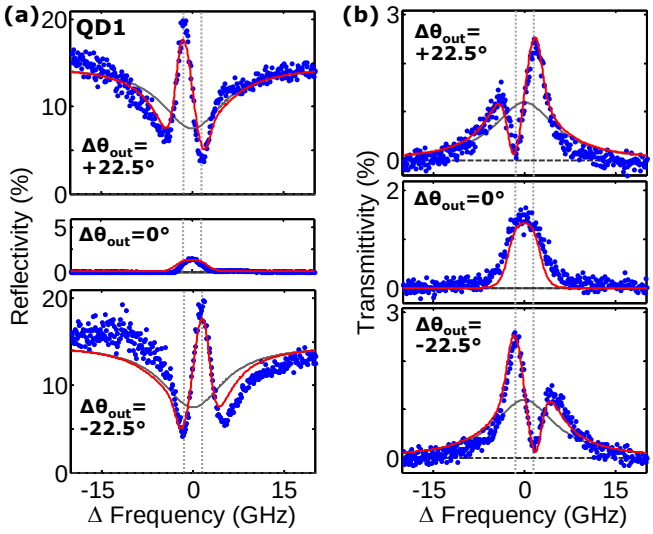

Figure 6.3: Resonant (a) reflection and (b) transmission spectroscopy with a neutral QD (QD1 in Fig. 6.2) for $\theta_{in} = 45°$ and for various $\theta_{out} = \theta_{in} + 90° + \Delta\theta_{out}$. Blue dots: experimental data. Red lines: predicted curves using Eqs. 6.1 and 6.2 and the parameters obtained from the fits in Fig. 6.2 (b,c). Grey lines: predicted curves corresponding to an empty cavity. Vertical dashed lines mark the two transitions split by the fine-structure interaction.

on the input and output polarization as

$$t_{\theta_{out},\theta_{in}}(\omega) = \mathbf{e}_{out}^{\dagger}\mathbf{t}(\omega)\mathbf{e}_{in}, \tag{6.2}$$

where $\boldsymbol{e_i} = (cos(\theta_i), sin(\theta_i))$ defines the linear input/output (i =in/out) polarization with angle θ_i. This model assumes that when the two transitions are excited simultaneously ($\theta_{in} = 45°$), coherence in the system is fully maintained leading to quantum interference between the transmission amplitudes t_x and t_y. In an incoherent system we would obtain a classical mixture of the excited states, making such interference impossible. The reflectivity is calculated in a similar way by using $r_{x/y} = 1 - t_{x/y}(\omega)$ in the Jones matrix.

To further explore the validity of Eq. (6.2) and to demonstrate the full power of polarization degenerate cavity QED, we show in Fig. 6.3 (a, b) reflection and transmission spectra for $\theta_{in} = 45°$, while $\theta_{out} = \theta_{in} + 90° + \Delta\theta_{out}$ is varied. For $\Delta\theta_{out} = 0°$, the crossed polarizer condition, the transmission and reflection spectra consist of two partially overlapping Lorentzian lines split by ∼3 GHz. The phase difference between these two resonances becomes apparent for the $\Delta\theta_{out} = +22.5°$ ($-22.5°$) spectra, which can be seen as the *coherent sum* of the $\Delta\theta_{out} = 0°$ and the $\Delta\theta_{out} = +45°$ ($-45°$) spectra, where the latter only contains the high (low) frequency transition. All the red curves in Fig. 6.2 and 6.3 are produced with the same parameters for C, κ and $\gamma_{\perp}$ and fit the experimental data very well. The results demonstrate how in a polarization degenerate cavity the fine-split excited states of a

neutral QD can be simultaneously addressed in a coherent way. Furthermore, these interference measurements hold great promise as a clever combination of $\mathbf{e}_{in}$ and $\mathbf{e}_{out}$ can be used to tune the constructive or destructive interference between t_x and t_y. This forms a generic technique to increase the ratio between an uncoupled and a coupled cavity system, and thereby the fidelity of entanglement operations.

6.3 Singly-charged quantum dot

Now we turn to a different QD in the same polarization degenerate cavity, but operated in a voltage regime around 0.9 V where it is singly negatively charged. This system is of particular importance in quantum information as the optical transitions are polarization degenerate (see Fig. 6.4 (a)), due to cancellation of electron-hole exchange interaction, and enables coherent control of the resident electron spin if a small in-plane magnetic field is applied. We first focus on Fig. 6.4 (b, c), which shows transmission spectra when circularly (σ^+) or linearly polarized light is coupled into the cavity and transmitted light of the same (i.e., parallel) polarization is recorded. We define the contrast as $(|t_c|^2 - T)/|t_c|^2$, with the measured transmittivity T with a QD and the calculated transmittivity $|t_c|^2$ without a QD. While for the neutral QD case we found contrasts of $> 91\%$ in Fig. 6.2 (c), we now observe a strongly reduced contrast of the QD resonance, which is $\sim 19\%$ when circularly polarized light is used and $\sim 26\%$ for linear polarization.

We use a slightly larger laser power ($P_{laser} = 10$ pW) compared to the neutral QD as we find that the charging effects are now significantly smaller, due to less absorption of the resonant laser at this voltage. Furthermore, this intensity corresponds to a mean intracavity photon number $\langle \bar{n} \rangle = |t|^2 P_{laser}/(\kappa_m \hbar\omega) < 0.001$, and is therefore sufficiently small to prevent QD saturation effects from occurring.

In addition, we compared the cross-polarized transmitted intensity for circular and linear polarized light. For circular (σ^+ and σ^-) polarization, shown in Fig. 6.4 (d), we observe negligible transmission, indicating that circular polarization remains unchanged. Surprisingly, for two linear orthogonal (lin1 and lin2) polarizations displayed in Fig. 6.4 (e), we observe that about 10% of the light is transmitted relative to $|t_c|^2$, despite the low cooperativity (see below).

We will first try to explain our observations with a coherent model, which we adapt to the four-level system of a charged QD shown in Fig. 6.4 (a): The ground state consists of the two spin eigenstates, oriented in the out-of-plane direction, which couple with two corresponding trion lowest-energy excited states by degenerate circularly polarized optical transitions carrying spin $\sigma^\pm = \pm 1$. We write $t_1^\pm \equiv t_1$ for the corresponding transmission amplitudes of $\sigma^\pm$ polarized light coupling with a corresponding transition, and $t_c^\pm \equiv t_c$ for the case of an empty cavity. Since we do not control the electron spin state it can be in any random state $|\phi_{spin}\rangle = \alpha\,|\uparrow\rangle + \beta\,|\downarrow\rangle$. With the incoming photon state $|\phi_{in}\rangle = \gamma\,|+\rangle + \delta\,|-\rangle$, we obtain for the input quantum state $|\Psi_{in}\rangle = |\phi_{in}\rangle \otimes |\phi_{spin}\rangle$. The spin-selective interaction with the cavity-QD system entangles the photon with the electron spin via

$$|\Psi_{out}\rangle = t_1\gamma\alpha\,|+\uparrow\rangle + t_c\gamma\beta\,|+\downarrow\rangle + t_c\delta\alpha\,|-\uparrow\rangle + t_1\delta\beta\,|-\downarrow\rangle\,. \tag{6.3}$$

We then project this output state onto the detected polarization $|\phi_{out}\rangle = \gamma'\,|+\rangle +$

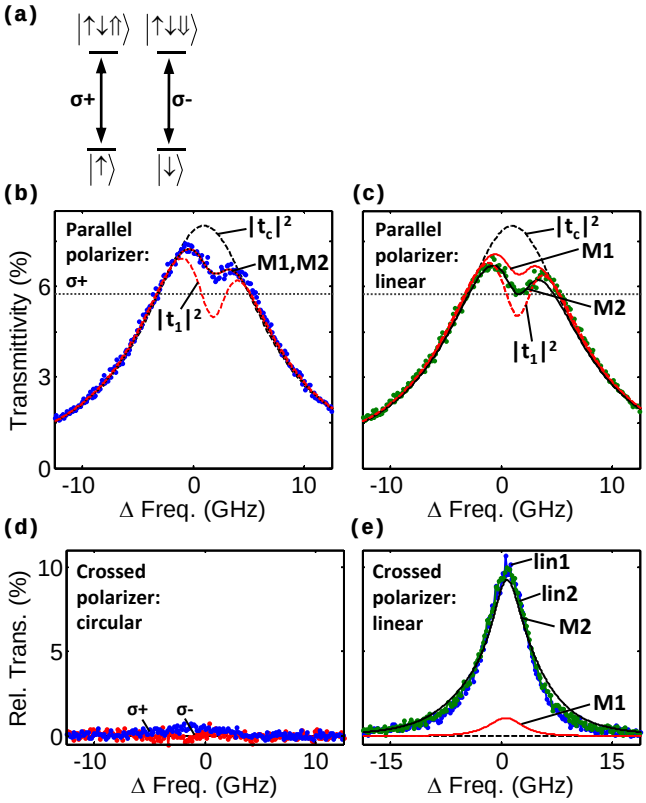

Figure 6.4: (a) Energy-level diagram of a singly charged QD. Transmission spectra for $P_{laser} = 10$ pW are shown for circular and linear polarization, analyzed with a (b) and (c) parallel or (d) and (e) crossed polarizer. The red-black dashed line in (b) is a fit of Eq. (6.4) (coherent model, M1) to the data, which yields the same result as Eq. (6.5) (decoherent model, M2). The red (black) solid lines in (c) and (e) predict the experimental data using Eq. (6.4) [Eq. (6.5)]. Black (red) dashed curves: empty (coupled) cavity calculations.

$\delta' |-\rangle$, and take the trace over the electron spin to obtain the projected transmission:

$$T = |t_1\gamma\gamma' + t_c\delta\delta'|^2|\alpha|^2 + |t_c\gamma\gamma' + t_1\delta\delta'|^2|\beta|^2. \tag{6.4}$$

Since we do not control the spin state we use $|\alpha|^2 = |\beta|^2 = 0.5$ for the balanced case. Note that this model (M1) is coherent in the sense that it still contains interference between the t_1 and t_c terms.

The red through line in Fig. 6.4 (c) shows how model M1 fits our data for the optimum cavity-QD coupling and QD dephasing parameters $C = 0.13$ and $\gamma_\perp = 9.5$ ns^{-1}. The dephasing rate can not be explained by the decay rate of the excited state, since lifetime measurements showed this to be about 1.2 ns. Instead, we attribute this much faster dephasing rate to an efficient cotunneling process across the 20 nm electron tunnel barrier, which is expected to be more pronounced for the flatter conduction band here compared to the neutral QD case presented before. This fast dephasing also reduces the cooperativity, which, however, might also be reduced due to low spatial overlap between the QD and the cavity mode. We expect that utilizing a thicker 35 nm tunnel barrier will decrease the cotunneling process and enable high fidelity spin state preparation [107].

Next we consider the linear-polarization data shown in Fig. 6.4 (c,e), where the model prediction is shown by red lines. Eq. (6.4) predicts that purely circular polarized light should pass the cavity unmodified, and can therefore be fully blocked by a crossed polarizer ($\gamma\gamma' = \delta\delta' = 0$), which is indeed what we observe experimentally in Fig. 6.4 (d). Significant discrepancies between the data and our model are however observed in Fig. 6.4 (c) and in (e) particularly, where the cross-polarized transmission signal for linear-polarizations lin1 and lin2 is much larger than expected. This can not be caused by an energy splitting, or phase difference, between the two transitions, as these splittings would have been visible in the data. Furthermore, the observed cross-polarized transmission is so large that it would require $C > 0.8$ in Eq. (6.4) to explain the cross-polarized transmission in Fig. 6.4 (e), while we found $C = 0.13$ for the fit in Fig. 6.4 (b).

This result therefore indicates that additional dephasing processes take place that project linear polarized light on the preferred circular basis of the QD transitions. The preference for this basis is known from literature Refs. [71, 107, 140] and is experimentally demonstrated by the fact that circular polarized light remains circular polarized after the interaction with the QD–cavity system. If the absorption and reemission of linear light would be a fully coherent process, the linear polarization should largely remain, which is clearly not the case in Fig. 6.4 (e).

To model the results, we now introduce a tentative model (M2) that describes the spin-exciton system as if it were fully decoherent, meaning that any light interacting with the QD is instantaneously projected on the QD transition polarization basis. This corresponds to immediate decoherence of the entangled state described by Eq. (6.3) and elimination of interference between the t_1 and t_c terms in Eq. (6.4). Since only a fraction of the light that enters the cavity becomes entangled with the QD spin state, we first need to calculate the fraction of the light that did not interact. We estimate this fraction T_0 by multiplying the cavity transmission with the QD

response function: $T_0 = |t_c|^2 \times |\frac{1}{1+\frac{2C}{1-i\Delta'}}|^2$. The intensities of the circularly polarized components of the transmitted light that interacted with a parallel or opposite electron spin are now given by $T_1' = |t_1|^2 - T_0$ and $T_c' = |t_c|^2 - T_0$, respectively.

The total transmitted intensity corresponds now to the incoherent sum of five transmission channels:

$$\begin{aligned} T = T_0 |\langle \phi_{out} | \phi_{in} \rangle|^2 + T_1' |\gamma\alpha \langle \phi_{out} | + \rangle|^2 + T_c' |\delta\alpha \langle \phi_{out} | - \rangle|^2 \\ + T_c' |\gamma\beta \langle \phi_{out} | + \rangle|^2 + T_1' |\delta\beta \langle \phi_{out} | - \rangle|^2. \end{aligned} \tag{6.5}$$

The transmission predicted by the incoherent model (M2, Eq. (6.5)) and coherent model (M1, Eq. (6.4)) are equivalent in case of circular incoming polarization (Fig. 6.4 (b,d)). They differentiate however in case of the linear-polarization data in Fig. 6.4 (c,e). The solid black curves predicted by the incoherent model (M2), based on the parameters deduced from Fig. 6.4 (b), agrees very well while the coherent model (M1) does not.

While the polarization degenerate microcavities enables systematic polarization analysis and the identification of a high degree of decoherence in the charged QD system, the exact origin of decoherence is not known to us. We think it is related to the cotunneling process and future sample designs with thicker tunnel barriers will resolve this issue.

6.4 Conclusion

In conclusion, we have demonstrated a polarization degenerate solid-state cavity QED system with charge control, which allows full use of all polarization degrees of freedom. Here, simple polarimetric reflection and transmission measurements enable the study of the coherence properties of the coupled QD–cavity system, for neutral and charged quantum dots. This is an important advance for fundamental studies of spin dynamics and optical interactions in solid-state cavity QED systems, and an important step towards quantum information applications with single electron and hole spin qubits, and postselection-free spin–photon polarization interaction.

6.5 Appendix A: Sample structure and characterization

The sample under study has been grown by molecular beam epitaxy on a GaAs [100] substrate. Two distributed Bragg reflectors (DBR) surround an aperture region and a λ thick cavity region containing in the center InAs self-assembled quantum dots (QDs). The top DBR mirror consists of 26 pairs of $\lambda/4$ layers of GaAs and $Al_{0.90}Ga_{0.10}As$, while the bottom mirror consists of 13 pairs of layers of GaAs and AlAs and 16 pairs of GaAs and $Al_{0.90}Ga_{0.10}As$ layers. This way the reflectivities of top and bottom mirrors are matched in order to enable transmission and reflection measurements and optimize the incoupling efficiency. The oxidation aperture consists of a 10 nm AlAs layer embedded between 95 nm $Al_{0.83}Ga_{0.17}As$ and 66 nm $Al_{0.75}Ga_{0.25}As$ layers, providing a linearly tapered oxidation upon wet oxidation. The QDs are separated by a 20 nm GaAs tunnel barrier to n-doped GaAs (Si dopant, concentration 2.0×10^{18} cm^{-3}) and by a 107 nm GaAs to p-doped GaAs (C doping, concentration 1.0×10^{18} cm^{-3}).

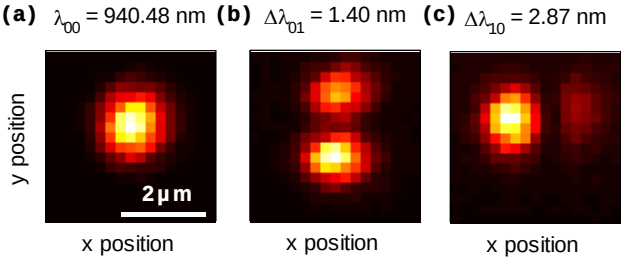

Figure 6.5: Spatial PL scans of the Hermite-Gaussian modes, where (a) is the fundamental mode Ψ_{00} and (b,c) the first order Ψ_{10}/Ψ_{01} modes. Light: more PL counts. The captions denote the wavelength λ_{00} of the fundamental mode, or the wavelength splitting $\Delta\lambda_{10/01} = \lambda_{00} - \lambda_{10/01}$.

By analyzing the confined optical modes and the wavelength splitting between the fundamental and first order optical modes, an estimation can be made of the maximum Purcell factor and the numerical aperture (NA) of the fundamental mode. A high Purcell factor is necessary to observe QD couplings close to the strong coupling regime, while a modest NA enables perfect mode-matching to external fields.

To characterize the optical properties of the confined modes, the sample is excited using an 852 nm laser diode and photoluminescence as function of position is recorded using a spectrometer. Hermite-Gaussian modes are clearly identified in Fig. 6.5. Following methods described in [103] we calculate the mode volume V using:

$$V = L_{cav}\frac{\lambda_{00}^3}{8\pi n_0^2\sqrt{\Delta\lambda_{01}\Delta\lambda_{10}}}, \tag{6.6}$$

where $L_{eff} \approx 5\lambda_{00}/n \approx 1.4$ μm is the effective cavity length, $\lambda_{00} = 940.48$ nm is the wavelength of the fundamental mode in vacuum, $n \approx 3.25$ is the average refractive index, and $\Delta\lambda_{01/10}$ are the mode splittings between the $\Psi_{01/10}$ modes and the Ψ_{00} mode. Filling in the experimentally obtained values for the modesplitting, we obtain $V = 2.2$ μm^3. The expected maximum Purcell factor P is given by:

$$P = \frac{3}{4\pi^2}(\frac{\lambda_{00}}{n_0})^3\frac{Q}{V}, \tag{6.7}$$

where $Q = 2.6 * 10^4$ is the quality factor measured during the resonant spectroscopy scans. Using the above mentioned values we find $P = 22$. The intensity of the fundamental mode, perpendicular to the propagation direction $\hat{z}$, has the form: $I \propto \exp[-2(\frac{x^2}{w_x^2} + \frac{y^2}{w_y^2})]$, where $w_{x/y} = \frac{1}{n_0\pi}\sqrt{\frac{\lambda_{00}^3}{2\Delta\lambda_{10/01}}}$ is the mode waist. The numerical aperture of the Gaussian beam originating from the fundamental mode is given by $\mathrm{NA}_{x/y} = \sin(\frac{\lambda_{00}}{\pi W_{x/y}})$, which gives $\mathrm{NA}_x = 0.18$ and $\mathrm{NA}_y = 0.25$. The NA of the used objective 0.4, enabling perfect mode-matching.

6.6 Appendix B: Complete description of the transmission amplitude

The transmission amplitude through a cavity with a coupled QD is given by [37, 133, 139]:

$$t = \eta_{out} \frac{1}{1 - i\Delta + \frac{2C}{1 - i\Delta'}}, \tag{6.8}$$

where the parameters are defined in the main text. We will here quantify the role of losses and its effect on the out-coupling efficiency $\eta_{out} = \frac{2\kappa_m}{\kappa}$, defined as the probability that a photon in the mode will leave the cavity through the top or bottom mirror. Here κ_m is the damping rate of each Bragg mirror, κ_s is the scattering and absorption rate inside the cavity, and $\kappa = 2\kappa_m + \kappa_s$ is the total cavity intensity damping rate. Furthermore $\kappa_m = T_{mirror}/t_{round}$, where T_{mirror} is the transmittivity of a single mirror and $t_{round} = 2nL_{cav}/c$ is the cavity round trip time. n is the average refractive index, $L_{cav} \approx 5\lambda/n$ is the effective cavity length, c is the speed of light and $\lambda \approx 940$ nm is the wavelength in vacuum.

The mirror damping rate $\kappa_m \approx 11$ ns^{-1} is calculated from the sample design parameters. Three observations consistently yield $\kappa_s \approx 55$ ns^{-1}: (i) the measured quality factor $Q \approx 2.6 \times 10^4$ is lower than $Q = 9.1 \times 10^4$ as determined by the mirror transmittivity $T_{mirror} = 3.4{*}10^{-4}$ and cavity length, and corresponds to $\kappa = 77$ ns^{-1}, (ii) the minimum reflectivity of the empty cavity $\frac{R_{min}}{R_{max}} = |1 - \eta_{out}|^2 \approx 0.5$, and (iii) the maximum transmission $T_{max} = |\eta_{out}|^2 \approx 0.08$, (not taking into account a $\sim 30\%$ reflectivity at the GaAs to air interface at the back of the sample). We attribute this scattering rate κ_s to (spectrally broad) absorption losses in the doped layers and scattering by the oxide aperture. Reducing κ_s, for example by using a lower doping concentration, is a major concern in future sample designs.

Finally we will comment on the case of non-perfect mode matching. The total transmission T through the cavity is then given by $T = \eta_{in}\eta_T|t|^2$, where η_{in} is the in-coupling efficiency and η_T is the collection efficiency at the transmission port. The total reflection is given by $R = \eta_R|1 - \eta_{in}t|^2$, where η_R is the collection efficiency at the reflection port. In case of perfect mode matching $\eta_{in} = \eta_R = \eta_T = 1$.

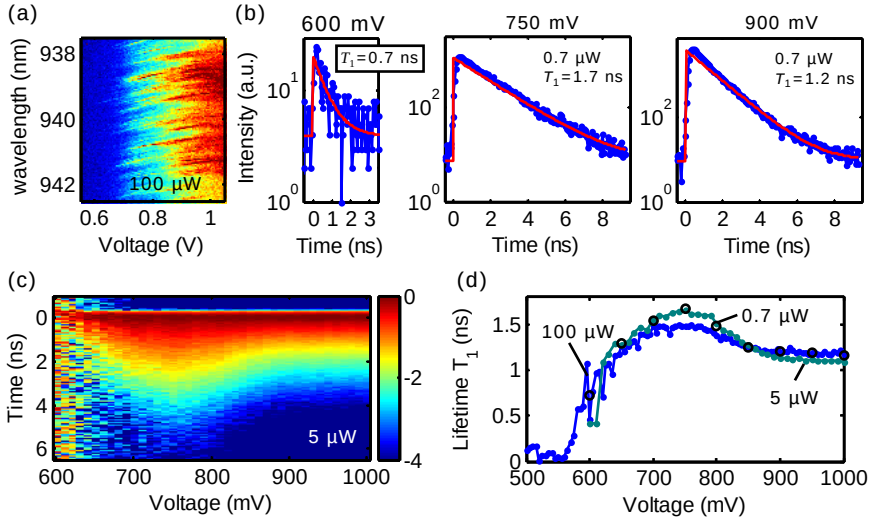

Figure 6.6: Lifetime measurements on an ensemble of QDs. (a) shows a colormap of the photoluminescence (PL) as function of wavelength and voltage. (b) shows lifetime traces for three voltages. Red lines are fit using $y = A\exp(-t/T_1) + B$. (c) displays a colormap of the normalized PL intensity as function of time and bias voltage (logarithmic scale). (d) shows lifetimes T_1 determined from fits as function of voltage for three different pump laser ($\lambda = 850$ nm) intensities.

6.7 Appendix C: Lifetime measurements

Lifetime measurements were performed in order to investigate to what extent the recorded homogeneous dephasing rates of the QD are lifetime limited or if additional pure dephasing plays a role. The homogeneous dephasing rate is given by: $\gamma_\perp = \gamma_\parallel + \gamma^*$, where $\gamma_\parallel$ is the population relaxation rate, and γ^* is the pure dephasing rate. The homogeneous dephasing time T_2 is related to the population decay time T_1 and the pure dephasing time T_2^* through: $1/T_2 = 1/2T_1 + 1/T_2^*$, where the factor 2 arises because T_1 refers to a population decay rate while T_2 refers to an amplitude decay rate. In the following we present lifetime decay measurements in order to determine T_1.

We switch to the region around where the top metal contact is applied, as here the top DBR is largely etched away and a low Q cavity is present. The sample is excited with a pulsed Ti:sapphire laser (∼80 MHz, $\lambda = 850$ nm). We first record photoluminescence (PL) of an ensemble of QDs shown in Fig. 6.6 (a). The QDs are charge neutral in the voltage range 600-850 mV and become charged for voltages > 850 mV. We then switch to lifetime measurements and detect the PL with an 'ID Quantique ID100-MM50' avalanche photodiode, with a timing jitter of about 100 ps, and analyze this with a 'Becker & Hickl SPC330' time-correlated single photon counter card.

Figure 6.6 (b) shows individual lifetime traces recorded at different voltages. Fits

(red lines) are applied using $y = A\exp(-t/T_1)+B$. Reasonable fits are obtained which could probably be further improved around $t = 0$ ns by taking the response function of the APD into account. In Fig. 6.6 (c) we show a colormap of the PL counts as function of time and voltage, normalized by the number of counts at $t = 0$ ns. In Fig. 6.6 (d) we display the lifetimes T_1 determined from such fits as shown in Fig. 6.6 (b). Small variations in the lifetimes are visible for increasing pump intensities, possibly arising from QD saturation and biexciton decay effects. The maximum lifetime of the QDs is around 750 mV, in the voltage regime where the QDs are charge neutral. For smaller voltages, and thus increasing electric field in the out-of-plane direction, the lifetime decreases as fast non-radiative tunneling processes become more dominant. For larger voltages and decreasing electric field the lifetimes slightly decreases. The electron and holes are now less separated which results in a larger oscillator strength, as this is proportional to the square of the vertical components of the electron and hole wave functions. The lifetime for the charge neutral QDs determined from the fits is approximately $T_1 = 1.7$ ns at 750 mV, and for the singly-charged QDs $T_1 = 1.2$ ns at 900 mV.

For the neutral QD we found from the resonant scanning laser fits $\gamma_\perp = 2.0 \pm 0.5$ ns^{-1}, while a value of $\gamma_\parallel = 1/2T_1 = 0.3$ ns^{-1} would be expected if the line shape were transform limited. This indicates that the pure dephasing rate $\gamma^* \approx 1.7$ ns^{-1}, which could be related to charge or nuclear spin noise, or coupling to phonons. For the single-charged QD $\gamma_\perp = 9.5$ ns^{-1} and $T_1 = 1.2$ ns, which implies that the pure dephasing rate is $\gamma^* \approx 9.1$ ns^{-1}. This indicates that for the trion pure dephasing processes take place that occur much faster compared to the charge neutral QD, and we hypothesize this is related to a co-tunneling mechanism.

Chapter 7

Quantum dot nonlinearity through cavity-enhanced feedback with a charge memory

In an oxide apertured quantum dot (QD) micropillar cavity-QED system, we found strong QD hysteresis effects and lineshape modifications even at very low intensities corresponding to $< 10^{-3}$ intracavity photons. We attribute this to the excitation of charges by the intracavity field; charges that get trapped at the oxide aperture, where they screen the internal electric field and blueshift the QD transition. This in turn strongly modulates light absorption by cavity QED effects, eventually leading to the observed hysteresis and lineshape modifications. The cavity resonance also enables us to observe the QD frequency charge dynamics. All experimental data agrees well with a charging model based on power-law scaling.

M. P. Bakker, T. Ruytenberg, W. Löffler, A. V. Barve, L. A. Coldren, M. P. van Exter, and D. Bouwmeester, submitted to Physical Review B

7.1 Introduction

Cavity quantum electrodynamics with quantum dots (QDs) coupled to microcavities enables various applications such as single-photon switches [133, 141–144], generation of non-classical states of light [26, 145, 146] and hybrid quantum information schemes [13, 112]. However, QDs deviate from an ideal atom-like systems as they strongly interact with their environment, for example through nuclear spins [138, 147] and via charge traps [137, 148]. These interactions need to be understood and controlled in order to improve the QD coherence properties. For this purpose cavities are very useful to probe the QD environment, through increased light-matter interaction.

In this Chapter we investigate such a QD-cavity system. For sufficiently low optical field intensity this system can be described by the QED of an effective 2-level system in a single-mode cavity. For increasing intensities we report on bistable and strong nonlinear behavior. The sample under study consists of InAs self-assembled QDs inside a PIN diode structure embedded in a micropillar. This system combines QD charge and Stark shift control by applying a bias voltage with high-quality polarization-degenerate cavity modes [94, 96, 98–100]. The mode confinement in the transversal direction is achieved by an oxide aperture formed through a wet oxidation

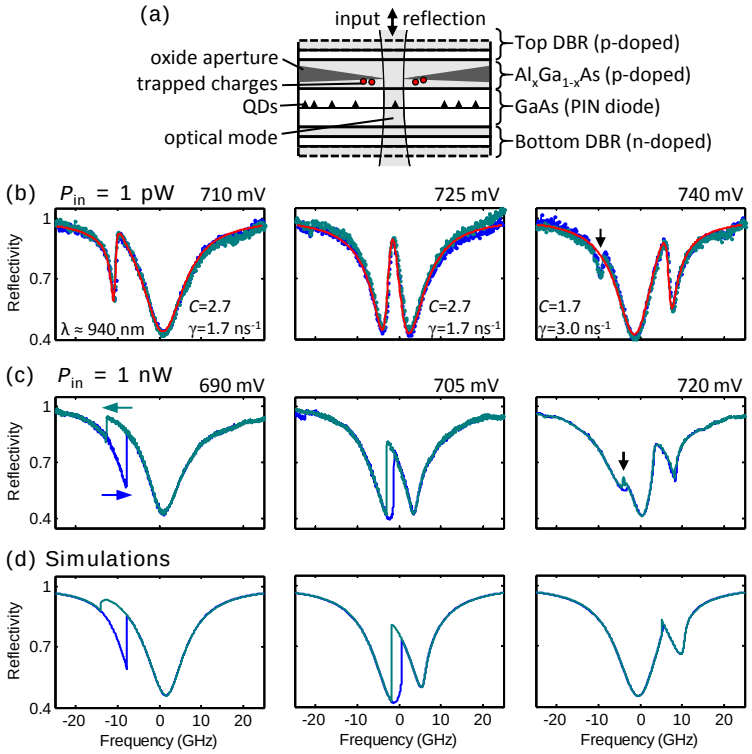

Figure 7.1: (a) Schematic of the sample structure with charges trapped at the oxide aperture. Figure is not to scale and only a couple DBR pairs are shown. Resonant reflection spectroscopy scans recorded using laser intensities of (b) 1pW and (c) 1 nW for various applied bias voltages. Blue (green) curve: upward (downward) frequency scan. Red lines in (b) are fits using Eqn. 7.1 and reflectivity $R = |1 - t|^2$. The QD cooperativity C and dephasing rate γ obtained from the fits are named in the figures. The black arrows denote a second QD in the same cavity. Scans were taken on ∼s timescale. (d) presents simulations that predict the scans in (c).

step. The observed bistability and nonlinear behavior in the cavity QED system can be explained by attributing a second role to the oxide aperture, namely that of a charge memory. Charges in this memory, created by resonant absorption, will cause a modification to the applied bias voltage which in turn shifts the QD frequency, and modify the amount of absorption. In Figure 7.1 (a) the sample structure, with charges trapped at the oxide aperture, is schematically shown.

We consider one of the fine-split transitions of a charge neutral QD coupled to a polarization degenerate cavity mode in the intermediate coupling regime. Figure 7.1 (b) shows reflection spectra, recorded at a sufficiently low incident intensity $P_{in} = 1$ pW such that no nonlinear effects occur. Upward and downward frequency scans overlap perfectly and can be fitted by theory for a dipole inside an optical cavity, which we will discuss later in detail. However, when a higher intensity of 1 nW is used, several strong deviations occur, see Fig. 7.1 (c). First of all, a hysteresis feature appears when the QD is tuned at or below the cavity resonance. Second, while at the high frequency side of the cavity resonance the hysteresis is much less, a line shape modification is still visible. Finally, in order to obtain the same QD detuning compared to the low intensity scans, a lower bias voltage has to be applied. After a thorough characterization of this effect, we present a model that explains all features as is shown in Fig. 7.1 (d).

7.2 One and two laser scans

A first hint on the underlying dynamics is provided by investigating the power dependence in single-laser scans. In Fig. 7.2 (a) we first keep the QD bias voltage constant and show scans for increasing laser intensity. A QD blueshift occurs, as is displayed in Fig. 7.2 (c). In a second set of measurements in Fig. 7.2 (b), we keep the QD-cavity detuning constant by changing the bias voltage as function of the laser intensity. A lower bias voltage has to be applied for increasing laser intensity, shown in Fig. 7.2 (d). Furthermore, the hysteresis width increases with intensity, see Fig. 7.2 (e), up to nearly 6 GHz, but then saturates and even decreases slightly when the intensity is above the QD saturation intensity (~ 2.5 nW). All three observations in Figs. 7.2 (c-e) obey the same empirical power law $\propto P_{in}^{\beta}$, with $\beta = 0.35$. Already at an incident intensity $P_{in} = 11$ pW, corresponding to a maximum mean photon per cavity lifetime of $\langle \overline{n} \rangle \sim 4 \times 10^{-4}$, a QD blueshift and line shape modification is clearly visible. Here the mean intracavity photon number is found from $\langle \overline{n} \rangle = P_{out}/\kappa_m \hbar\omega$, where $\kappa_m \sim 11$ ns^{-1} is the mirror loss rate, ω is the light angular frequency, and the maximum output intensity $P_{out} = |t|^2 P_{in} \sim 1$ pW (see below).

We now switch to a two-laser experiment (see Fig. 7.3) in order to further investigate the phenomenon that the QD blueshifts with increasing laser intensity. The QD transition is probed with a low intensity (1 pW) probe laser such that no line shape modification occurs. We then add a second high intensity (1 nW) pump laser with orthogonal polarization, such that it can be filtered out with a crossed polarizer in the detection channel. The pump laser is scanned in steps across the cavity resonance; for each step the QD-cavity spectrum is measured with the weak probe laser. Figure 7.3 (a-c) presents these measurements for various bias voltages such

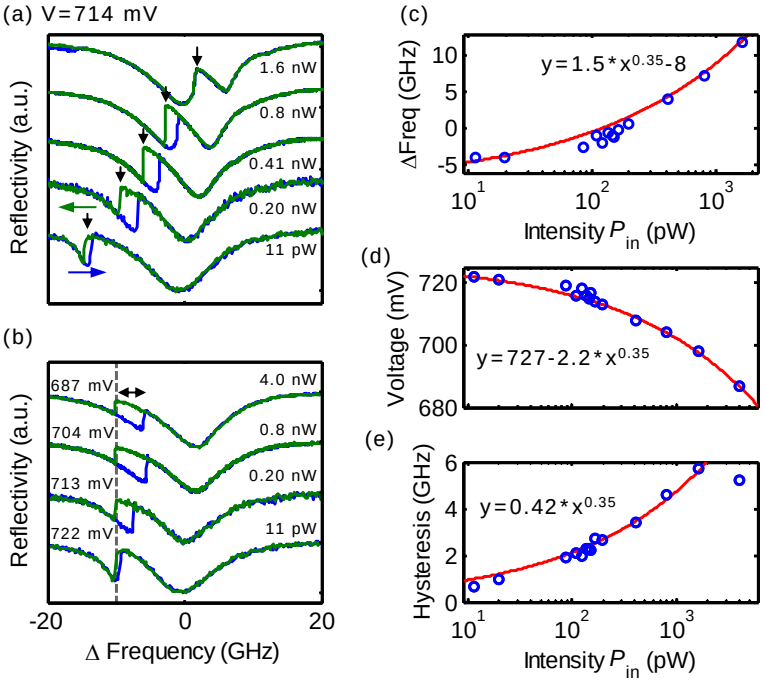

Figure 7.2: Characterization of the QD blueshift and nonlinearity. (a) Resonant reflection spectra for a fixed bias voltage and various intensities of the scanning laser. Blue (green): low to high (high to low) frequency scan. (b) Scans where the QD-cavity detuning is kept constant by varying the bias voltage for various laser intensities. (c) Relative QD shift (estimated from the vertical arrows in (a)), (d) applied bias voltage to keep the QD-cavity detuning constant (vertical dashed line in (b)), and (e) hysteresis width (horizontal arrow in (b)), all as function of the laser intensity. Red lines in (c,d,e) show empirical power law fits. Vertical offsets have been added to the scans in (a,b).

that the average QD-cavity detuning is varied. For every bias voltage the QD-cavity and pump laser-cavity detunings are determined, and the relative QD frequency as function of the pump laser-cavity detuning is shown in Fig. 7.3 (d). The maximum QD blueshift (of about 8 GHz) occurs when the pump laser is resonant with the cavity mode, corresponding to the vertical dashed line. An increased blueshift also occurs when the pump laser is close to the QD frequency, indicated by the arrows in Fig. 7.3 (d), at which point the intracavity field also increases due to cavity QED effects. The gray dashed curves are Lorentzian lines convoluted with the $\propto P_{in}^{0.35}$ power law from Fig. 7.2 (c) and correspond to the data nicely. In conclusion, the data clearly shows that the QD resonance blueshifts when the intracavity field increases, and this effect is independent of the QD-laser or the QD-cavity detuning.

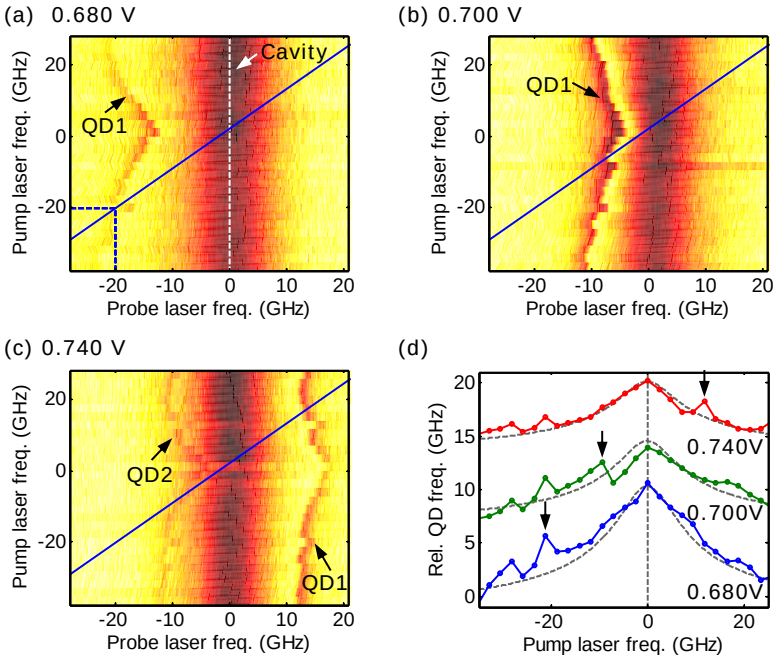

Figure 7.3: Two-laser scans with resonant lasers. (a-c) Reflectivity color maps as function of the weak (1 pW) probe laser frequency and the second high intensity (1 nW) pump laser frequency for various applied bias voltages. The blue line shows the pump laser frequency compared to the probe laser. The arrows indicate the QD position. (d) Relative QD frequency shift as function of the pump laser-cavity detuning. The arrows denote where the laser is resonant with the QD. Gray dashed lines: Lorentzian function convoluted with the power law from Fig. 7.2 (c) that have been added as a reference. Vertical offsets are added to the curves.

7.3 Model and explanation

We now introduce a model that explains the dynamic line shape modifications. We start from the transmission amplitude of a cavity with a coupled dipole [37, 139]:

$$t = \eta_{out} \frac{1}{1 - i\Delta + \frac{2C}{1 - i\Delta'}}, \tag{7.1}$$

where $\Delta = 2(\omega - \omega_c)/\kappa$ is the relative detuning between the laser (ω) and cavity (ω_c) angular frequencies, C is the device cooperativity, $\Delta' = (\omega - \omega_{QD})/\gamma$ is the relative detuning between the laser and QD transition (ω_{QD}), η_{out} is the output coupling efficiency, κ is the total intensity damping rate of the cavity and γ is the QD dephasing rate. We obtain close to perfect mode-matching, and therefore the total transmittivity through the cavity is given by $T = |t|^2$, and the total reflectivity is given by $R = |1 - t|^2$. In Fig. 7.1 (a) we show that the model fits the low intensity

measurements very well. The QD cooperativity and dephasing parameters C and γ are noted in the subfigure windows, and a cavity damping rate $\kappa \sim 77$ ns^{-1} and an output coupling efficiency $\eta_{out} = 2\kappa_m/\kappa \sim 0.3$ is found, corresponding to a cavity Q-factor of $Q \sim 2.6 \times 10^4$.

As a next step, we introduce a QD frequency $f_{QD} = \omega_{QD}/2\pi$ that dynamically changes with the intracavity intensity, which is proportional to $|t|^2$:

$$f_{QD} = f_0 + \alpha|t|^{2\beta}, \tag{7.2}$$

where f_0 equals the QD frequency in the limit of vanishing intracavity intensity. Based on the empirical values determined in Fig. 7.2 (c), we use $\alpha = 1.5 \times (P_{in}/\eta_{out}^2)^{\beta}$ GHz, with P_{in} in pW, and $\beta = 0.35$. Due to cavity QED effects, the intracavity field depends strongly on the QD frequency such that the cavity can change from being largely transparent to being largely reflective through only small changes in the QD frequency. This interplay leads to the observed nonlinear behaviour.

Finally, we take into account that we are operating the QD–cavity system close to the saturation intensity, which slightly suppresses the QD features. We take this into account by calculating the reflectivity R' by taking the weighted sum of the reflectivities of a coupled (R) and uncoupled (R_0) cavity: $R' = xR + (1-x)R_0$, with $x = 0.8$. This is a strong simplification of a more rigorous approach based on the quantum master equation and calculation of the intracavity photon number [133], but is sufficient for our purpose. For QD cooperativity C and dephasing rate γ we use the values obtained in the fits in Fig. 7.1 (a). Figure 7.1 (c) shows that the predicted scans match the actual measurements very well.

As the underlying physical mechanism we hypothesize that charges are excited by the resonant laser and get trapped at the oxide aperture. Reasonably high doping concentrations were used, up to 6×10^{18} cm^{-3} for the carbon p-doped layers and up to 5×10^{18} cm^{-3} for the silicon n-doped layers, and it is well-known that absorption takes place in these doped layers [149], resulting in a non-neglible photocurrent (see the Appendix section I). The excited charges partly screen the internal electric field responsible for the quantum confined stark effect in the QD, leading to the observed blueshift of the QD transitions.

Furthermore, the fact that even for a very low cavity mean photon number of ~ 0.001 ($P_{in} = 11$ pW) nonlinearities take place, indicates that the oxide aperture must form an efficient charge memory compared to the QD-cavity decay rate (77 ns^{-1}). It is well known that the interface between GaAs and aluminum oxide (AlO_x), produced by wet oxidation of AlAs, provides a very high density of charge traps, in the form of amorphous oxide and micro crystallites [150], and in the form of elemental interfacial As [151], leading to spatially non-uniform Fermi level pinning [152]. The time-resolved charge decay measurements presented below confirm that the charges are relatively long-lived on a ~ 10 ms timescale. Also, a comparison with QDs observed outside of the oxide aperture region show that laser induced blueshift is neglible in these regions (see Appendix section II). Furthermore, the charging hypothesis agrees with the observed $\propto P^{0.35}$ sublinear powerlaw, which would be the consequence of Coulomb repulsion between trapped charges, possibly in combination with increased filling of trap states that have an increasing decay rate.

Our results agree with observations in Ref. [137], where single–charge fluctuations are probed at a GaAs/AlAs interface located about 50 nm away from the QDs, while a gradual variation was observed for charge traps more than 150 nm away. We did not observe any single–charge influences as the distance between the QDs and the oxide aperture is about 200 nm in our sample. In contrast to our work, the GaAs/AlAs interface studied in Ref. [137] is located in the intrinsic region, while the aperture in our sample is located in the p-doped region, but a similar QD blueshift for increasing laser intensity and constant bias voltage was observed.

7.4 Off-resonant laser pumping and time dynamics

Finally, we performed a set of measurements to gain insight in the temporal dynamics of the charge build-up and decay. For this purpose we use a laser ($\lambda = 852$ nm) that is off-resonant with the cavity but is resonant with the wetting layer. At a larger laser intensity, more charges are excited compared to the resonant laser and larger QD shifts can be obtained. We now use the coupled QD-cavity system as a very sensitive probe of the internal electric field, a principle that was also used to monitor a single charge trap in real-time [153].

Figure 7.4 (a) shows, for various off-resonant pump laser intensities, the bias voltage that has to be applied to tune the QD to the cavity resonance, determined by using a weak ($\sim$1 pW) resonant probe laser. Again, as in Fig. 7.2 (d), a clear sub-linear behavior $\propto P_{in}^{\beta}$ is visible. At an even higher intensity of 100 μW, a bias voltage of 350 mV had to be applied to tune the QD in to resonance, clearly indicating that the charge buildup and QD blueshift is not easily saturated. Strikingly, even for an excitation power of 200 nW, the QD has the same cooperativity C and dephasing rate γ as when no off-resonant laser is present, see Fig. 7.4 (b). This indicates that, even though many charges are excited, they are located relatively far away and give rise to a more-or-less constant effective electric field, thereby preserving the QD coherence.

In order to directly monitor the time dynamics of the charge buildup and decay, we fix a weak probe laser that will not excite any additional charges at the cavity resonance, and monitor the reflectivity as function of bias voltage and time. Figure 7.4 (c) shows, for various off-resonant pump laser intensities, reflectivity colormaps of the probe laser when the off-resonant pump laser is turned on at $t = 0$ ms. For $t < 0$ ms, the QD is resonant with the cavity resonance at $V = 713$ mV (white dashed lines), corresponding with a high probe laser reflectivity at this voltage and a low reflectivity at different voltages. The reflectivity at $V = 713$ mV abruptly decreases as the pump laser is turned on, but is then restored at lower bias voltages, demonstating direct probing of the charge build-up. For increasing pump laser intensities, the reflectivity is restored at a lower voltage, but also the time for the charge build-up to reach an equilibrium decreases.

The decay of the charges is monitored in Fig. 7.4 (d), where the pump laser is turned off at $t = 0$ ms. For $t < 0$ ms the QD reflectivity signal is now highest for a low bias voltage when the charge reservoir is saturated. After the pump is turned off and the charges disappear, the reflectivity now gets restored at an increasing bias voltage. The charge decay rate is initially fastest, when many charges are still present and the

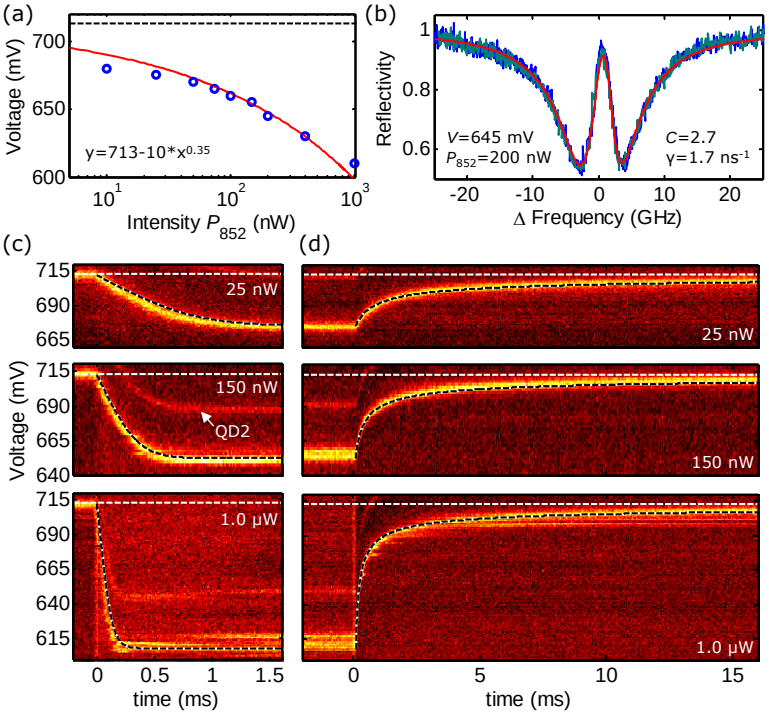

Figure 7.4: Two-laser scans with an off-resonant ($\lambda = 852$ nm) laser. (a) shows the bias voltage where the QD transition is resonant with the cavity mode, as function of the intensity P_{852} of the off-resonant laser. The black dashed line indicates the QD bias voltage when no off-resonant laser is applied. (b) Example of resonant reflection scans using a weak (1 pW) probe laser, recorded in the presence of an off-resonant laser. Text in the figures denotes the applied bias voltage V, intensity P_{852}, and QD cooperativity C and dephasing rate γ of the predicted red line. (c,d) Colormaps of the reflected intensity of the probe laser fixed to the center of the cavity resonance (light/dark: high/low signal, corresponding to an on(off) resonant QD), as function of the time and applied bias voltage, for various off-resonant pump intensities. The off-resonant laser is turned on (c) and off (d) at $t = 0$ ms. The red line in (a) and the black-white dashed in (c,d) are reproduced using the same parameters (see main text for explanation). Note that the time axes of (c,d) are different.

QD is resonant at a lower bias voltage, but then strongly decreases and finally occurs on a ∼10 ms timescale, much slower than the charge build-up rate.

We now introduce a simple power law model to describe the charge build-up and decay dynamics. We assume that the QD voltage shift ΔV is proportional to the number of trapped charges Q, and increases as a function of the pump laser intensity P, such that $\Delta V = -Q = -\Gamma P^{\beta}$. As a result, the charge decay and buildup is described using: $\frac{dQ}{dt} = P - (Q/\Gamma)^{1/\beta}$. The red line in Fig. 7.4 (b) and the white-black dashed lines Fig. 7.4 (c-d) are reproduced with $\Gamma = 10$ and the same powerlaw scaling factor $\beta = 0.35$ as found earlier, and describe the data nicely.

Our results could serve as a novel method to tune QD transitions without the need for electrical contacts, or enable independent tuning of QDs sharing the same voltage contacts. Furthermore it could serve as a low power optical switch mediated by a charge memory. The cavity-enhanced feedback mechanism with the charge environment could in principle also occur in other solid-state microcavity structures, where doped layers are present in which charges can be excited and where material defects or interfaces could act as a charge trap. This interaction therefore also has to be taken into account when studying dynamical nuclear spin polarization (DNP) effects, which is of general interest to prolong the QD coherence time and the potential to form a quantum memory. DNP gives rise to QD line shape modifications, hysteresis and bistability behavior [138, 154–159]; phenomena that could also give rise to cavity-enhanced feedback mechanisms.

7.5 Conclusion

In conclusion, we have studied a neutral QD transition coupled to a microcavity and observed strong cavity-enhanced feedback with the charge environment. Hysteresis and modifications of the QD line shape are demonstrated at intensities of way less than 1 photon per cavity lifetime, which we explain and model by a QD frequency blueshift attributed to charges trapped at the oxide aperture as a function of the intracavity field. In general, these results demonstrate the potential of studying and controlling the QD environment using a cavity QED system.

Appendix

In these Appendices we will first present photocurrent measurements. To confirm that a $\lambda \sim 940$ nm resonant laser excites charges in the cavity region, we compare the photocurrent with when a $\lambda = 852$ nm off-resonant laser is used. Then we compare photoluminescence data with and without the presence of an aperture, to demonstrate that the oxide aperture plays an important role in trapping the charges,. These observations support our claim that the mechanism behind the observed nonlinear effects in the resonant QD scans, is the excitation of charges that are trapped by the oxide aperture.

7.6 Appendix A: Photocurrent measurements

Current as function of bias voltage was measured without (dark) and with the presence of a $\lambda = 852$ nm or a $\lambda \sim 940$ nm laser, see Fig. 7.5 (a). The $\lambda \sim 940$ nm laser

frequency was locked at the cavity resonance, such that the absorption is increased due to the high finesse ($\sim 2\times10^3$) of the cavity, as is the case during the resonant scans in the main text. When no additional pump laser is applied, a current flows through the device in the same direction as that the forward bias voltage is applied, giving rise to an IV-curve that is typical for a PIN diode device. In the presence of an additional pump laser charges are now optically excited and flow in the opposite direction due to the internal field being present, giving rise to an additional negative photocurrent. In Fig. 7.5 (b) we compare the absolute value of the photocurrent produced by the $\lambda \sim 940$ nm and $\lambda = 852$ nm laser, normalized by the pump laser intensity. For both lasers a strong bias voltage dependency is visible and the collected photocurrent is smaller at a larger bias voltage, which is closer to the flatband regime. This indicates that either the absorption, or the collection efficiency of the excited charges, is voltage dependent. The 940 nm laser gives rise to a photocurrent of about 0.5 mA/W at a bias voltage of 700 mV where charge neutral QDs are typically operated, which at an intensity of 1 nW corresponds to about 3×10^6 charges being excited and collected per second.

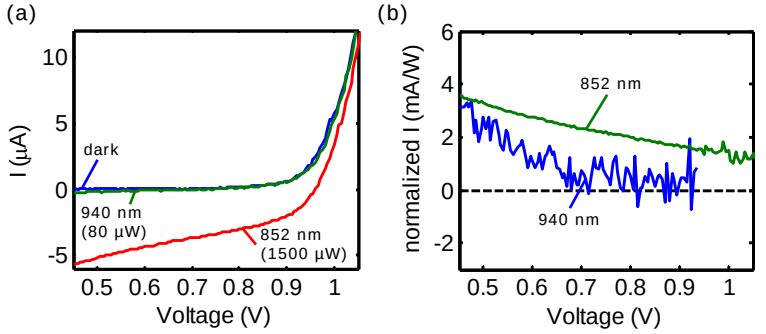

Figure 7.5: (a) The current through the sample as function of the applied bias voltage without (dark) and with the presence of a 852 nm or $\sim$ 940 nm laser. The 940 nm laser was locked at the microcavity resonance. The used intensity is mentioned between brackets.(b) Difference between the current when no laser and when an 852 nm or 940 nm laser is present, normalized by the input laser intensity.

7.7 Appendix B: Photoluminescence measurements

Next, we compare the photoluminescence collected from the oxide-aperture microcavity and from a region with an unbalanced cavity. In the unbalanced cavity region the top DBR has been nearly completely etched away, in order to enhance the collection efficiency, and no oxide aperture has been applied. Figure 7.6 (a,c) present colormaps of the PL spectra as a function of applied bias voltage and collected wavelength, using a $\lambda = 852$ nm pump laser of various intensities. Figure 7.6 (b) shows the PL intensity as function of voltage at the cavity resonance. Single QD lines (marked by the arrows) are hardly distinguishable from the background cavity emission, which

originates from broadband wetting layer emission. For increasing pump laser intensity, it is clearly visible that the QD lines appear at a lower bias voltage. For the QDs in the region without an oxide aperture, the shift in voltage is however much smaller. The QDs in Fig. 7.6 (c) are now better visible, even though at high pump laser intensities for increasing voltage again broadband emission 'washes out' clear QD signatures. Figure 7.6 (d) presents the mean PL counts for various pump intensities. A shoulder is visible, which corresponds with the voltage range where the QDs are on average charge neutral. The shoulder does shift to a lower voltage range, but the shift (in total $\sim$ 50 mV for 1100 μW) is much smaller compared to the total $\sim$ 700 mV (for 1500 μW) voltage shift of the QDs in the microcavity. Even though it is likely that roughly the same amount of charges are excited by the $\lambda = 852$ nm laser in the microcavity region compared to elsewhere in the sample, these results indicate that the oxide aperture provides a charge memory, causing a much larger effective charge buildup resulting in a larger voltage shift of the QDs.

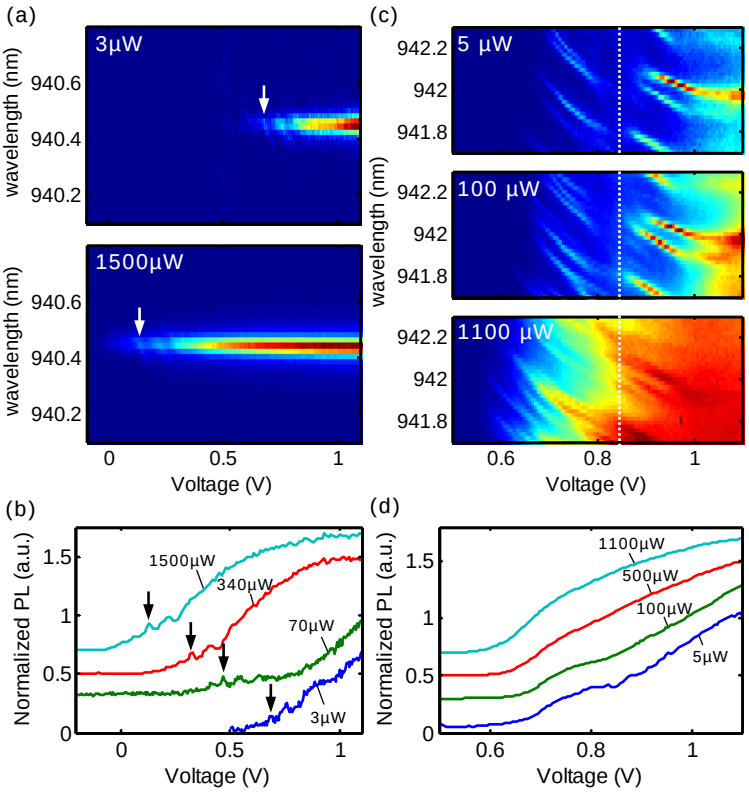

Figure 7.6: Photoluminescence (PL) colormaps as function of the applied bias voltage and collection wavelength recorded at (a) the microcavity, and (c) from an unbalanced planar cavity. The intensity of the ($\lambda = 852$ nm) pump laser is indicated in the top left corner of the figures. (b) PL intensity as function of bias voltage at the cavity resonance, for various pump laser intensities. The vertical arrows in (a, b) denotes the same QD peak. (d) average PL intensity as function of voltage collected from the unbalanced planar cavity. The white dashed vertical line serves as a reference. An offset has been added between the curves in (b, d).

Chapter 8

Homodyne detection of coherence and phase shift of a quantum dot in a cavity

A homodyne measurement technique is demonstrated that enables direct observation of the coherence and phase of light that passed through a coupled quantum dot (QD)–microcavity system, which in turn enables clear identification of coherent and incoherent QD transitions. As an example, we study the effect of power induced decoherence, where the QD transition saturates and incoherent emission from the excited state dominates at higher power. Further, we show that the same technique allows measurement of the quantum phase shift induced by a single QD in the cavity, which is strongly enhanced by cavity quantum electrodynamics effects.

M. P. Bakker, H. Snijders, W. Löffler, A. V. Barve, L. A. Coldren, D. Bouwmeester, M. P. van Exter, submitted to Optics Letters

8.1 Introduction

Quantum dots (QD) are artificial atoms in the solid–state with potential applications for quantum information [71]. Embedding QDs in high Q microcavities holds promise to implement deterministic logic gates [112], entangle independent photons [160], and couple distant QDs to form a quantum network [13]. Additionally, cavity-enhanced light–matter interactions enable a powerful spectroscopic tool for QD characterization. In the following, we present a straightforward technique to analyze both the coherence as well as the quantum phase shift of light transmitted through a QD–cavity system.

Several techniques have been demonstrated to determine the coherence of the emission of a coherently driven two-level transition in an atomic or molecular system, i.e. resonance fluorescence (RF). These techniques include analyzing the interference between RF and the incident laser itself as function of polarization, analyzing the time correlation function $g^{(2)}(\mathrm{t})$ using a Hanbury Brown Twiss setup, measuring with an interferometer the mutual phase coherence between the coherently scattered light and a local oscillator, or analyze the frequency spectrum using a high finesse scanning Fabry Perot interferometer [161–164]. Additionally, the phase shift of transmitted light through a cavity with a strongly coupled atom can be determined using a heterodyne setup [56].

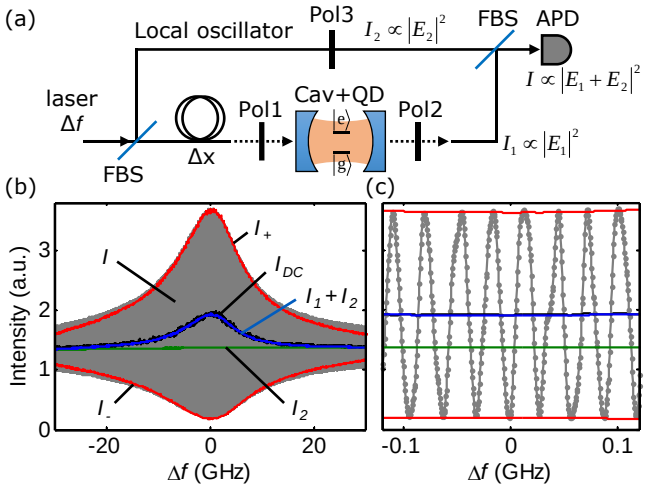

Figure 8.1: Demonstration of the homodyne interference technique. (a) Schematic of the setup. Coherent light from a scanning laser is split using a fiber beam-splitter (FBS), transmitted through the QD-cavity system, recombined with the local oscillator on a FBS and recorded with a avalanche photodiode (APD). Pol: polarization controlling optics. Pol3 is always set to match Pol2. (b) Signal for an empty cavity as function of scanning laser frequency detuning. Grey: interference signal I when combing the local oscillator and the cavity signal. Black: DC component. Green: I_2 reference signal. Blue: predicted DC signal from the sum $I_1 + I_2$. Red: predicted envelope of the interference signal for full interference (see text for details). (c) zoom-in around zero detuning.

Recently, such techniques have been extended to also study QDs in solid-state systems [165–168] and to measure the quantum phase shift induced by a coupled QD-cavity system by analyzing the reflection intensity as function of output polarization [145], or by interfering light reflected from the QD-cavity system with light reflected from another piece of the sample [169]. In this Letter we present a homodyne detection technique that enables simultaneous measurement of both coherence and induced phase shift. The technique is relatively straightforward as it requires only one scanning laser and it is mostly fiber-based. It provides complete coherence and phase information as function of scanning laser detuning.

8.2 Setup and technique

The setup for the homodyne interference technique is schematically displayed in Fig. 8.1 (a). Light from a scanning laser is first split into two paths with a fiber beam splitter (FBS). One path (with intensity $I_1 \propto |E_1|^2$) is transmitted through the QD–cavity system, while the other path ($I_2 \propto |E_2|^2$) is used as the local oscillator. The two signals are combined using a FBS and the interference signal ($I \propto |E_1 + E_2|^2$) is recorded. The sample under study is an oxide apertured micropillar with embedded InAs self-assembled QDs, a system that combines QD charge and energy

control, access to the intermediate coupling regime, and polarization degenerate cavity modes [94, 96, 98–100, 170]. Access to the full polarization degree of freedom enables us to use free space polarizing optics (Pol1 and Pol2) to set the input and output polarizations. These are either set to be parallel, or the output is set at orthogonal crossed polarization; we use a combination of a quarter wave plate and a polarizer to compensate for the small amount of birefringence present in the sample. To match the local oscillator polarization (Pol3) to the output polarization (Pol2), we use a coiled fiber polarization controller. In our setup there is no need for active stabilization and a single scan is recorded in typically a couple of seconds.

The signal after transmission through the sample is given by $E_1(t) = E_1 \exp\big(i\omega t + i2\pi\frac{\Delta x}{c}\Delta f + i\phi(f,t)\big)$, where ω is the angular frequency, Δf is the laser frequency detuning, $\Delta x \approx 10$ m is the optical path length difference between the two interferometer arms, c is the speed of light, $\phi(\Delta f, t)$ is the phase shift induced by the QD–cavity system, and E_1 is the transmission amplitude of the cavity. When this signal is combined with the local oscillator $E_2(t) = E_2 e^{i\omega t}$, the resulting interference intensity I is given by:

$$I = I_1 + I_2 + 2\sqrt{I_1 I_2}\cos\left(2\pi\frac{\Delta x}{c}\Delta f + \phi(f,t)\right). \tag{8.1}$$

When the transmitted light is coherent, i.e. $\phi(\Delta f, t) = \phi(\Delta f)$ does not vary in time, I contains interference oscillations that are bounded by $I_\pm = I_1 + I_2 \pm 2\sqrt{I_1 I_2}$. In case of incoherent light, which can be interpreted as a rapidly varying phase $\phi(\Delta f, t)$, no interference is present and $I = I_1 + I_2$.

In Figure 8.1 (b,c) we show the case for an empty cavity, where the transmitted light naturally remains fully coherent. Also the polarization is not modified, and we set Pol2 parallel to Pol1 and use a large intensity $\sim 10\ \mu$W that is recorded with a fast photodiode instead of an APD. First, we record the reference signal I_2 (green curve) and the transmitted intensity I_1 (not shown) separately; this enables us to predict the DC signal $I_1 + I_2$ (blue curve) and the interference envelope $I_\pm = I_1 + I_2 \pm 2\sqrt{I_1 I_2}$ (two red curves). The grey curve shows the measured interference signal I. By low pass filtering we obtain the DC signal I_{DC} (black curve) that agrees well with $I_1 + I_2$. The envelope of I agrees nicely to the independently measured calculated envelopes (red curves), which is especially clear in the zoom-in around the cavity resonance in Fig. 8.1 (c). It is worth pointing out that, even though $I_1/I_2 \simeq 0.3$, the ratio of the maxima and minima of the interference fringes is much larger: $I_+/I_- \simeq 12$. This demonstrates the beauty of interference and the strength of the technique to measure the coherence of the transmitted light.

8.3 Charge neutral QD and power dependence

We now investigate the coherence properties of light scattered by a charge neutral QD. The lowest excited states of a neutral QD are split in energy, due to electron-hole interaction arising from QD anisotropy, and couple through orthogonally linear polarized transitions with the ground state in a V-type system as is shown in the inset in Fig. 8.2 (a). We prepare the input polarization at 45° with respect to the

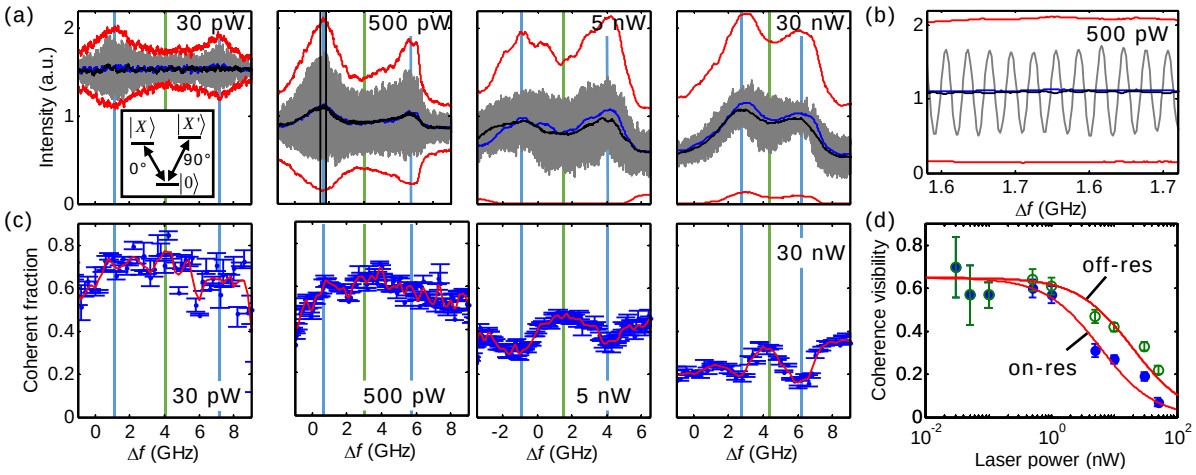

Figure 8.2: Coherence of the scattered light by a QD as function of laser cavity detuning and injected power. (a) Scans for various laser powers. The input polarization was set to 45° and transmission was recorded through a crossed polarizer such that only the two fine-split QD transitions, see inset for a schematic, and not the cavity are visible. The five curves show: I (grey), I_{DC} (black), $I_1 + I_2$ (blue), I_+ and I_- (red 2×). (b) zoom-in of the 500 pW scan in (a). (c) Coherent fraction determined as the ratio $F = (I_{max} - I_{min})/(I_+ - I_-)$. (d) Coherent fraction as function of laser power determined on the resonance of a QD transition (blue vertical lines in (a,c)) and off resonance (green vertical lines). Red lines are predicted curves using Eq. (8.2).

polarizations of both transitions such that scattered light, with a polarization of 0° or 90 °, passes through the crossed polarizer set to -45°; while the cavity background transmission, of which the polarization is unchanged, is filtered out.

Figure 8.2 (a) shows the light scattered by the two transitions for various intensities. First I_1 and I_2 are recorded separately and $I_1 + I_2$ (blue lines) and the envelope I_+ and I_- (two red lines) are calculated. The interference signal I is shown in grey and the low pass filtered signal I_{DC} is shown by the black line, which follows the blue line. The interference signal I was Fourier-filtered with a bandpass filter centered at the oscillation frequency to remove some noise. Figure 8.2 (b) shows a zoom-in of the 500 pW scan around the low frequency transition. A clear oscillation signal is visible, with a coherent fraction, defined as the ratio $F = (I_{max} - I_{min})/(I_+ - I_-)$, where I_{max} and I_{min} are the upper and lower bounds of the interference envelope, of about 0.6. This indicates that the scattered light is only partially coherent.

To investigate this further, we show in Fig. 8.2 (c) the calculated coherent fraction as function of the laser detuning for various intensities. For a low power of 30 pW it can be seen that the scattered light coherence is about 0.7, but this decreases for increasing intensities. An additional structure of dips in the curve of the coherent fraction becomes visible. This shows that the coherence decreases more rapidly at the QD resonances (marked by the blue vertical lines), compared to the detuned case (the green vertical line marks the center between the two transitions) due to the less efficient off-resonant driving. We note that for increasing power the QD line shapes become distorted and the fine splitting between transitions becomes smaller, due to a dynamical charging effect as is explained in Ref. [171].

To analyze this power-dependency, we plot in Figure 8.2 (d) the coherent fraction at the resonance and off the resonance of a QD transition as function of the laser power. The fraction F of the scattered light that remains coherent follows the relationship [172]:

$$F = \frac{\gamma_{\parallel}/\gamma_{\perp}}{1 + (P/P_o)/(1 + \Delta'^2)}, \tag{8.2}$$

where $\gamma_{\parallel}$ and $\gamma_{\perp}$ denote the population relaxation rate and the homogeneous dephasing rate, respectively, P is the laser power, P_0 is the saturation power, and Δ' is the detuning with respect to the QD linewidth. The scattered light is almost fully coherent if the used power is small and $\gamma_{\parallel} \approx \gamma_{\perp}$, i.e. the pure dephasing is small. For increasing power the coherent fraction decreases as the QD excited state population builds up and incoherent emission increases. For frequencies detuned from the QD resonance the effective driving rate becomes smaller and the effects gets reduced. We show theoretical curves for $\gamma_{\parallel}/\gamma_{\perp} = 0.65$, $P_0 = 6$ nW, and $\Delta' = 0$ and $\Delta' = 1.5$ for the on-resonance and off-resonance cases, which match the data well and demonstrate the nonlinear QD saturation dynamics. The mean intracavity photon number $\langle \overline{n} \rangle$ is given by: $\langle \overline{n} \rangle = P_{out}/\kappa_m \hbar\omega$, where $\kappa_m \approx 11$ ns^{-1} is the mirror loss rate, and the maximum output intensity $P_{out} = |t|^2 P$ is a function of the maximum transmittivity $|t|^2 \approx 0.09$ and incident power P. A saturation power of $P_0 = 6$ nW corresponds to a mean intracavity photon number $\langle \overline{n} \rangle \approx 0.2$, and sounds reasonable compared to other work with efficient coupling to a single emitter [164]. The direct observation

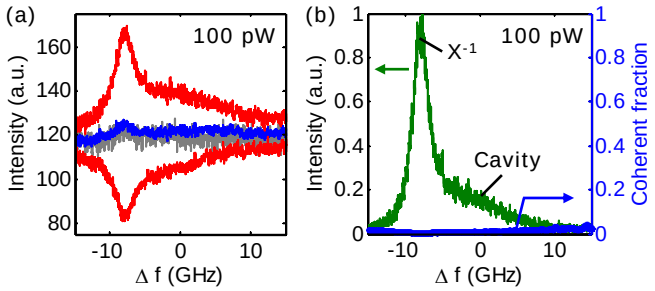

Figure 8.3: Incoherent scattered light from a singly-charged QD (X^{1-}) that suffers from fast decoherence. A linear input and a crossed output polarization is used such that only light scattered by the circularly polarized QD transitions is detected. (a) shows the interference signal I (grey), $I_1 + I_2$ (blue), and I_+ and I_- (red lines). (b) cross-polarized transmitted intensity I_1 of the QD-cavity system (green) and the determined coherence visibility (blue), showing that the scattered is nearly fully incoherent ($F < 0.05$).

that $\gamma_\parallel/\gamma_\perp = 0.65$ indicates that the QD lineshape is not lifetime limited and that additional pure dephasing, such as spectral fluctuations or coupling to phonons, plays a role.

8.4 Singly-charged QD

We now turn in Fig. 8.3 to a negatively charged QD that suffers from decoherence. We use a linear input polarization such that only the light scattered by the circularly polarized QD transitions passes through the crossed output polarizer. In Fig. 8.3 (a) we show $I_1 + I_2$ (blue line) and the predicted envelope I_+ and I_- (red lines). The interference signal I (grey line) now hardly shows oscillations. The calculated coherent fraction, shown by the blue curve in Figure 8.3 (b), is less than 5%. This implies that $\gamma_\parallel/\gamma_\perp \ll 1$ and that the QD suffers from fast decoherence. The green curve in Fig. 8.3 (b) displays the transmitted intensity I_1; showing the red detuned QD, and part of the cavity line shape due to the dispersive effect of the QD coupled to it.

The strong incoherent behavior was previously also investigated through high resolution spectral and polarization resolved studies in Ref. [170]. Here among others a larger homogeneous dephasing rate $\gamma_\perp$ and smaller cooperativity C were observed for the charged QDs compared to the charge neutral ones. The findings are attributed to a fast co-tunneling process of electrons across the very small (20 nm) tunnel barrier that separates the QD from a n-doped contact region. Our technique therefore serves as a powerful QD characterization technique which will help to characterize future sample improvements, such as utilizing a thicker tunnel barrier.

8.5 Phase shift

Finally, we show that from the obtained data we can also derive the quantum phase shift induced by a single QD transition coupled to a cavity, which forms a hallmark in cavity QED experiments [56, 145, 169, 173]. This phase shift $\phi(\Delta f)$,

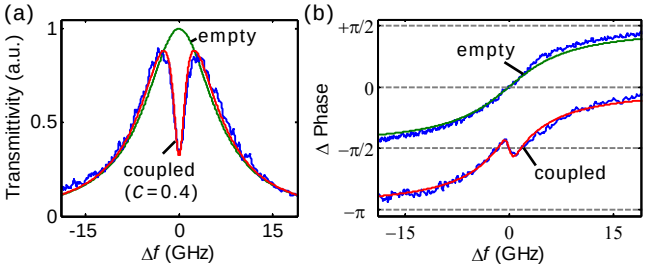

Figure 8.4: Phase shift induced by a QD–cavity system. (a) shows the transmitted intensity I_1 of a coupled QD–cavity system recorded at $P_{laser} = 10$ pW. (b) shows the phase shift for an empty cavity for $P_{laser} = 10$ μW (upper curve) and a coupled system for $P_{laser} = 10$ pW (lower curve). The lower curve is displaced for clarity. Red lines in (a,b) are predicted curves for QD cooperativity $C = 0.4$, QD depasing rate $\gamma_\perp = 4$ ns^{-1} and cavity total loss rate $\kappa = 80$ ns^{-1}. Green curves in (a,b) are predicted lines for an empty cavity.

see Eq. (8.1), can easily be extracted from the interference signal by analyzing the oscillation in a rotating frame, which we realize in practice by multiplying the signal with a complex exponent $\exp\left(i2\pi\frac{\Delta x}{c}\Delta f\right)$ and applying a DC filter. We switch back to a neutral QD and set the input polarization to match one of the fine split transitions and now record the transmission with a parallel polarization. In Fig. 8.4 (a) we display the transmitted intensity I_1, showing the QD feature appearing as a dip in the otherwise Lorentzian cavity lineshape. Figure 8.4 (b) shows the phase shift induced by an empty cavity and by a coupled QD–cavity system. The red and green curves are calculated based on a cavity QED model with no additional fit parameters [37, 139, 170], and agree nicely to the data.

8.6 Conclusion

In conclusion, we have presented a technique that enables to determine the coherence and phase of light that is transmitted through a coupled QD-cavity system. The method is versatile as it only requires one scanning laser and is mostly fiber-based. This technique is important for QD characterization studies and for fundamental tests of cavity QED.

Chapter 9

Outlook

In this chapter we start with a discussion on 3 ongoing studies, which are not yet ready for publication in a scientific journal but are still important preliminary results and offer food for thought and discussion: (i) First, we will present photon time correlation measurements that were performed by resonantly probing a coupled QD–cavity system. Clear signatures of bunching and anti-bunching are demonstrated. (ii) Next, we will propose a method to study phonon induced exciton dephasing via an asymmetry in the QD dephasing rate between red and blue cavity detunings in our current cavity QED sample. The challenge lies in distinguishing between these phonon influences and other (voltage dependent) dephasing effects. (iii) Finally, we propose a method to increase the fidelity of quantum operations by using the full polarization degree of freedom in a polarization degenerate microcavity. By tuning the input and output polarizations and using interference of orthogonal light components, the contrast between a coupled and uncoupled QD–cavity system can be dramatically enhanced.

We conclude with a discussion on some of the drawbacks of our current sample ('131018A') that were discovered during the work in this thesis, and discuss improvements for new sample generations.

9.1 Photon correlation measurements

A cavity QED system that is resonantly probed can convert coherent laser light into non-classical states of light that follows super-Poissonian statistics (bunched photons) or sub-Poissonian statistics (anti-bunched photons). This property could be used to implement a single-photon switch [141], towards which much experimental progress has been realized [63, 142–144, 174, 175]. Also, photon correlation measurements could offer a technique to observe Jaynes-Cummings (JC) nonlinearities and transitions to higher order rungs of the JC ladder [176, 177]; nonlinearities that could be used to generate N–photon bundles [26, 178], where the photons released by the cavity system exist in well defined Fock states.

For the photon correlation measurements, the scanning laser is first tuned to the cavity resonance frequency and locked to a resonance of the 250 MHz free spectral range Fabry-Perot interferometer. The reflected and transmitted light is collected with a single-mode and multi-mode fiber, respectively, and is then detected with 'ID Quantique ID100-MM50' avalanche photodetectors (APD). Alternatively, we have performed a classical photon correlation measurement by using a fiber beam splitter (FBS) in reflection or transmission. The APDs have a timing jitter of about 100 ps,

but relatively small detection efficiencies of only $\sim 3\%$ at a wavelength of 940 nm. The signal from the two APDs is then analyzed using a 'Becker & Hickl SPC330' time-correlated single photon counter card. A neutral QD with a large cooperativity $C \approx 2.5$ was used in a polarization degenerate microcavity, the same QD–cavity system presented in Chapters 6 and 7. Typically light intensities of 1-10 pW were used to probe the QD-cavity system.

In Fig 9.1 we present preliminary results of photon correlation measurements. In Fig. 9.1 (a), signatures of the anti-bunching of light are shown, with $g^2(\Delta t = 0) \approx 0.5$. The input linear polarization was set to 45° with respect to the two fine split QD transitions and crossed polarizers were used to detect the reflected and transmitted light. A clear dip of coincidence events around $\Delta t = 0$ ns is visible.

On the other hand, we present a clear bunching feature in Fig. 9.1 (b), with $g^{(2)}(\Delta t = 0) \approx 2.4$. The polarization was set to match one of the fine split transitions, and the transmitted light was analyzed at the same polarization with a FBS. The bunching and anti-bunching signatures approximately correspond to Lorentzian functions (red curves) with a FWHM of 360 ps, which is approximately the convoluted timing resolution of two detectors. This indicates that the interaction of light and the coupled QD–cavity system occurs on a very fast timescale, probably on the order of the intra-cavity photon storage time $\tau \approx 1/2\kappa_m \approx 45$ ps.

To intuitively understand the photon correlation measurements, one could assume that if a n-photon Fock state interacts with the coupled QD–cavity system, one photon will have the transmittivity T_1 and reflectivity R_1 that corresponds to the coupled QD–cavity system (with cooperativity C), while the other $n-1$ photons will have transmittivity T_c and reflectivity R_c that corresponds to an empty system ($C = 0$). Photon anti-bunching then occurs in the general case when $T_1, R_1 > 0$ and $T_c, R_c = 0$. This is the case for example in Fig. 9.1 (a), where the photons that are not modified by the QD are eliminated by the crossed polarizer and any multi-photon state of light will be transformed into a single-photon state. This cross-polarized mode of operation could be of great interest for applications requiring a true single-photon source.

Photon bunching signatures on the other hand, are obtained in the general case when $T_1, R_1 < T_c, R_c$, as is for example shown in Fig. 9.1 (b). An initial Poisson distribution, with mean photon number $\overline{n}$ and standard deviation $\Delta n = \sqrt{\overline{n}}$, is now converted into a super–Poissonian state with $\overline{n}' < \overline{n}$ while the standard deviation $\Delta n' \approx \Delta n$ remains unchanged, and therefore $\Delta n'/\overline{n}' \approx \Delta n/\overline{n} > 1$. This implies that the bunching peak is strongly power dependent.

In reality, transitions to higher order rungs of the JC ladder, the excitation of the QD, and the fact that not every photon in the cavity interacts with the QD need to be considered as well, and the task of predicting photon correlations as function of input intensity, input and output polarizations, and QD-cavity detuning, becomes non-trivial. One approach could be to use numerical methods and solve the quantum master equation, such as provided by the Quantum Optics toolbox [40].

9.2 Cavity enhanced coupling with phonons

Electronic excitations in QDs can interact with their solid-state environment via phonons, which in principle is undesired as it decreases the coherence properties.

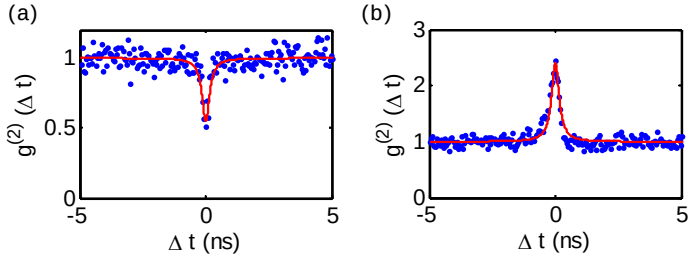

Figure 9.1: Photon time correlation measurements. (a) Anti-bunched signature, obtained at an in-coupling polarization $\theta_{in} = 45°$ while collecting reflected and transmitted light through crossed polarizers. (b) Bunched light, measured at $\theta_{in} = 0°$ while collecting the transmitted light at the same polarization.

Coupling to phonons is reduced however by the small $\sim$ 20 nm dimension of the QD, which prevents an interaction with phonons that have a larger wavelength, and by cooling down to cryogenic temperatures. Phonon–exciton coupling still occurs however and has been predicted theoretically [179], and observed experimentally [180, 181] in the form of Stokes and anti-Stokes features in the QD emission spectrum as a consequence of emission and absorption, respectively, of acoustic phonons. An asymmetry arises at low temperatures, as phonon absorption is suppressed while phonon emission still occurs.

Several theoretical proposals predict phonon–induced asymmetries to become enhanced in a coupled QD–cavity system [182, 183]. The general idea behind phonon induced dephasing is schematically depicted in Fig. 9.2. When a QD transition is detuned at the red-side of the cavity resonance and probed by a resonant laser, cavity enhanced absorption of a phonon and emission of a photon at the cavity resonance occurs, but is limited by the strong reduction of phonons at sufficiently low temperatures. A blue-detuned QD transition would experience a similar cavity-enhanced phonon induced decoherence, but then through the emission of a phonon. Unlike the red detuned case, here the decoherence process would persist even when there are initially no phonons present. This would result in an asymmetry in the QD lineshape: the faster dephasing rate at the blue-detuned side results in a broader QD feature and a smaller cooperativity.

Our system is in principle well suited to investigate such effects, as the QD-cavity detuning can be varied while keeping the temperature constant. Voltage tuning however brings the additional challenge that the QD experiences a voltage dependent dephasing rate. Within a certain voltage range or 'plateau', the charged state of the QD is well-defined, but at the edges of these plateaus fast additional co–tunneling or non-radiative decay processes of the exciton become dominant, which also gives rise to QD dephasing. It is therefore a challenge, for example in the experimental data presented in Fig. 9.2 where an asymmetry is clearly visible, to distinguish between the phonon effects and effects induced by the applied bias voltage.

One approach could be to strain-tune the QD while keeping the voltage constant, for example through the application of laser-induced surface defects which red-detune

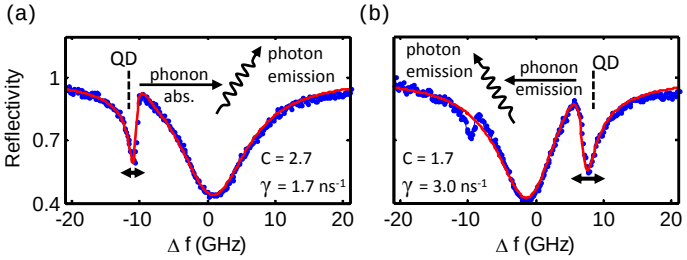

Figure 9.2: General idea behind phonon induced dephasing illustrated with measurements. (a) When a QD is red-detuned from the cavity resonance and is probed resonantly, cavity assisted absorption of a phonon and emission of a photon at the cavity frequency ($\Delta f = 0$ GHz) occurs, while for (b) a blue-detuned QD a similar process occurs but accompanied by phonon emission. At sufficiently low temperatures the phonon emission process (b) is more efficient, leading to an asymmetry in the QD dephasing rate γ.

the QD transitions [95]. Possibly it would also be beneficial to cool down to lower temperatures compared to the 9.0 K that is the current limit. As discussed in Chapter 2.1, hopefully the installation of additional temperature control of the cold head will make it possible to reach lower temperatures.

9.3 Using full polarization control for high fidelity spin–photon entanglement

In this section we will discuss some simulations on utilizing polarization control in a polarization degenerate microcavity. One of the long-term goals of this research project is to realize spin–photon entanglement by a scheme briefly discussed in Chapter 1.1. Such an experiment requires a singly charged QD with two ground states $|\uparrow\rangle$,$|\downarrow\rangle$, and the reflection or subsequent transmission of a photon depending on the spin state. The figures of merit for such a process to successfully occur could be defined as the ratio $R_\uparrow/R_\downarrow$ ($T_\downarrow/T_\uparrow$) of the spin-dependent reflectivity (transmittivity). Optimizing these ratios is also beneficial to observe spin quantum jumps [184–186], or to enhance the photon correlation features described in section 9.1. The figures of merit are however challenged by the non-unity in-coupling efficiency ($\eta \sim 0.3$ in our device) and the finite value of the QD cooperativity C. We will show that, by using a polarization degenerate cavity and clever tuning of the in- and out-coupling polarizations, these ratios can be greatly increased.

We consider a polarization degenerate cavity with a QD that has an energy level scheme as depicted in Fig. 9.3 (a). The QD is in an arbitrary superposition of the two ground states $|\Psi\rangle = \alpha\,|\uparrow\rangle + \beta\,|\downarrow\rangle$, with $|\alpha|^2 + |\beta|^2 = 1$. The general requirements for our polarization tuning scheme are that the two ground states couple to transitions of orthogonal polarization, and that there is a frequency splitting between the two levels. In the following, we simulate the case where there is a 2 GHz frequency splitting and the transitions couple to the same excited state and are linearly polarized (0° and 90°). This case could for example be achieved with a singly-charged QD and

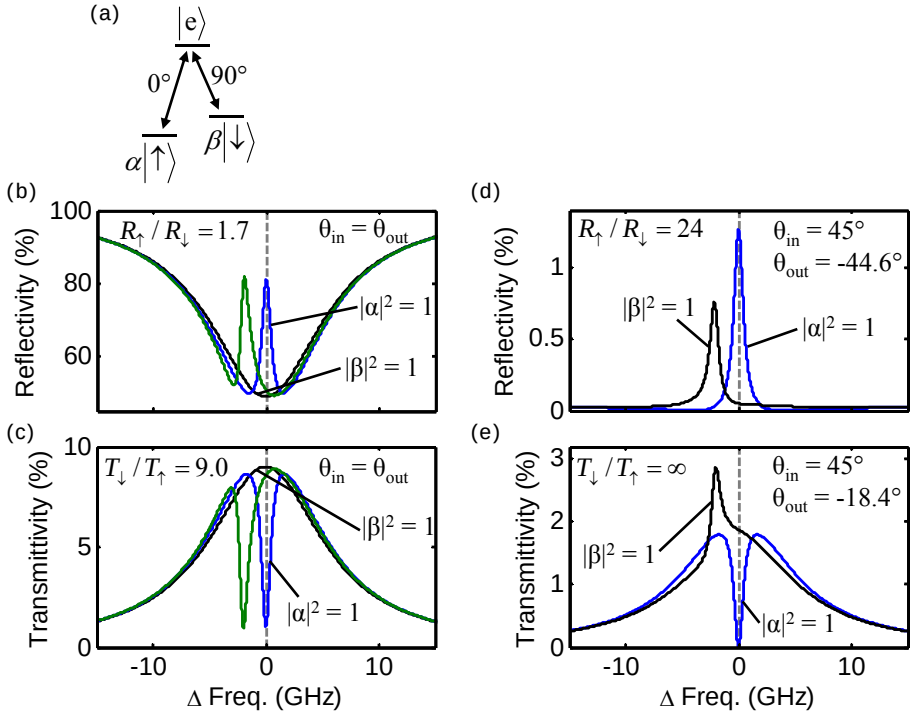

Figure 9.3: Demonstration of using detuned polarizers to increase the contrast of spin-dependent cavity reflection and transmission. (a) shows a schematic of the Zeeman split spin up/down ground states of a singly-charged QD that each couple with a linearly orthogonally polarized transition. The QD is in a superposition state $|\Psi\rangle = \alpha\,|\uparrow\rangle + \beta\,|\downarrow\rangle$. (b,c) Simulated reflectivity and transmittivity curves for the same input as output polarization. Blue curve: $\theta_{in} = 0°$ and $|\alpha|^2 = 1$, black curve: $\theta_{in} = 0°$ and $|\beta|^2 = 1$, green curve: $\theta_{in} = 90°$ and $|\beta|^2 = 1$. The fidelity is defined as the ratio between the blue and the black curve at the QD resonance indicated by the grey vertical dashed lines. (d,e) Simulated curves for $|\alpha|^2 = 1$ (blue) and $|\beta|^2 = 1$ (black), for input polarization $\theta_{in} = 45°$ and output polarization indicated in the figure window. For all the simulations $\eta = 0.3$, $\kappa = 77$ ns^{-1}, $C = 1$, $\gamma = 1$ ns^{-1} and frequency splitting of 2 GHz between the two spin states is used.

an in-plane magnetic field on the order of 1 T, see Chapter 2.3.5 and Figure 2.8 where we show this energy level scheme for a negatively charged QD. But an out-of-plane magnetic field configuration could also be used, where the ground states couple to corresponding excited states through circularly polarized transitions of different handedness and energy.

The two transitions, induced by linearly polarized light at 0° and 90°, correspond with transmission (reflection) amplitudes $t_\uparrow$ ($r_\uparrow = 1 - t_\uparrow$) and $t_\downarrow$ ($r_\downarrow = 1 - t_\downarrow$), an uncoupled cavity corresponds to transmission (reflection) amplitude t_c ($r_c = 1 - t_c$). Following methods described in Chapter 6, the transmittivity for $|\alpha|^2 = 1$ is given by $T_\uparrow = |\mathbf{e}_{out}^\dagger \begin{pmatrix} t_\uparrow & 0 \\ 0 & t_c \end{pmatrix} \mathbf{e}_{in}|^2$, while $T_\downarrow = |\mathbf{e}_{out}^\dagger \begin{pmatrix} t_c & 0 \\ 0 & t_\downarrow \end{pmatrix} \mathbf{e}_{in}|^2$ for $|\beta|^2 = 1$. Here, $\boldsymbol{e_i} = (cos(\theta_i), sin(\theta_i))$ defines the linear input/output (i =in/out) polarization with angle θ_i.

We consider a cavity with $\eta = 0.3$ and $\kappa = 77$ ns^{-1}, similar to the one studied throughout this thesis. For the QD we use $C = 1$, $\gamma = 1$ ns^{-1}, and a splitting of 2 GHz between the two transitions. Figure 9.3 (b,c) shows the reflectivity and transmittivity for the case where $\mathbf{e}_{in} = \mathbf{e}_{out}$. The blue curve shows the case for $\theta_{in} = 0°$ and $|\alpha|^2 = 1$, and the black curve shows the case for the same incoming polarization but $|\beta|^2 = 1$. The ratios between these two curves at the resonance frequency (laser-cavity detuning $\Delta f = 0$ GHz) of the spin-up transition are shown in the figure panels. The green curve shows as a reference the case for $\theta_{in} = 90°$ and $|\beta|^2 = 1$.

Figure 9.3 (d,e) shows that the fidelities can be dramatically increased by using an input polarization $\theta_{in} = 45°$ and detuning the output polarization. This does come at the expense of a reduced throughput of light through the system. In order to achieve larger fidelities and reduce losses, the in-coupling efficiency η and QD cooperativity C will have to be further increased.

9.4 Further sample improvements

All experiments described in Chapters 5-8 were performed with samples fabricated from the '131018A' wafer. There are however three shortcomings of this wafer: (i) the singly-charged QD suffers from fast decoherence, (ii) the incoupling efficiency is limited to $\eta = 0.3$, and (iii) it could be more advantageous to switch from negatively charged QDs to positively charged ones. In the following subsections we will discuss these shortcomings and propose sample improvements.

9.4.1 Charged QD decoherence

The main drawback of the samples produced from the '131018A' wafer material is that the singly-charged QDs suffer from fast decoherence. We conclude this from three observations: (i) in Chapter 6 we measured dephasing rates $\gamma \sim 9$ ns^{-1} that are a factor 20 larger than expected from the measured radiative lifetime of 1.2 ns, (ii) the crossed polarization signal shown in Fig. 6.4 (e) is too large to be explained by a 'coherent' model and seems to indicate that linear light is instantaneously projected onto a circular basis by the QD interaction (the 'incoherent' model), and (iii) the interference technique measurements shown in Fig. 8.3 in Chapter 8 demonstrate a nearly complete incoherent scattered signal. This dephasing is a limitation for using

a single charge as a spin qubit, and in general makes experiments challenging as the cooperativity $C = g^2/\kappa\gamma$ is, as we have found so far, limited to values of $C < 0.3$, to be compared to the maximum value $C = 2.5$ we found for a charge neutral QD.

We hypothesize that a fast co-tunneling process lies at the heart of this, and one thing to investigate would be to increase the tunnel barrier from 20 nm to 35 nm for a negatively charged QD sample, as was used in previous work were a QD spin-state was prepared with near-unity fidelity [107]. For future positively charged QD samples a tunnel barrier of 25 nm should be sufficient, since heavy holes have a larger effective mass compared to electrons, and this tunnel barrier thickness was used to demonstrate optical pumping of a hole spin [187],

9.4.2 In-coupling efficiency

Another drawback is the non-unity in-coupling efficiency $\eta = 2\kappa_m/(2\kappa_m + \kappa_s) \approx 0.3$. One approach to improve η is to decrease the absorption/scattering loss rate $\kappa_s \approx 5\kappa_m \approx 55$ ns^{-1} in the current sample. We hypothesize that κ_s is limited by absorption by the doped layers, and can be decreased by reducing the doping concentrations. Another approach would be to increase the mirror loss rate κ_m by using less Bragg pairs in the mirrors, but this comes at the cost of a reduced cavity Q–factor.

9.4.3 Switch from electron spins to hole spins

A final improvement would be to switch from negatively charged QDs to positively charged ones. Electron spins experience hyperfine interaction with nuclear spins which limits their coherence time. Hole spins have p-orbitals, and partially d-orbitals, and therefore experience only about 10% of the hyperfine interaction compared to electrons [188–190]. They do experience dipole-dipole coupling but this only acts in the out-of-plane growth direction, and by applying an in-plane magnetic field this effect can be canceled [191]. Several experiments have indeed demonstrated coherent properties of hole spins and promising coherence times of at least $T_2 > 100$ ns [106, 192].

An additional, but less significant, benefit of switching to hole spins, is that hole spins have a smaller in-plane g-factor compared to electron spins $|g_h| < |g_e|$ [108, 192]. The Zeeman splitting $\Delta E_h = g_{h,e}\mu_B B_x$ of the ground state is therefore smaller compared to the splitting of the excited states, which make the transitions from the ground states to the lowest energy excited state lower in energy compared to the transitions to the second excited state. This way a Λ-system is realized that is energetically separated from other unwanted transitions. This could be of interest in order to use such techniques as presented in Refs. [193, 194], where an arbitrary ground state superposition is obtained by directly mapping the polarization of an incoming light pulse onto the spin state, through a technique related to coherent population trapping.

Bibliography

[1] K. M. Birnbaum, A. Boca, R. Miller, A. D. Boozer, T. E. Northup, and H. J. Kimble, "Photon blockade in an optical cavity with one trapped atom," *Nature*, vol. 436, pp. 87–90, July 2005.

[2] D. Englund, A. Faraon, I. Fushman, N. Stoltz, P. Petroff, and J. Vuckovic, "Controlling cavity reflectivity with a single quantum dot," *Nature*, vol. 450, pp. 857–861, Dec. 2007.

[3] K. Srinivasan and O. Painter, "Linear and nonlinear optical spectroscopy of a strongly coupled microdisk-quantum dot system," *Nature*, vol. 450, pp. 862–865, Dec. 2007.

[4] B. B. Blinov, D. L. Moehring, Duan, and C. Monroe, "Observation of entanglement between a single trapped atom and a single photon," *Nature*, vol. 428, pp. 153–157, Mar. 2004.

[5] E. Togan, Y. Chu, A. S. Trifonov, L. Jiang, J. Maze, L. Childress, M. V. G. Dutt, A. S. Sorensen, P. R. Hemmer, A. S. Zibrov, and M. D. Lukin, "Quantum entanglement between an optical photon and a solid-state spin qubit," *Nature*, vol. 466, pp. 730–734, Aug. 2010.

[6] K. De Greve, L. Yu, P. L. McMahon, J. S. Pelc, C. M. Natarajan, N. Y. Kim, E. Abe, S. Maier, C. Schneider, M. Kamp, S. Hofling, R. H. Hadfield, A. Forchel, M. M. Fejer, and Y. Yamamoto, "Quantum-dot spin-photon entanglement via frequency downconversion to telecom wavelength," *Nature*, vol. 491, pp. 421–425, Nov. 2012.

[7] W. B. Gao, P. Fallahi, E. Togan, J. Miguel-Sanchez, and A. Imamoglu, "Observation of entanglement between a quantum dot spin and a single photon," *Nature*, vol. 491, pp. 426–430, Nov. 2012.

[8] L. M. Duan, M. D. Lukin, J. I. Cirac, and P. Zoller, "Long-distance quantum communication with atomic ensembles and linear optics," *Nature*, vol. 414, pp. 413–418, Nov. 2001.

[9] S. D. Barrett and P. Kok, "Efficient high-fidelity quantum computation using matter qubits and linear optics," *Phys. Rev. A*, vol. 71, p. 060310, Jun 2005.

[10] D. L. Moehring, P. Maunz, S. Olmschenk, K. C. Younge, D. N. Matsukevich, L. M. Duan, and C. Monroe, "Entanglement of single-atom quantum bits at a distance," *Nature*, vol. 449, pp. 68–71, Sept. 2007.

[11] H. Bernien, B. Hensen, W. Pfaff, G. Koolstra, M. S. Blok, L. Robledo, T. H. Taminiau, M. Markham, D. J. Twitchen, L. Childress, and R. Hanson, "Heralded entanglement between solid-state qubits separated by three metres," *Na-*

ture, vol. 497, pp. 86–90, May 2013.

[12] W. Pfaff, B. J. Hensen, H. Bernien, S. B. van Dam, M. S. Blok, T. H. Taminiau, M. J. Tiggelman, R. N. Schouten, M. Markham, D. J. Twitchen, and R. Hanson, "Unconditional quantum teleportation between distant solid-state quantum bits," *Science*, vol. 345, pp. 532–535, Aug. 2014.

[13] H. J. Kimble, "The quantum internet," *Nature*, vol. 453, pp. 1023–1030, June 2008.

[14] S. Ritter, C. Nolleke, C. Hahn, A. Reiserer, A. Neuzner, M. Uphoff, M. Mucke, E. Figueroa, J. Bochmann, and G. Rempe, "An elementary quantum network of single atoms in optical cavities," *Nature*, vol. 484, pp. 195–200, Apr. 2012.

[15] M. A. Nielsen, "Cluster-state quantum computation," *Reports on Mathematical Physics*, vol. 57, pp. 147–161, Feb. 2006.

[16] Y. L. Lim, S. D. Barrett, A. Beige, P. Kok, and L. C. Kwek, "Repeat-Until-Success quantum computing using stationary and flying qubits," Sept. 2005.

[17] H. J. Briegel, W. Dür, J. I. Cirac, and P. Zoller, "Quantum Repeaters: The Role of Imperfect Local Operations in Quantum Communication," *Physical Review Letters*, vol. 81, pp. 5932–5935, Dec. 1998.

[18] L. Childress, J. M. Taylor, A. S. Sørensen, and M. D. Lukin, "Fault-Tolerant Quantum Communication Based on Solid-State Photon Emitters," *Physical Review Letters*, vol. 96, pp. 070504+, Feb. 2006.

[19] V. Giovannetti, S. Lloyd, and L. Maccone, "Advances in quantum metrology," *Nat Photon*, vol. 5, pp. 222–229, Apr. 2011.

[20] H. J. Kimble, Y. Levin, A. B. Matsko, K. S. Thorne, and S. P. Vyatchanin, "Conversion of conventional gravitational-wave interferometers into quantum nondemolition interferometers by modifying their input and/or output optics," *Physical Review D*, vol. 65, p. 022002, Dec. 2001.

[21] J. L. O'Brien, A. Furusawa, and J. Vuckovic, "Photonic quantum technologies," *Nature Photonics*, vol. 3, pp. 687–695, Dec. 2009.

[22] C. H. Bennett and G. Brassard, "Quantum cryptography : Public key distribution and coin tossing," *Theoretical Computer Science*, Sept. 2011.

[23] A. K. Ekert, "Quantum cryptography based on Bell's theorem," *Physical Review Letters*, vol. 67, pp. 661–663, Aug. 1991.

[24] N. Gisin, G. Ribordy, W. Tittel, and H. Zbinden, "Quantum cryptography," *Reviews of Modern Physics*, vol. 74, pp. 145–195, Mar. 2002.

[25] E. Knill, R. Laflamme, and G. J. Milburn, "A scheme for efficient quantum computation with linear optics," *Nature*, vol. 409, pp. 46–52, Jan. 2001.

[26] C. S. Munoz, E. del Valle, A. G. Tudela, K. Muller, S. Lichtmannecker, M. Kaniber, C. Tejedor, J. J. Finley, and F. P. Laussy, "Emitters of N-photon bundles," *Nat Photon*, vol. 8, pp. 550–555, July 2014.

[27] I. Afek, O. Ambar, and Y. Silberberg, "High-NOON States by Mixing Quantum and Classical Light," *Science*, vol. 328, pp. 879–881, May 2010.

[28] V. Giovannetti, S. Lloyd, and L. Maccone, "Quantum-Enhanced Measurements: Beating the Standard Quantum Limit," *Science*, vol. 306, pp. 1330–1336, Nov. 2004.

[29] Z. Yuan, B. E. Kardynal, R. M. Stevenson, A. J. Shields, C. J. Lobo, K. Cooper, N. S. Beattie, D. A. Ritchie, and M. Pepper, "Electrically Driven Single-Photon Source," *Science*, vol. 295, pp. 102–105, Jan. 2002.

[30] T. Heindel, C. Schneider, M. Lermer, S. H. Kwon, T. Braun, S. Reitzenstein, S. Höfling, M. Kamp, and A. Forchel, "Electrically driven quantum dot-micropillar single photon source with 34% overall efficiency," *Applied Physics Letters*, vol. 96, p. 011107, Jan. 2010.

[31] N. Akopian, N. H. Lindner, E. Poem, Y. Berlatzky, J. Avron, D. Gershoni, B. D. Gerardot, and P. M. Petroff, "Entangled Photon Pairs from Semiconductor Quantum Dots," *Physical Review Letters*, vol. 96, p. 130501, Apr. 2006.

[32] A. Dousse, J. Suffczynski, A. Beveratos, O. Krebs, A. Lemaitre, I. Sagnes, J. Bloch, P. Voisin, and P. Senellart, "Ultrabright source of entangled photon pairs," *Nature*, vol. 466, pp. 217–220, July 2010.

[33] R. Ho, K. W. Mai, and M. A. Horowitz, "The future of wires," *Proceedings of the IEEE*, vol. 89, pp. 490–504, Apr. 2001.

[34] D. A. B. Miller, "Device requirements for dense interconnects," in *LEOS Annual Meeting Conference Proceedings, 2009. LEOS '09. IEEE*, p. 340, IEEE, Oct. 2009.

[35] E. T. Jaynes and F. W. Cummings, "Comparison of quantum and semiclassical radiation theories with application to the beam maser," *Proceedings of the IEEE*, vol. 51, pp. 89–109, Jan. 1963.

[36] C. Gardiner and M. Collett, "Input and output in damped quantum systems: Quantum stochastic differential equations and the master equation," *Physical Review A*, vol. 31, pp. 3761–3774, June 1985.

[37] A. Auffèves-Garnier, C. Simon, J.-M. Gérard, and J.-P. Poizat, "Giant optical nonlinearity induced by a single two-level system interacting with a cavity in the Purcell regime," *Phys. Rev. A*, vol. 75, pp. 053823–053838, May 2007.

[38] D. F. Walls and G. J. Milburn, *Quantum Optics*. Springer, 2nd ed., Feb. 2008.

[39] S. Fan, "Input-output formalism for few-photon transport in one-dimensional nanophotonic waveguides coupled to a qubit," *Phys. Rev. A*, vol. 82, pp. 063821–063829, Dec. 2010.

[40] S. M. Tan, "A computational toolbox for quantum and atomic optics," *Journal of Optics B: Quantum and Semiclassical Optics*, vol. 1, pp. 424–432, Aug. 1999.

[41] S. Haroche, M. Brune, and J.-M. Raimond, "Atomic clocks for controlling light fields," *Physics Today*, vol. 66, pp. 27–32, Dec. 2012.

[42] C. Monroe, "Quantum information processing with atoms and photons," *Nature*, vol. 416, pp. 238–246, Mar. 2002.

[43] C. J. Hood, T. W. Lynn, A. C. Doherty, A. S. Parkins, and H. J. Kimble, "The Atom-Cavity Microscope: Single Atoms Bound in Orbit by Single Photons," *Science*, vol. 287, pp. 1447–1453, Feb. 2000.

[44] S. P. Yu, J. D. Hood, J. A. Muniz, M. J. Martin, R. Norte, C. L. Hung, S. M. Meenehan, J. D. Cohen, O. Painter, and H. J. Kimble, "Nanowire photonic crystal waveguides for single-atom trapping and strong light-matter interactions," *Applied Physics Letters*, vol. 104, p. 111103, Mar. 2014.

[45] A. Goban, C. L. Hung, S. P. Yu, J. D. Hood, J. A. Muniz, J. H. Lee, M. J. Martin, A. C. McClung, K. S. Choi, D. E. Chang, O. Painter, and H. J. Kimble, "Atomlight interactions in photonic crystals," *Nat. Commun.*, vol. 5, no. 4808, 2014.

[46] T. G. Tiecke, J. D. Thompson, N. P. de Leon, L. R. Liu, V. Vuletic, and M. D. Lukin, "Nanophotonic quantum phase switch with a single atom," *Nature*, vol. 508, pp. 241–244, Apr. 2014.

[47] A. Wallraff, D. I. Schuster, A. Blais, L. Frunzio, Huang, J. Majer, S. Kumar, S. M. Girvin, and R. J. Schoelkopf, "Strong coupling of a single photon to a superconducting qubit using circuit quantum electrodynamics," *Nature*, vol. 431, pp. 162–167, Sept. 2004.

[48] R. Barends, J. Kelly, A. Megrant, A. Veitia, D. Sank, E. Jeffrey, T. C. White, J. Mutus, A. G. Fowler, B. Campbell, Y. Chen, Z. Chen, B. Chiaro, A. Dunsworth, C. Neill, P. O/'Malley, P. Roushan, A. Vainsencher, J. Wenner, A. N. Korotkov, A. N. Cleland, and J. M. Martinis, "Superconducting quantum circuits at the surface code threshold for fault tolerance," *Nature*, vol. 508, pp. 500–503, Apr. 2014.

[49] E. M. Purcell, H. C. Torrey, and R. V. Pound, "Resonance Absorption by Nuclear Magnetic Moments in a Solid," *Physical Review Online Archive (Prola)*, vol. 69, pp. 37–38, Jan. 1946.

[50] P. Goy, J. M. Raimond, M. Gross, and S. Haroche, "Observation of Cavity-Enhanced Single-Atom Spontaneous Emission," *Physical Review Letters*, vol. 50, pp. 1903–1906, June 1983.

[51] R. G. Hulet, E. S. Hilfer, and D. Kleppner, "Inhibited spontaneous emission by a Rydberg atom," *Physical Review Letters*, vol. 55, no. 20, pp. 2137–2140, 1985.

[52] S. Haroche and D. Kleppner, "Cavity Quantum Electrodynamics," *Physics Today*, vol. 42, pp. 24–30, Jan. 2008.

[53] D. M. Meekhof, C. Monroe, B. E. King, W. M. Itano, and D. J. Wineland, "Generation of Nonclassical Motional States of a Trapped Atom," *Physical Review Letters*, vol. 76, pp. 1796–1799, Mar. 1996.

[54] M. Brune, F. S. Kaler, A. Maali, J. Dreyer, E. Hagley, J. M. Raimond, and

S. Haroche, "Quantum Rabi Oscillation: A Direct Test of Field Quantization in a Cavity," *Physical Review Letters*, vol. 76, pp. 1800–1803, Mar. 1996.

[55] R. Thompson, G. Rempe, and H. Kimble, "Observation of normal-mode splitting for an atom in an optical cavity," *Physical Review Letters*, vol. 68, pp. 1132–1135, Feb. 1992.

[56] Q. A. Turchette, C. J. Hood, W. Lange, H. Mabuchi, and H. J. Kimble, "Measurement of Conditional Phase Shifts for Quantum Logic," *Physical Review Letters*, vol. 75, pp. 4710–4713, Dec. 1995.

[57] H. P. Specht, C. Nolleke, A. Reiserer, M. Uphoff, E. Figueroa, S. Ritter, and G. Rempe, "A single-atom quantum memory," *Nature*, vol. 473, pp. 190–193, May 2011.

[58] A. Reiserer, S. Ritter, and G. Rempe, "Nondestructive Detection of an Optical Photon," *Science*, vol. 342, pp. 1349–1351, Dec. 2013.

[59] A. Reiserer, N. Kalb, G. Rempe, and S. Ritter, "A quantum gate between a flying optical photon and a single trapped atom," *Nature*, vol. 508, pp. 237–240, Apr. 2014.

[60] M. J. Biercuk, H. Uys, A. P. VanDevender, N. Shiga, W. M. Itano, and J. J. Bollinger, "Optimized dynamical decoupling in a model quantum memory," *Nature*, vol. 458, pp. 996–1000, Apr. 2009.

[61] E. Vetsch, D. Reitz, G. Sagué, R. Schmidt, S. T. Dawkins, and A. Rauschenbeutel, "Optical Interface Created by Laser-Cooled Atoms Trapped in the Evanescent Field Surrounding an Optical Nanofiber," *Phys. Rev. Lett.*, vol. 104, p. 203603, May 2010.

[62] J. D. Thompson, T. G. Tiecke, N. P. de Leon, J. Feist, A. V. Akimov, M. Gullans, A. S. Zibrov, V. Vuletić, and M. D. Lukin, "Coupling a Single Trapped Atom to a Nanoscale Optical Cavity," *Science*, vol. 340, pp. 1202–1205, June 2013.

[63] I. Shomroni, S. Rosenblum, Y. Lovsky, O. Bechler, G. Guendelman, and B. Dayan, "All-optical routing of single photons by a one-atom switch controlled by a single photon," *Science*, vol. 345, pp. 903–906, Aug. 2014.

[64] J. Clarke and F. K. Wilhelm, "Superconducting quantum bits," *Nature*, vol. 453, pp. 1031–1042, June 2008.

[65] R. J. Schoelkopf and S. M. Girvin, "Wiring up quantum systems," *Nature*, vol. 451, pp. 664–669, Feb. 2008.

[66] M. H. Devoret and R. J. Schoelkopf, "Superconducting Circuits for Quantum Information: An Outlook," *Science*, vol. 339, pp. 1169–1174, Mar. 2013.

[67] D. Riste, M. Dukalski, C. A. Watson, G. de Lange, M. J. Tiggelman, Y. Blanter, K. W. Lehnert, R. N. Schouten, and L. DiCarlo, "Deterministic entanglement of superconducting qubits by parity measurement and feedback," *Nature*, vol. 502, pp. 350–354, Oct. 2013.

[68] R. Hanson, L. P. Kouwenhoven, J. R. Petta, S. Tarucha, and L. M. K. Vandersypen, "Spins in few-electron quantum dots," *Reviews of Modern Physics*, vol. 79, pp. 1217–1265, Oct. 2007.

[69] R. Hanson and D. D. Awschalom, "Coherent manipulation of single spins in semiconductors," *Nature*, vol. 453, pp. 1043–1049, June 2008.

[70] O. Gywat, H. J. Krenner, and J. Berezovsky, *Spins in Optically Active Quantum Dots*. Wiley-VCH, 1 ed., Feb. 2010.

[71] R. J. Warburton, "Single spins in self-assembled quantum dots," *Nat Mater*, vol. 12, pp. 483–493, June 2013.

[72] J. Berezovsky, M. H. Mikkelsen, N. G. Stoltz, L. A. Coldren, and D. D. Awschalom, "Picosecond Coherent Optical Manipulation of a Single Electron Spin in a Quantum Dot," *Science*, vol. 320, pp. 349–352, Apr. 2008.

[73] D. Press, T. D. Ladd, B. Zhang, and Y. Yamamoto, "Complete quantum control of a single quantum dot spin using ultrafast optical pulses," *Nature*, vol. 456, pp. 218–221, Nov. 2008.

[74] D. Press, K. De Greve, P. L. McMahon, T. D. Ladd, B. Friess, C. Schneider, M. Kamp, S. Hofling, A. Forchel, and Y. Yamamoto, "Ultrafast optical spin echo in a single quantum dot," *Nat Photon*, vol. 4, pp. 367–370, June 2010.

[75] W. F. Koehl, B. B. Buckley, F. J. Heremans, G. Calusine, and D. D. Awschalom, "Room temperature coherent control of defect spin qubits in silicon carbide," *Nature*, vol. 479, pp. 84–87, Nov. 2011.

[76] P. C. Maurer, G. Kucsko, C. Latta, L. Jiang, N. Y. Yao, S. D. Bennett, F. Pastawski, D. Hunger, N. Chisholm, M. Markham, D. J. Twitchen, J. I. Cirac, and M. D. Lukin, "Room-Temperature Quantum Bit Memory Exceeding One Second," *Science*, vol. 336, pp. 1283–1286, June 2012.

[77] K. Saeedi, S. Simmons, J. Z. Salvail, P. Dluhy, H. Riemann, N. V. Abrosimov, P. Becker, H.-J. Pohl, J. J. L. Morton, and M. L. W. Thewalt, "Room-Temperature Quantum Bit Storage Exceeding 39 Minutes Using Ionized Donors in Silicon-28," *Science*, vol. 342, pp. 830–833, Nov. 2013.

[78] J. Hagemeier, C. Bonato, T.-A. Truong, H. Kim, G. J. Beirne, M. Bakker, M. P. van Exter, Y. Luo, P. Petroff, and D. Bouwmeester, "H1 photonic crystal cavities for hybrid quantum information protocols," *Opt. Express*, vol. 20, no. 22, pp. 24714–24726, 2012.

[79] T. M. Sweeney, S. G. Carter, A. S. Bracker, M. Kim, C. S. Kim, L. Yang, P. M. Vora, P. G. Brereton, E. R. Cleveland, and D. Gammon, "Cavity-stimulated Raman emission from a single quantum dot spin," *Nat Photon*, vol. 8, pp. 442–447, June 2014.

[80] D. Press, S. Götzinger, S. Reitzenstein, C. Hofmann, A. Löffler, M. Kamp, A. Forchel, and Y. Yamamoto, "Photon Antibunching from a Single Quantum-Dot-Microcavity System in the Strong Coupling Regime," *Physical Review Letters*, vol. 98, p. 117402, Mar. 2007.

[81] C. Böckler, S. Reitzenstein, C. Kistner, R. Debusmann, A. Löffler, T. Kida, S. Höfling, A. Forchel, L. Grenouillet, J. Claudon, and J. M. Gérard, "Electrically driven high-Q quantum dot-micropillar cavities," *Applied Physics Letters*, vol. 92, p. 091107, Mar. 2008.

[82] A. K. Nowak, S. L. Portalupi, V. Giesz, O. Gazzano, C. Dal Savio, P. F. Braun, K. Karrai, C. Arnold, L. Lanco, I. Sagnes, A. Lemaître, and P. Senellart, "Deterministic and electrically tunable bright single-photon source," *Nature Communications*, vol. 5, Feb. 2014.

[83] J. Miguel-Sánchez, A. Reinhard, E. Togan, T. Volz, A. Imamoglu, B. Besga, J. Reichel, and J. Estève, "Cavity quantum electrodynamics with charge-controlled quantum dots coupled to a fiber FabryPerot cavity," *New Journal of Physics*, vol. 15, p. 045002, Apr. 2013.

[84] S. G. Carter, T. M. Sweeney, M. Kim, C. S. Kim, D. Solenov, S. E. Economou, T. L. Reinecke, L. Yang, A. S. Bracker, and D. Gammon, "Quantum control of a spin qubit coupled to a photonic crystal cavity," *Nat Photon*, vol. 7, pp. 329–334, Apr. 2013.

[85] T. Yoshie, A. Scherer, J. Hendrickson, G. Khitrova, H. M. Gibbs, G. Rupper, C. Ell, O. B. Shchekin, and D. G. Deppe, "Vacuum Rabi splitting with a single quantum dot in a photonic crystal nanocavity," *Nature*, vol. 432, pp. 200–203, Nov. 2004.

[86] M. Arcari, I. Söllner, A. Javadi, S. Lindskov Hansen, S. Mahmoodian, J. Liu, H. Thyrrestrup, H. Lee, E. D. Song, J. S. Stobbe, and P. Lodahl, "Near-unity coupling efficiency of a quantum emitter to a photonic crystal waveguide," *Phys. Rev. Lett.*, vol. 113, p. 093603, Aug 2014.

[87] K. Hennessy, C. Högerle, E. Hu, A. Badolato, and A. Imamoğlu, "Tuning photonic nanocavities by atomic force microscope nano-oxidation," *Applied Physics Letters*, vol. 89, p. 041118, July 2006.

[88] K. Hennessy, A. Badolato, M. Winger, D. Gerace, M. Atature, S. Gulde, S. Falt, E. L. Hu, and A. Imamoglu, "Quantum nature of a strongly coupled single quantum dot-cavity system," *Nature*, vol. 445, pp. 896–899, Feb. 2007.

[89] S. M. Thon, M. T. Rakher, H. Kim, J. Gudat, W. T. M. Irvine, P. M. Petroff, and D. Bouwmeester, "Strong coupling through optical positioning of a quantum dot in a photonic crystal cavity," *Applied Physics Letters*, vol. 94, p. 111115, Mar. 2009.

[90] S. Sun, H. Kim, G. S. Solomon, and E. Waks, "Strain tuning of a quantum dot strongly coupled to a photonic crystal cavity," *Applied Physics Letters*, vol. 103, pp. 151102+, Oct. 2013.

[91] J. P. Reithmaier, G. Sek, A. Loffler, C. Hofmann, S. Kuhn, S. Reitzenstein, L. V. Keldysh, V. D. Kulakovskii, T. L. Reinecke, and A. Forchel, "Strong coupling in a single quantum dot-semiconductor microcavity system," *Nature*, vol. 432, pp. 197–200, Nov. 2004.

[92] A. Dousse, L. Lanco, J. Suffczyński, E. Semenova, A. Miard, A. Lemaître, I. Sagnes, C. Roblin, J. Bloch, and P. Senellart, "Controlled Light-Matter Coupling for a Single Quantum Dot Embedded in a Pillar Microcavity Using Far-Field Optical Lithography," *Physical Review Letters*, vol. 101, p. 267404, Dec. 2008.

[93] R. Albrecht, A. Bommer, C. Deutsch, J. Reichel, and C. Becher, "Coupling of a single nitrogen-vacancy center in diamond to a fiber-based microcavity," *Phys. Rev. Lett.*, vol. 110, p. 243602, Jun 2013.

[94] C. Bonato, D. Ding, J. Gudat, S. Thon, H. Kim, P. M. Petroff, M. P. van Exter, and D. Bouwmeester, "Tuning micropillar cavity birefringence by laser induced surface defects," *Applied Physics Letters*, vol. 95, no. 25, p. 251104, 2009.

[95] J. Gudat, C. Bonato, E. van Nieuwenburg, S. Thon, H. Kim, P. M. Petroff, M. P. van Exter, and D. Bouwmeester, "Permanent tuning of quantum dot transitions to degenerate microcavity resonances," *Applied Physics Letters*, vol. 98, p. 121111, Mar. 2011.

[96] M. P. Bakker, A. V. Barve, A. Zhan, L. A. Coldren, M. P. van Exter, and D. Bouwmeester, "Polarization degenerate micropillars fabricated by designing elliptical oxide apertures," *Applied Physics Letters*, vol. 104, p. 151109, Apr. 2014.

[97] P. W. Fry, J. J. Finley, L. R. Wilson, A. Lemaître, D. J. Mowbray, M. S. Skolnick, M. Hopkinson, G. Hill, and J. C. Clark, "Electric-field-dependent carrier capture and escape in self-assembled InAs/GaAs quantum dots," *Applied Physics Letters*, vol. 77, no. 26, pp. 4344–4346, 2000.

[98] N. G. Stoltz, M. Rakher, S. Strauf, A. Badolato, D. D. Lofgreen, P. M. Petroff, L. A. Coldren, and D. Bouwmeester, "High-quality factor optical microcavities using oxide apertured micropillars," *Applied Physics Letters*, vol. 87, no. 3, p. 031105, 2005.

[99] S. Strauf, N. G. Stoltz, M. T. Rakher, L. A. Coldren, P. M. Petroff, and D. Bouwmeester, "High-frequency single-photon source with polarization control," *Nature Photonics*, vol. 1, pp. 704–708, Nov. 2007.

[100] M. T. Rakher, N. G. Stoltz, L. A. Coldren, P. M. Petroff, and D. Bouwmeester, "Externally Mode-Matched Cavity Quantum Electrodynamics with Charge-Tunable Quantum Dots," *Physical Review Letters*, vol. 102, p. 097403, Mar. 2009.

[101] C. J. R. Sheppard, "Approximate calculation of the reflection coefficient from a stratified medium," *Pure and Applied Optics: Journal of the European Optical Society Part A*, vol. 4, p. 665, Sept. 1995.

[102] L. R. Brovelli and U. Keller, "Simple analytical expressions for the reflectivity and the penetration depth of a Bragg mirror between arbitrary media," *Optics Communications*, vol. 116, pp. 343–350, May 1995.

[103] C. Bonato, J. Gudat, K. de Vries, S. M. Thon, H. Kim, P. M. Petroff, M. P.

van Exter, and D. Bouwmeester, "Optical modes in oxide-apertured micropillar cavities," *Opt. Lett.*, vol. 37, pp. 4678–4680, Nov. 2012.

[104] D. Leonard, K. Pond, and P. M. Petroff, "Critical layer thickness for self-assembled InAs islands on GaAs," *Physical Review B*, vol. 50, pp. 11687–11692, Oct. 1994.

[105] P. M. Petroff, A. Lorke, and A. Imamoglu, "Epitaxially self-assembled quantum dots," *Physics Today*, vol. 54, pp. 46–52, May 2001.

[106] D. Brunner, B. D. Gerardot, P. A. Dalgarno, G. Wüst, K. Karrai, N. G. Stoltz, P. M. Petroff, and R. J. Warburton, "A Coherent Single-Hole Spin in a Semiconductor," *Science*, vol. 325, pp. 70–72, July 2009.

[107] M. Atatüre, J. Dreiser, A. Badolato, A. Högele, K. Karrai, and A. Imamoglu, "Quantum-Dot Spin-State Preparation with Near-Unity Fidelity," *Science*, vol. 312, pp. 551–553, Apr. 2006.

[108] X. Xu, Y. Wu, B. Sun, Q. Huang, J. Cheng, D. G. Steel, A. S. Bracker, D. Gammon, C. Emary, and L. J. Sham, "Fast spin state initialization in a singly charged inas-gaas quantum dot by optical cooling," *Phys. Rev. Lett.*, vol. 99, p. 097401, Aug 2007.

[109] X. Xu, B. Sun, P. R. Berman, D. G. Steel, A. S. Bracker, D. Gammon, and L. J. Sham, "Coherent population trapping of an electron spin in a single negatively charged quantum dot," *Nat Phys*, vol. 4, pp. 692–695, Sept. 2008.

[110] A. G. Baca and C. I. H. Ashby, *Fabrication of GaAs Devices.* The Insititution of Engineering and Technology, 2005.

[111] D. Wiedenmann, M. Grabherr, R. Jäger, and R. King, "High volume production of single-mode VCSELs," *Proc. SPIE*, vol. 6132, pp. 1–12, 2008.

[112] C. Bonato, F. Haupt, S. S. R. Oemrawsingh, J. Gudat, D. Ding, M. P. van Exter, and D. Bouwmeester, "CNOT and Bell-state analysis in the weak-coupling cavity QED regime," *Physical Review Letters*, vol. 104, p. 160503, Apr. 2010.

[113] A. Sakamoto, H. Nakayama, and T. Nakamuro, "Fabrication control during AlAs oxidation of the VCSELs via optical probing technique of AlAs lateral oxidation (OPTALO)," *Proc. SPIE*, vol. 4649, pp. 211–217, 2002.

[114] S. A. Feld, J. P. Loehr, R. E. Sherriff, J. Wiemeri, and R. Kaspi, "In situ optical monitoring of AlAs wet oxidation using a novel low-temperature low-pressure steam furnace design," *Photonics Technology Letters, IEEE*, vol. 10, pp. 197–199, Feb. 1998.

[115] G. Almuneau, R. Bossuyt, P. Collière, L. Bouscayrol, M. Condé, I. Suarez, V. Bardinal, and C. Fontaine, "Real-time in situ monitoring of wet thermal oxidation for precise confinement in VCSELs," *Semiconductor Science and Technology*, vol. 23, p. 105021, Sept. 2008.

[116] G. Ctistis, A. Hartsuiker, E. van der Pol, J. Claudon, W. L. Vos, and J. M. Gérard, "Optical characterization and selective addressing of the resonant

modes of a micropillar cavity with a white light beam," *Physical Review B*, vol. 82, p. 195330, Nov. 2010.

[117] K. J. Vahala, "Optical microcavities," *Nature*, vol. 424, pp. 839–846, Aug. 2003.

[118] M. P. Bakker, D. J. Suntrup, H. Snijders, T.-A. Truong, P. M. Petroff, M. P. van Exter, and D. Bouwmeester, "Monitoring the formation of oxide apertures in micropillar cavities," *Applied Physics Letters*, vol. 102, p. 101109, Mar. 2013.

[119] A. J. Bennett, D. J. P. Ellis, A. J. Shields, P. Atkinson, I. Farrer, and D. A. Ritchie, "Observation of the Purcell effect in high-index-contrast micropillars," *Applied Physics Letters*, vol. 90, no. 19, p. 191911, 2007.

[120] O. Blum, C. I. H. Ashby, and H. Q. Hou, "Barrier-layer-thickness control of selective wet oxidation of AlGaAs for embedded optical elements," *Applied Physics Letters*, vol. 70, no. 21, pp. 2870–2872, 1997.

[121] G. R. Hadley, "Effective index model for vertical-cavity surface-emitting lasers," *Opt. Lett.*, vol. 20, pp. 1483–1485, July 1995.

[122] S. Reitzenstein and A. Forchel, "Quantum dot micropillars," *Journal of Physics D: Applied Physics*, vol. 43, p. 033001, Jan. 2010.

[123] K. Panajotov, B. Nagler, G. Verschaffelt, A. Georgievski, H. Thienpont, J. Danckaert, and I. Veretennicoff, "Impact of in-plane anisotropic strain on the polarization behavior of vertical-cavity surface-emitting lasers," *Applied Physics Letters*, vol. 77, pp. 1590–1592, Sept. 2000.

[124] A. K. J. van Doorn, M. P. van Exter, and J. P. Woerdman, "Elastooptic anisotropy and polarization orientation of verticalcavity surfaceemitting semiconductor lasers," *Applied Physics Letters*, vol. 69, pp. 1041–1043, Aug. 1996.

[125] A. W. Snyder and J. Love, *Optical Waveguide Theory*. 1983.

[126] A. Weisshaar, J. Li, R. L. Gallawa, and I. C. Goyal, "Vector and quasi-vector solutions for optical waveguide modes using efficient Galerkin's method with Hermite-Gauss basis functions," *Lightwave Technology, Journal of*, vol. 13, pp. 1795–1800, Aug. 1995.

[127] E. Waks and C. Monroe, "Protocol for hybrid entanglement between a trapped atom and a quantum dot," *Phys. Rev. A*, vol. 80, p. 062330, Dec 2009.

[128] J. Cirac, A. Ekert, S. Huelga, and C. Macchiavello, "Distributed quantum computation over noisy channels," *Phys. Rev. A*, vol. 59, pp. 4249–4254, Jun 1999.

[129] W. Yao, R.-B. Liu, and L. Sham, "Theory of control of the spin-photon interface for quantum networks," *Phys. Rev. Lett.*, vol. 95, p. 030504, Jul 2005.

[130] J. Schaibley, A. Burgers, G. McCracken, L.-M. Duan, P. Berman, D. Steel, A. Bracker, D. Gammon, and L. Sham, "Demonstration of quantum entanglement between a single electron spin confined to an inas quantum dot and a photon," *Phys. Rev. Lett.*, vol. 110, p. 167401, Apr 2013.

[131] C. Hu, W. Munro, J. O'Brien, and J. Rarity, "Proposed entanglement beam splitter using a quantum-dot spin in a double-sided optical microcavity," *Phys.*

Rev. B, vol. 80, p. 205326, Nov 2009.

[132] S. Sun and E. Waks, "Deterministic generation of entanglement between a quantum-dot spin and a photon," *Phys. Rev. A*, vol. 90, p. 042322, Oct 2014.

[133] V. Loo, C. Arnold, O. Gazzano, A. Lemaître, I. Sagnes, O. Krebs, P. Voisin, P. Senellart, and L. Lanco, "Optical Nonlinearity for Few-Photon Pulses on a Quantum Dot-Pillar Cavity Device," *Phys. Rev. Lett.*, vol. 109, pp. 166806–166810, Oct. 2012.

[134] Fry, "Inverted Electron-Hole Alignment in InAs-GaAs Self-Assembled Quantum Dots," *Phys. Rev. Lett.*, vol. 84, pp. 733–736, Jan. 2000.

[135] R. J. Warburton, C. Schaflein, D. Haft, F. Bickel, A. Lorke, K. Karrai, J. M. Garcia, W. Schoenfeld, and P. M. Petroff, "Optical emission from a charge-tunable quantum ring," *Nature*, vol. 405, pp. 926–929, June 2000.

[136] S. Seidl, M. Kroner, A. Hgele, K. Karrai, R. J. Warburton, A. Badolato, and P. M. Petroff, "Effect of uniaxial stress on excitons in a self-assembled quantum dot," *Applied Physics Letters*, vol. 88, p. 203113, 2006.

[137] J. Houel, A. V. Kuhlmann, L. Greuter, F. Xue, M. Poggio, B. D. Gerardot, P. A. Dalgarno, A. Badolato, P. M. Petroff, A. Ludwig, D. Reuter, A. D. Wieck, and R. J. Warburton, "Probing single-charge fluctuations at a gaas/alas interface using laser spectroscopy on a nearby ingaas quantum dot," *Phys. Rev. Lett.*, vol. 108, pp. 107401–107405, Mar. 2012.

[138] B. Urbaszek, X. Marie, T. Amand, O. Krebs, P. Voisin, P. Maletinsky, A. Högele, and A. Imamoglu, "Nuclear spin physics in quantum dots: An optical investigation," *Rev. Mod. Phys.*, vol. 85, pp. 79–133, Jan. 2013.

[139] E. Waks and J. Vuckovic, "Dipole Induced Transparency in Drop-Filter Cavity-Waveguide Systems," *Phys. Rev. Lett.*, vol. 96, pp. 153601–153604, Apr. 2006.

[140] A. Högele, M. Kroner, S. Seidl, K. Karrai, M. Atatüre, J. Dreiser, A. Imamoğlu, R. J. Warburton, A. Badolato, B. D. Gerardot, and P. M. Petroff, "Spin-selective optical absorption of singly charged excitons in a quantum dot," *Applied Physics Letters*, vol. 86, p. 221905, May 2005.

[141] D. E. Chang, A. S. Sorensen, E. A. Demler, and M. D. Lukin, "A single-photon transistor using nanoscale surface plasmons," *Nature Physics*, vol. 3, pp. 807–812, Aug. 2007.

[142] D. Englund, A. Majumdar, M. Bajcsy, A. Faraon, P. Petroff, and J. Vučković, "Ultrafast Photon-Photon Interaction in a Strongly Coupled Quantum Dot-Cavity System," *Physical Review Letters*, vol. 108, p. 093604, Mar. 2012.

[143] R. Bose, D. Sridharan, H. Kim, G. S. Solomon, and E. Waks, "Low-photon-number optical switching with a single quantum dot coupled to a photonic crystal cavity," *Phys. Rev. Lett.*, vol. 108, p. 227402, May 2012.

[144] T. Volz, A. Reinhard, M. Winger, A. Badolato, K. J. Hennessy, E. L. Hu, and A. Imamoglu, "Ultrafast all-optical switching by single photons," *Nat Photon*,

vol. 6, pp. 605–609, Sept. 2012.

[145] I. Fushman, D. Englund, A. Faraon, N. Stoltz, P. Petroff, and J. Vučković, "Controlled Phase Shifts with a Single Quantum Dot," *Science*, vol. 320, pp. 769–772, May 2008.

[146] A. Majumdar, M. Bajcsy, A. Rundquist, and J. Vučković, "Loss-Enabled Sub-Poissonian Light Generation in a Bimodal Nanocavity," *Phys. Rev. Lett.*, vol. 108, pp. 183601–183605, May 2012.

[147] E. A. Chekhovich, M. N. Makhonin, A. I. Tartakovskii, A. Yacoby, H. Bluhm, K. C. Nowack, and L. M. K. Vandersypen, "Nuclear spin effects in semiconductor quantum dots," *Nat Mater*, vol. 12, pp. 494–504, June 2013.

[148] A. V. Kuhlmann, J. Houel, A. Ludwig, L. Greuter, D. Reuter, A. D. Wieck, M. Poggio, and R. J. Warburton, "Charge noise and spin noise in a semiconductor quantum device," *Nat Phys*, vol. 9, pp. 570–575, Sept. 2013.

[149] S. M. Sze and K. K. Ng, *Physics of Semiconductor Devices*. Wiley-Interscience, 3 ed., Oct. 2006.

[150] R. D. Twesten, D. M. Follstaedt, K. D. Choquette, and R. P. Schneider, "Microstructure of laterally oxidized AlxGa1xAs layers in verticalcavity lasers," *Applied Physics Letters*, vol. 69, pp. 19–21, July 1996.

[151] C. I. H. Ashby, J. P. Sullivan, P. P. Newcomer, N. A. Missert, H. Q. Hou, B. E. Hammons, M. J. Hafich, and A. G. Baca, "Wet oxidation of AlxGa1xAs: Temporal evolution of composition and microstructure and the implications for metal-insulator-semiconductor applications," *Applied Physics Letters*, vol. 70, pp. 2443–2445, May 1997.

[152] E. I. Chen, N. Holonyak, and S. A. Maranowski, "AlxGa1xAsGaAs metaloxide semiconductor field effect transistors formed by lateral water vapor oxidation of AlAs," *Applied Physics Letters*, vol. 66, pp. 2688–2690, May 1995.

[153] C. Arnold, V. Loo, A. Lemaître, I. Sagnes, O. Krebs, P. Voisin, P. Senellart, and L. Lanco, "Cavity-Enhanced Real-Time Monitoring of Single-Charge Jumps at the Microsecond Time Scale," *Phys. Rev. X*, vol. 4, pp. 021004–021009, Apr. 2014.

[154] P. F. Braun, B. Urbaszek, T. Amand, X. Marie, O. Krebs, B. Eble, A. Lemaitre, and P. Voisin, "Bistability of the nuclear polarization created through optical pumping in $ in1-x gax as $ quantum dots," *Physical Review B*, vol. 74, p. 245306, Dec. 2006.

[155] A. I. Tartakovskii, T. Wright, A. Russell, V. I. Fal'ko, A. B. Van'kov, J. Skiba-Szymanska, I. Drouzas, R. S. Kolodka, M. S. Skolnick, P. W. Fry, A. Tahraoui, H.-Y. Liu, and M. Hopkinson, "Nuclear Spin Switch in Semiconductor Quantum Dots," *Phys. Rev. Lett.*, vol. 98, pp. 026806–026809, Jan. 2007.

[156] P. Maletinsky, A. Badolato, and A. Imamoglu, "Dynamics of Quantum Dot Nuclear Spin Polarization Controlled by a Single Electron," *Phys. Rev. Lett.*, vol. 99, pp. 056804–056808, Aug. 2007.

[157] B. Eble, O. Krebs, A. Lemaître, K. Kowalik, A. Kudelski, P. Voisin, B. Urbaszek, X. Marie, and T. Amand, "Dynamic nuclear polarization of a single charge-tunable inas/gaas quantum dot," *Phys. Rev. B*, vol. 74, pp. 081306–081309, Aug. 2006.

[158] C. Latta, A. Hogele, Y. Zhao, A. N. Vamivakas, P. Maletinsky, M. Kroner, J. Dreiser, I. Carusotto, A. Badolato, D. Schuh, W. Wegscheider, M. Atature, and A. Imamoglu, "Confluence of resonant laser excitation and bidirectional quantum-dot nuclear-spin polarization," *Nat Phys*, vol. 5, pp. 758–763, Oct. 2009.

[159] A. Högele, M. Kroner, C. Latta, M. Claassen, I. Carusotto, C. Bulutay, and A. Imamoglu, "Dynamic Nuclear Spin Polarization in the Resonant Laser Excitation of an InGaAs Quantum Dot," *Phys. Rev. Lett.*, vol. 108, pp. 197403–197408, May 2012.

[160] C. Y. Hu, W. J. Munro, and J. G. Rarity, "Deterministic photon entangler using a charged quantum dot inside a microcavity," *Physical Review B (Condensed Matter and Materials Physics)*, vol. 78, no. 12, p. 125318, 2008.

[161] H. J. Kimble, M. Dagenais, and L. Mandel, "Photon antibunching in resonance fluorescence," *Phys. Rev. Lett.*, vol. 39, pp. 691–695, Sep 1977.

[162] T. Basché, W. E. Moerner, M. Orrit, and H. Talon, "Photon antibunching in the fluorescence of a single dye molecule trapped in a solid," *Phys. Rev. Lett.*, vol. 69, pp. 1516–1519, Sep 1992.

[163] T. Plakhotnik and V. Palm, "Interferometric signatures of single molecules," *Phys. Rev. Lett.*, vol. 87, p. 183602, Oct 2001.

[164] G. Wrigge, I. Gerhardt, J. Hwang, G. Zumofen, and V. Sandoghdar, "Efficient coupling of photons to a single molecule and the observation of its resonance fluorescence," *Nat Phys*, vol. 4, pp. 60–66, Jan. 2008.

[165] A. Muller, E. B. Flagg, P. Bianucci, X. Y. Wang, D. G. Deppe, W. Ma, J. Zhang, G. J. Salamo, M. Xiao, and C. K. Shih, "Resonance Fluorescence from a Coherently Driven Semiconductor Quantum Dot in a Cavity," *Physical Review Letters*, vol. 99, p. 187402, Nov. 2007.

[166] A. Nick Vamivakas, Y. Zhao, C.-Y. Lu, and M. Atature, "Spin-resolved quantum-dot resonance fluorescence," *Nat Phys*, vol. 5, pp. 198–202, Mar. 2009.

[167] E. B. Flagg, A. Muller, J. W. Robertson, S. Founta, D. G. Deppe, M. Xiao, W. Ma, G. J. Salamo, and C. K. Shih, "Resonantly driven coherent oscillations in a solid-state quantum emitter," *Nat Phys*, vol. 5, pp. 203–207, Mar. 2009.

[168] K. Konthasinghe, J. Walker, M. Peiris, C. K. Shih, Y. Yu, M. F. Li, J. F. He, L. J. Wang, H. Q. Ni, Z. C. Niu, and A. Muller, "Coherent versus incoherent light scattering from a quantum dot," *Phys. Rev. B*, vol. 85, p. 235315, June 2012.

[169] A. B. Young, R. Oulton, C. Y. Hu, A. C. T. Thijssen, C. Schneider, S. Reitzenstein, M. Kamp, S. Höfling, L. Worschech, A. Forchel, and J. G. Rar-

ity, "Quantum-dot-induced phase shift in a pillar microcavity," *Phys. Rev. A*, vol. 84, p. 011803, Jul 2011.

[170] M. P. Bakker, A. V. Barve, T. Ruytenberg, W. Löffler, L. A. Coldren, D. Bouwmeester, and M. P. van Exter, "Polarization degenerate solid-state cavity quantum electrodynamics," *Phys. Rev. B*, vol. 91, p. 115319, Mar 2015.

[171] M. P. Bakker, T. Ruytenberg, W. Löffler, A. V. Barve, L. Coldren, M. P. van Exter, and D. Bouwmeester, "Quantum dot nonlinearity through cavity-enhanced feedback with a charge memory," Mar. 2015. http://arxiv.org/abs/1503.08142.

[172] R. Loudon, *The Quantum Theory of Light (Oxford Science Publications)*. Oxford University Press, USA, 3 ed., Sept. 2000.

[173] C. Sames, H. Chibani, C. Hamsen, A. Altin, P., T. Wilk, and G. Rempe, "Antiresonance phase shift in strongly coupled cavity qed," *Phys. Rev. Lett.*, vol. 112, p. 043601, Jan 2014.

[174] W. Chen, K. M. Beck, R. Bücker, M. Gullans, M. D. Lukin, H. Tanji-Suzuki, and V. Vuletić, "All-Optical Switch and Transistor Gated by One Stored Photon," *Science*, vol. 341, pp. 768–770, Aug. 2013.

[175] H. Kim, R. Bose, T. C. Shen, G. S. Solomon, and E. Waks, "A quantum logic gate between a solid-state quantum bit and a photon," *Nat Photon*, vol. 7, pp. 373–377, May 2013.

[176] F. P. Laussy, E. del Valle, M. Schrapp, A. Laucht, and J. J. Finley, "Climbing the JaynesCummings ladder by photon counting," *Journal of Nanophotonics*, vol. 6, p. 061803, Nov. 2012.

[177] A. Majumdar, M. Bajcsy, and J. Vučković, "Probing the ladder of dressed states and nonclassical light generation in quantum-dot˘cavity qed," *Physical Review A*, vol. 85, p. 041801, Apr. 2012.

[178] A. Rundquist, M. Bajcsy, A. Majumdar, T. Sarmiento, K. Fischer, K. G. Lagoudakis, S. Buckley, A. Y. Piggott, and J. Vučković, "Nonclassical higher-order photon correlations with a quantum dot strongly coupled to a photonic-crystal nanocavity," *Phys. Rev. A*, vol. 90, p. 023846, Aug 2014.

[179] Ahn, "Resonance fluorescence of semiconductor quantum dots: Signatures of the electron-phonon interaction," *Phys. Rev. B*, vol. 71, pp. 153309–153312, Apr. 2005.

[180] L. Besombes, K. Kheng, L. Marsal, and H. Mariette, "Acoustic phonon broadening mechanism in single quantum dot emission," *Physical Review B*, vol. 63, p. 155307, Mar. 2001.

[181] P. Borri, W. Langbein, S. Schneider, U. Woggon, R. L. Sellin, D. Ouyang, and D. Bimberg, "Ultralong Dephasing Time in InGaAs Quantum Dots," *Physical Review Letters*, vol. 87, p. 157401, Sept. 2001.

[182] P. Kaer, T. R. Nielsen, P. Lodahl, A.-P. Jauho, and J. Mørk, "Microscopic theory of phonon-induced effects on semiconductor quantum dot decay dynamics

in cavity QED," *Phys. Rev. B*, vol. 86, pp. 085302–085321, Aug. 2012.

[183] J. Iles-Smith and A. Nazir, "Probing emitter-cavity dressed states through environmental transitions," Jan. 2015. http://arxiv.org/abs/1412.6044.

[184] M. P. van Exter, J. Gudat, G. Nienhuis, and D. Bouwmeester, "Spin quantum jumps in a singly charged quantum dot," *Physical Review A*, vol. 80, p. 023812, Aug. 2009.

[185] A. N. Vamivakas, C. Y. Lu, C. Matthiesen, Y. Zhao, S. Falt, A. Badolato, and M. Atature, "Observation of spin-dependent quantum jumps via quantum dot resonance fluorescence," *Nature*, vol. 467, pp. 297–300, Sept. 2010.

[186] A. Delteil, W.-b. Gao, P. Fallahi, J. Miguel-Sanchez, and A. Imamoğlu, "Observation of quantum jumps of a single quantum dot spin using submicrosecond single-shot optical readout," *Phys. Rev. Lett.*, vol. 112, p. 116802, Mar 2014.

[187] B. D. Gerardot, D. Brunner, P. A. Dalgarno, P. Ohberg, S. Seidl, M. Kroner, K. Karrai, N. G. Stoltz, P. M. Petroff, and R. J. Warburton, "Optical pumping of a single hole spin in a quantum dot," *Nature*, vol. 451, pp. 441–444, Jan. 2008.

[188] P. Fallahi, S. T. Y ılmaz, and A. Imamoğlu, "Measurement of a heavy-hole hyperfine interaction in ingaas quantum dots using resonance fluorescence," *Phys. Rev. Lett.*, vol. 105, p. 257402, Dec 2010.

[189] E. A. Chekhovich, A. B. Krysa, M. S. Skolnick, and A. I. Tartakovskii, "Direct measurement of the hole-nuclear spin interaction in single inp/gainp quantum dots using photoluminescence spectroscopy," *Phys. Rev. Lett.*, vol. 106, p. 027402, Jan 2011.

[190] E. A. Chekhovich, M. M. Glazov, A. B. Krysa, M. Hopkinson, P. Senellart, A. Lemaitre, M. S. Skolnick, and A. I. Tartakovskii, "Element-sensitive measurement of the hole-nuclear spin interaction in quantum dots," *Nature Physics*, vol. 9, pp. 74–78, Dec. 2012.

[191] J. Fischer, "Spin decoherence of a heavy hole coupled to nuclear spins in a quantum dot," *Phys. Rev. B*, vol. 78, pp. 155329–155337, Oct. 2008.

[192] J. Houel, J. H. Prechtel, A. V. Kuhlmann, D. Brunner, C. E. Kuklewicz, B. D. Gerardot, N. G. Stoltz, P. M. Petroff, and R. J. Warburton, "High resolution coherent population trapping on a single hole spin in a semiconductor quantum dot," *Phys. Rev. Lett.*, vol. 112, p. 107401, Mar 2014.

[193] S. Z. Denega, M. Sladkov, D. Reuter, A. D. Wieck, T. L. C. Jansen, and C. H. van der Wal, "Ultrafast mapping of optical polarization states onto spin coherence of localized electrons in a semiconductor," Apr. 2011. http://arxiv.org/abs/1103.4307.

[194] C. G. Yale, B. B. Buckley, D. J. Christle, G. Burkard, F. J. Heremans, L. C. Bassett, and D. D. Awschalom, "All-optical control of a solid-state spin using coherent dark states," *Proceedings of the National Academy of Sciences*, vol. 110, pp. 7595–7600, May 2013.

Summary

In this thesis I have investigated 'quantum dots' (QDs) in optical microcavities. In this summary it will be explained how QDs and optical microcavities work, and what in summary the results are that were obtained during my promotion and that are presented in this thesis.

QDs are very small 3D structures consisting of a semiconductor material, Indium Arsenide (InAs), that is surrounded by another semiconductor material, Gallium Arsenide (GaAs). Figure 9.4 (a) shows an electron microscope image of the cross-section of a QD. QDs are spontaneously formed by first depositing InAs on a GaAs substrate, which causes small 'droplets' to be formed. Next, these InAs droplets are covered with GaAs. QDs consist of only $10.000 - 100.000$ In and As atoms, and have a pancake-like shape with a diameter of ~ 40 nm (a nm is equal to 10^{-9} meter) and a height of $1 - 2$ nm. InAs has the property that charges in this material have a lower energy than charges in the surrounding GaAs, and charges are therefore confined inside the QD. Furthermore, QDs are optically active, which means that they can absorb a light particle, which is called a photon, and subsequently emit it again. This process is schematically shown in Fig. 9.4 (b). The optical transitions are spectrally narrow, which means that only photons with a certain wavelength (or color) interact; QDs are therefore also called artificial atoms.

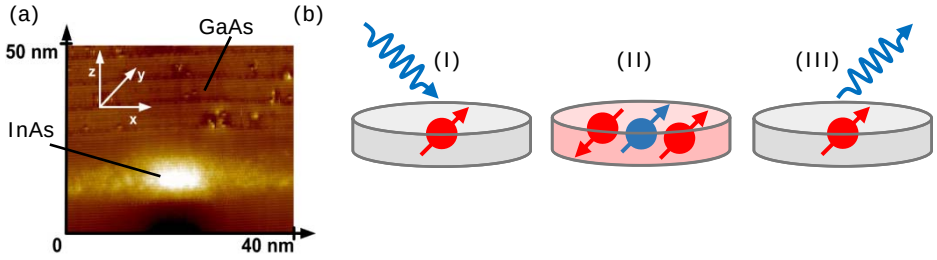

Figure 9.4: (a) Electron microscope image of an InAs quantum dot (QD) embedded inside a GaAs crystal. (b) Schematic representation of the absorption and emission of a photon by a QD charged with a single electron (red ball). (I) A photon is incident on the QD, (II) an electron and hole (blue ball) pair is created, and (III) a photon is emitted.

QDs are grown by our research group in such a structure, that the total charge in the QD can be controlled, such that only a single electron can be put inside it. A confined electron behaves according to the laws of quantum mechanics and is of interest because it can serve as a building block of a new type of 'quantum' computer. This computer would make use of the special properties of quantum mechanics and

can therefore perform certain calculations much faster than a 'classical' computer. Furthermore, research on QDs is driven by curiosity; as QDs behave according to the laws of quantum mechanics, it is an exciting challenge to see to what extent predictions from these laws can be measured in a laboratory.

Studying, reading-out, and interconnecting QDs can be done using single photons. However, the interaction probability between light and a QD is very small (typically only a couple of percent), as is the same for the chance to collect an emitted photon. This makes experiments challenging, but is also a severe limitation for applications. The solution is to use very small optical microcavities, where 'micro' refers to the μm scale dimensions of the cavities (one μm is equal to 10^{-6} meter). Light that enters a cavity and has the right wavelength that 'fits' inside, bounces on average about 2000 times back-and-forth, before it escapes. We then talk about resonant light that resonates in the cavity.

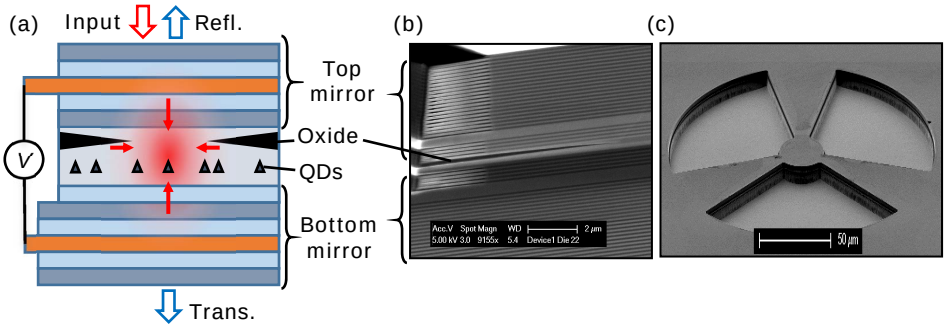

Figure 9.5: The microcavity. (a) Schematic image. Incident light (Input) is confined between the top and bottom mirrors and in the transverse direction by the oxide layer, before it is reflected or transmitted. Electrical contacts are used to apply a voltage V that controls the charge in the QDs. Electron microscope images of (b) a cross-section and (c) a top view of a micropillar (with a diameter of 30 μm).

Figure 9.5 (a) shows a schematic of a microcavity and Figure 9.5 (b,c) display cross-section and top view electron microscope images. Such a microcavity consists of two mirrors that confine the light in the out-of-plane direction. These mirrors are composed of many reflecting layers (composed of GaAs and Al(Aluminium)GaAs) which together act as an extremely good mirror, with a typical reflectivity $> 99.95\%$. To confine light also in the in-plane direction, first a small pillar is etched and, next, one of the layers in the center of the pillar is oxidized. Because the oxide has a lower refractive index than the unoxidized material, and light prefers high refractive index material, this way light is confined by the mirrors and the oxide layer into a small 'box'. The length of the oxide layer is essential; if the oxide layer has not penetrated far enough to the center of the pillar than the cavity is too large and the coupling between QDs and light is not strong enough. However, if the oxide has penetrated too far, the electrical contacts no longer function and neither do the QDs in that case.

The special property of a QD in a cavity is that a single QD, which absorbs in free space only a tiny fraction of the incident light, can now cause a photon, that would otherwise be transmitted by the cavity, to be (nearly) completely reflected. To explain the working mechanism of this process, we start with the interactions that can in general take place between light and matter. In Figure 9.6 (a) three processes are shown: (I) an incident photon does not interact, (II) a photon is absorbed, the QD is excited, and a photon is after some time spontaneously emitted, and (III) the photon is delayed by the QD and experiences a phase change, without being absorbed. This last process can be compared with light that transverses glass: the light is not absorbed, but does 'feel' the glass (SiO_2) molecules which causes it be slowed down, a process that is also described using a refractive index.

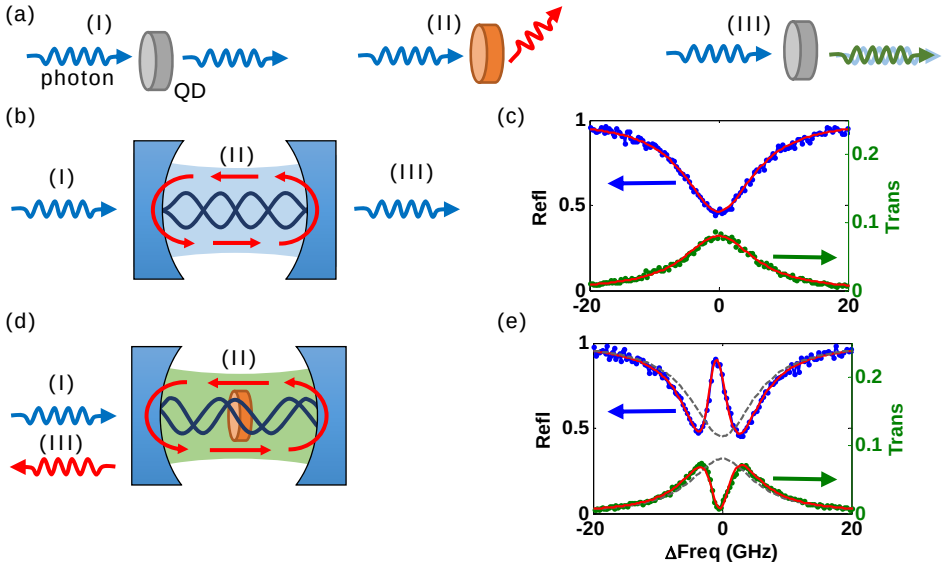

Figure 9.6: A QD in a microcavity. (a) An incident photon and a QD show three kinds of interactions: (I) no interaction, (II) absorption followed by emission, and (III) a phase change, or retardation, of the photon. (b) In an empty cavity, resonant light fits for an integer number of half wavelengths and is transmitted. (c) This results in a dip in the reflection spectrum and a peak in the transmission spectrum of the cavity. (d) In a cavity with a coupled QD a phase change is induced and the ($\Delta f = 0$ GHz) light is no longer resonant causing it to now be reflected. (e) In measurements a peak in the reflection dip and a dip in the transmission peak are now visible.

Figure 9.6 (b) shows schematically the case where light enters an empty cavity. Resonant light fits an integer number of half wavelengths in the cavity and, due to constructive interference, it is transmitted. Figure 9.6 (c) shows the corresponding measurements: along the horizontal axis the frequency of the incident light is scanned,

and along the vertical axis we see that the reflectivity has a minimum and the transmittivity has a maximum at the cavity resonance ($\Delta f = 0$ GHz). Figure 9.6 (d) shows what happens when a single QD is coupled to the cavity. A small portion of the light is now absorbed, but most of the light undergoes a delay and phase change that now prevents it from still 'fitting' inside the cavity. This causes the light to be no longer transmitted through the cavity, but instead to be reflected. Measurements in Fig. 9.6 (e) show this effect and are one of the highlights of the work that is presented in this thesis.

This thesis consists of 9 Chapters with roughly the following content:

Chapter 1 is a general introduction to the research field. A general motivation is presented and the most important theoretical concepts are explained. Also, a comparison is made between several experimental systems that have been realized to study (artificial) atoms coupled to photons in cavities, including our own system.

Chapter 2 is a more technical introduction. Details are displayed of the new cryostat that was developed during my dissertation, the optical measurement techniques, the design and fabrication of the samples, and characterization measurements on single QDs.

Chapter 3, 4 and 5 elaborate on the optimization of the oxide layer, which is critical for the proper functioning of the microcavities. In Chapter 3 a technique is presented that enables the real time monitoring of the oxidation process. In Chapter 4 it is demonstrated that the oxidation can also be well controlled in small steps. For these experiments we designed and constructed in Leiden a new oxidation furnace in collaboration with the Fine Mechanical Department. In Chapter 5 it is shown how the shape of the oxide layer can be controlled, and that the optical properties of the microcavities are closely related. This made it possible for us to realize microcavities that are polarization degenerate, which means that every incident polarization is preserved in the cavity. This property is essential for experiments presented in Chapter 6, 7 and 8.

In Chapter 6 charge neutral and singly charged QDs in microcavities are investigated. The optical transitions have different polarization properties that we can now, using the microcavities, clearly observe. Also, these studies enable us to study the coherent and incoherent dynamics of the QDs.

In Chapter 7 a memory effect is described in our system. Light that is coupled into the cavity also induces the excitation of other charges outside of the QDs, which are then trapped by the oxide layer. These trapped charges influence the energy of the QD transition and give rise to hysteresis and other effects. This behavior is explained using simulations and time-resolved measurements.

In Chapter 8 a novel technique is demonstrated to study the coherence and phase of light that is transmitted through the QD-cavity system. If light is scattered by a QD, the coherence of this light contains information on this interaction. We hope to use this information to further improve the properties of the QDs in the future. Also, the cavity and the QD induce a phase shift of the transmitted light, which we can observe with our technique.

Chapter 9 contains an outlook for further experiments and sample improvements, based on the understanding obtained in this thesis. For future research, especially

the coherent properties of charged QDs need to be improved, which is possible using the new characterization techniques that have been developed.

Samenvatting

Dit proefschrift beschrijft onderzoek naar 'quantum dots' (QD's, in het Nederlands vertaald als 'kwantum punten'), in optische trilholtes. In deze samenvatting zal worden uitgelegd hoe QD's en optische trilholtes werken, en wat samengevat de resultaten zijn die tijdens mijn promotieonderzoek behaald zijn en in dit proefschrift gepresenteerd worden.

QD's zijn hele kleine 3D structuren van een halfgeleidermateriaal, Indium Arsenide (InAs), dat is omgeven door een ander halfgeleidermateriaal, Gallium Arsenide (GaAs). Figuur 9.7 (a) laat een elektronenmicroscoop afbeelding van de doorsnede van een QD zien. Ze worden spontaan gevormd door eerst InAs op een GaAs substraat te deponeren, waardoor 'druppeltjes' ontstaan. Vervolgens worden deze InAs druppels weer met GaAs bedekt. QD's bestaan uit slechts $10.000 - 100.000$ afzonderlijke In en As atomen en hebben een pannenkoekachtige vorm met een diameter van ~ 40 nm (een nm is gelijk aan 10^{-9} meter) en een hoogte van $1 - 2$ nm. InAs heeft als eigenschap dat ladingen die zich erin bevinden een lagere energie hebben dan ladingen in het omringende GaAs, en er dus niet zomaar uit kunnen wegspringen. Verder zijn QD's optisch actief, wat inhoudt dat ze een lichtdeeltje, foton genaamd, kunnen absorberen en vervolgens kunnen uitzenden. Dit proces wordt schematisch weer gegeven in Fig. 9.7 (b). Deze optische overgangen zijn spectraal scherp, wat inhoudt

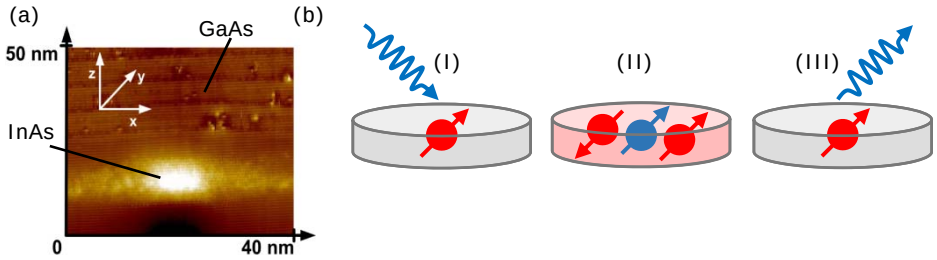

Figuur 9.7: (a) Elektronenmicroscoop afbeelding van een InAs quantum dot (QD) die in een GaAs kristal is ingebouwd. (b) Schematische weergave van de absorptie en emissie van een foton door een QD geladen met een enkel elektron (rode bolletje). Een foton valt (I) op de QD, creëert (II) een elektron en elektrongat (blauw bolletje) paar, en wordt (III) vervolgens weer uitgezonden.

dat alleen fotonen met een bepaalde golflengte (oftewel kleur) een interactie kunnen aangaan; QD's worden daarom ook wel kunstmatige atomen genoemd.

De QD's worden door onze onderzoeksgroep zodanig in een structuur gegroeid, dat de totale lading in de QD gecontroleerd kan worden zo dat er slechts één enkel elektron in zit. Een opgesloten elektron gedraagt zich volgens de wetten van de

kwantummechanica en is interessant omdat het kan dienen als een bouwsteen voor een nieuw soort 'kwantum' computer. Deze zou gebruik kunnen maken van speciale kwantummechanische eigenschappen en hierdoor bepaalde berekeningen veel sneller kunnen uitvoeren dan een 'klassieke' computer. Verder is onderzoek naar QD's gedreven door nieuwsgierigheid; omdat QD's zich gedragen volgens de wetten van de kwantummechanica, is het een spannende uitdaging om te kijken in hoeverre voorspellingen van deze wetten ook daadwerkelijk in een laboratorium gemeten kunnen worden.

QD's bestuderen, uitlezen, en met elkaar koppelen kan door middel van enkele fotonen. Echter, de interactie waarschijnlijkheid tussen licht en een QD is erg klein (typisch maar enkele procenten), evenals de kans dat een uitgezonden foton wordt opgevangen. Dit maakt experimenten erg lastig, maar ook met name toepassingen. De oplossing hiervoor is om hele kleine optische trilholtes te gebruiken (Engels: 'microcavities'). Licht dat in de trilholte valt en de juiste golflengte heeft waardoor het erin past, 'stuitert' in ons experiment gemiddeld ongeveer 2000 keer heen en weer, voordat het er doorheen gaat. We spreken dan van resonant licht of licht dat resoneert in de trilholte.

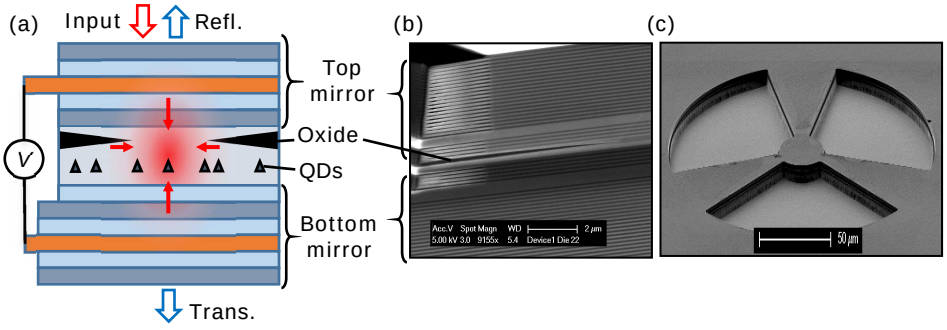

Figuur 9.8: Microscopische trilholte (microcavity). (a) schematische weergave. Invallend licht (Input) wordt ingevangen tussen de top en bodem spiegels en wordt in de dwarsrichting opgesloten door de oxidelaag, voordat het reflecteert of transmitteert. Met elektrische contacten wordt een spanning V aangelegd om de lading in de QD's te controleren. Elektronenmicroscoop afbeeldingen van (b) een doorsnede en (c) een bovenaanzicht van de centrale pillaar (diameter 30 μm).

Figuur 9.8 (a) toont een schematische afbeelding van een trilholte en Figuur 9.8 (b,c) laten elektronenmicroscoop afbeeldingen zien van een doorsnede en een bovenaanzicht. Zo'n trilholte bestaat ten eerste uit twee spiegels waartussen licht kan worden opgesloten. Deze spiegels bestaan uit heel veel reflecterende lagen (bestaand uit GaAs en Al(Aluminium)GaAs) die gezamenlijk als een hele goede spiegel functioneren, met een typische reflectiviteit $> 99.95\%$. Om licht ook in het vlak tussen de spiegels op te sluiten, wordt er eerst een pillaartje geëtst, en wordt daarna een van de lagen in het midden van de pilaar geoxideerd. Omdat het oxide een lagere brekingsindex heeft dan het ongeoxideerde materiaal, en licht een hoog brekingsindex

materiaal prefereert, wordt op deze manier het licht tussen de twee spiegels en de oxide laag in een doosje opgesloten. De lengte van de oxide laag is essentieel; als de laag niet ver genoeg geoxideerd is dan is de trilholte te groot en is de koppeling tussen QD's en licht niet sterk genoeg. Echter, als de laag te ver door geoxideerd is dan werken de elektrische contacten en daarmee de QD's niet.

Het bijzondere van een QD in een trilholte is dat één enkele QD, die in de vrije ruimte slechts een kleine fractie van het licht kan absorberen, er voor kan zorgen dat een foton dat anders door de trilholte zou worden doorgelaten, nu (bijna) volledig wordt gereflecteerd. Om de werking van dit proces uit te leggen, beginnen wij bij de interacties die tussen licht en materie kunnen plaatsvinden. In Figuur 9.9 (a) worden drie processen weer gegeven: (I) een invallend foton heeft geen interactie, (II) een foton wordt geabsorbeerd, de QD wordt aangeslagen, en een foton wordt na spontaan verval opnieuw uitgezonden, en (III) het foton wordt vertraagd door de QD en ondergaat een faseverandering, zonder dat het wordt geabsorbeerd. Dit laatste proces kan vergeleken worden met licht dat door glas valt: het licht wordt niet geabsorbeerd, maar 'voelt' wel de glas (SiO_2) moleculen en wordt daardoor vertraagd, een proces dat ook wel beschreven wordt met een brekingsindex.

Figuur 9.9 (b) geeft schematisch het proces weer van licht dat op een lege trilholte valt. Resonerend licht past een geheel aantal halve golflentes in de trilholte en wordt door constructieve interferentie getransmitteerd. Figuur 9.9 (c) laat de bijbehorende metingen zien: langs de horizontale as wordt de frequentie van het ingekoppelde licht veranderd, en langs de verticale as zien we dat de reflectie een minimum heeft en de transmissie een maximum bij de trilholte resonantie ($\Delta f = 0$ GHz). Figuur 9.9 (d) toont wat er gebeurt als er één QD aan de trilholte gekoppeld wordt. Een klein deel van het licht wordt nu geabsorbeerd, maar het meeste licht ondergaat een vertraging en faseverandering waardoor het niet meer in de trilholte 'past'. Dit zorgt ervoor dat het licht niet langer door de trilholte wordt getransmitteerd, maar in plaats daarvan gereflecteerd wordt. Metingen in Fig. 9.9 (e) laten dit effect zien en zijn een van de hoogtepunten van het werk dat wordt beschreven in dit proefschrift.

Dit proefschrift bestaat uit 9 hoofstukken met ruwweg de volgende inhoud:

Hoofdstuk 1 is een algemene introductie van het onderzoeksveld. Een algemene motivatie wordt gepresenteerd en de belangrijkste theoretische concepten worden uitgelegd. Ook wordt een vergelijking gemaakt tussen de verschillende soorten experimentele systemen die zijn ontwikkeld om (kunstmatige) atomen aan fotonen in trilholtes te koppelen, inclusief ons systeem.

Hoofdstuk 2 is een meer technische introductie. Hierin worden details gegeven over de nieuwe cryostaat die ontwikkeld is tijdens mijn promotie, de optische meettechnieken, het ontwerpen en ontwikkelen van de samples, en metingen aan enkele QD's.

Hoofdstuk 3, 4 en 5 gaan over het optimaliseren van de oxidelaag, welke kritiek is voor het goed functioneren van de trilholtes. In Hoofdstuk 3 wordt een techniek gepresenteerd waarmee het oxidatieproces bijna in real time gevolgd kan worden. In Hoofdstuk 4 wordt aangetoond dat de oxidatie ook gecontroleerd in kleine stapjes kan worden gedaan. Voor deze experimenten hebben we in Leiden een nieuw oxidatie oventje ontworpen en gebouwd in samenwerking met de Fijn Mechanische Dienst. In

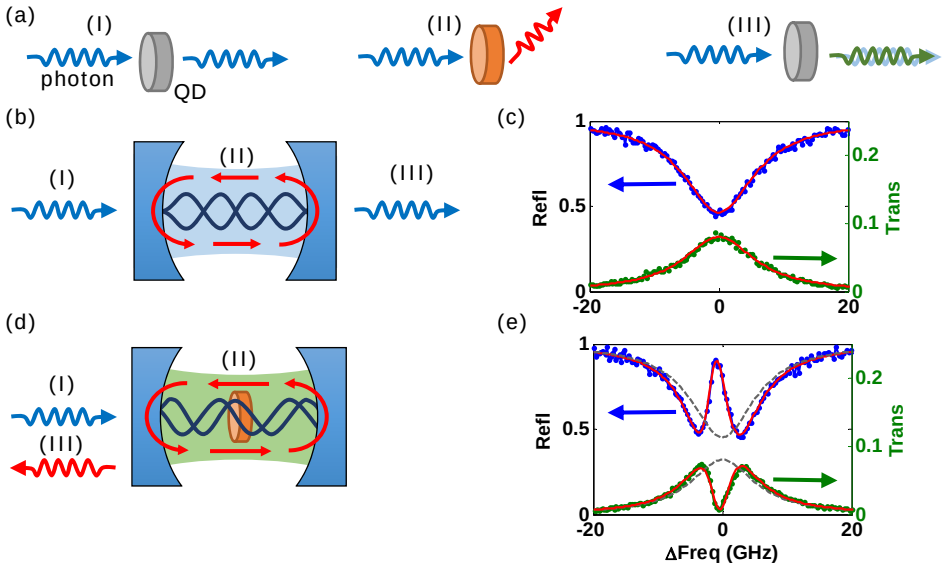

Figuur 9.9: Een QD in een trilholte. Als een foton op een QD valt kunnen er ruwweg drie processen optreden: (I) geen interactie, (II) absorptie gevolgd door emissie, en (III) een fase verandering, of vertraging, van het licht. (b) In een lege trilholte passen er voor resonerend licht een geheel aantal halve golflengtes in de trilholte en wordt het getransmitteerd. (c) Dit resulteert in een dip in de reflectie en een piek in de transmissie van deze trilholte. (d) In een trilholte met een gekoppelde QD wordt een fase verandering geïnduceerd en is het ($\Delta f = 0$ GHz) licht niet langer resonant waardoor het nu gereflecteerd wordt. (e) In metingen is dit zichtbaar als een piek in de reflectie dip en een dip in de transmissie piek.

Hoofdstuk 5 laten we zien hoe de vorm van de oxidelaag gecontroleerd kan worden, en dat de optische eigenschappen van de trilholte hier nauw mee samen hangen. Hierdoor lukt het ons om trilholtes te ontwikkelen die polarisatie ontaard zijn, dat wil zeggen dat elke inkomende polarisatie behouden blijft in de trilholte. Deze eigenschap is essentieel voor de experimenten in Hoofdstukken 6, 7 en 8.

In Hoofdstuk 6 worden ongeladen en enkel–geladen QD's in trilholtes onderzocht. De optische overgangen hebben verschillende polarisatie eigenschappen die wij nu, door middel van de trilholtes, heel duidelijk kunnen waarnemen. Ook kunnen wij door deze studies de interne coherente of incoherente dynamica van de QD's bestuderen.

In Hoofdstuk 7 wordt een geheugeneffect in ons system beschreven. Door licht in de trilholte te koppelen vinden er ook excitaties plaats van andere ladingen buiten de QD's die door de oxide laag gevangen worden. Deze ladingen beïnvloeden de energie van de QD overgangen en leiden tot onder andere hysterese effecten. Dit gedrag kan met simulaties en door middel van tijdsopgeloste metingen verklaard worden.

In Hoofdstuk 8 wordt een techniek gedemonstreerd waarmee we de coherentie en fase van licht kunnen bepalen dat door de trilholte is getransmitteerd. Als het licht door een QD verstrooid wordt, dan bevat de coherentie van dit licht informatie over

deze wisselwerking. We willen deze informatie gebruiken om in de toekomst de QD eigenschappen te verbeteren. Ook veroorzaken de trilholte en QD een fase verandering die waargenomen kan worden.

Hoofdstuk 9 is een vooruitblik met een vooruitzicht voor verdere metingen en sample verbeteringen. Voor vervolgonderzoek moet met name de coherentie eigenschappen van geladen QD's worden verbeterd. Hiervoor zijn in dit proefschrift belangrijke inzichten en karakterisatie technieken ontwikkeld.

Curriculum Vitæ

Morten Bakker was born on the 1st of February 1987 in Groningen. He lived in Muscat (Oman) from 1987-1993, in Copenhagen (Denmark) from 1993-1996, and moved to Zuidlaren in the Netherlands in 1996. He graduated in 2005 from the Maartenscollege high school in Haren with a Science and Technology (NT) profile and the additional subjects Latin and Geography. He finished on the 5th place in the National Geography Olympiad in 2005. He went on to study Applied Physics at the University of Groningen in 2005 and obtained his BSc cum laude in 2008. His BSc final project was on 'Heat transport measurements in spin-ladder compounds', with Marian Otter and prof. Paul van Loosdrecht. During his bachelor studies, he spent 10 months in 2007-2008 studying various subjects at the National University of Singapore. In 2008 he started on the top master programme in Nanoscience at the Zernike Institute for Advanced Materials at the University of Groningen. During this time, he performed a summer research internship project in the 'Superconducting circuits and quantum computation' group with dr. Will Oliver and prof. Terry Orlando at MIT in Boston (USA) in 2009. He then performed his MSc thesis project 'Electromagnetically induced transparency with electron spins bound to neutral Si donors in GaAs' with Maksym Sladkov and prof. Caspar van der Wal and graduated cum laude in 2010. He joined the Quantum Optics at the University of Leiden on the 1st of October 2010 to work on quantum dots in microcavities with dr. Martin van Exter and prof. Dirk Bouwmeester.

List of publications

1. M. Sladkov, A. U. Chaubal, M. P. Bakker, A. R. Onur, D. Reuter, A. D. Wieck, and C. H. van der Wal, "Electromagnetically induced transparency with an ensemble of donor-bound electron spins in a semiconductor," *Phys. Rev. B* **82**, 121308(R) (2010)

2. M. Sladkov, M. P. Bakker, A. U. Chaubal, D. Reuter, A. D. Wieck, and C. H. van der Wal, "Polarization-preserving confocal microscope for optical experiments in a dilution refrigerator with high magnetic field," *Rev. Sci. Instrum.* **82**, 043105 (2011)

3. J. Hagemeier, C. Bonato, T.-A. Truong, H. Kim, G. J. Beirne, M. P. Bakker, M. P. van Exter, Y. Luo, P. M. Petroff, and D. Bouwmeester, "H1 photonic crystal cavities for hybrid quantum information protocols," *Opt. Exp.* **20**, no. 22, pp. 24714-24726 (2012)

4. M. P. Bakker, D. J. Suntrup III, H. Snijders, T.-A. Truong, P. M. Petroff, M. P. van Exter and D. Bouwmeester, "Monitoring the formation of oxide apertures in micropillar cavities," *Appl. Phys. Lett.* **102**, 101109 (2013)

5. M. P. Bakker, D. J. Suntrup III, H. Snijders, T.-A. Truong, P. M. Petroff, D. Bouwmeester and M. P. van Exter, "Fine tuning of micropillar cavity modes through repetitive oxidations," *Opt. Lett.* **38**, pp. 3308-3311 (2013)

6. M. P. Bakker, A. V. Barve, A. Zhan, L. A. Coldren, M. P. van Exter and D. Bouwmeester, "Polarization degenerate micropillars fabricated by designing elliptical oxide apertures," *Appl. Phys. Lett.* **104**, 151109 (2014)

7. M. P. Bakker, A. V. Barve, T. Ruytenberg, W. Löffler, L. A. Coldren, D. Bouwmeester, and M. P. van Exter, "Polarization degenerate solid-state cavity quantum electrodynamics," *Phys. Rev. B* **91**, 115319 (2015)

8. M. P. Bakker, T. Ruytenberg, W. Löffler, A. V. Barve, L. A. Coldren, M. P. van Exter, and D. Bouwmeester, "Quantum dot nonlinearity through cavity-enhanced feedback with a charge memory," *submitted to Phys. Rev. B*

9. M. P. Bakker, H. Snijders, W. Löffler, A. V. Barve, L. A. Coldren, D. Bouwmeester, and M. P. van Exter, "Homodyne detection of coherence and phase shift of a quantum dot in a cavity," *submitted to Opt. Lett.*

Acknowledgement

During my PhD I have had the pleasure and joy to work together with a lot of people, whom I would like to gratefully acknowledge.

I would like to thank Dirk Bouwmeester for being my promotor and the principal investigator of the research collaboration between the University of Leiden and UC Santa Barbara. Martin van Exter I thank for being my co-promotor. His extensive knowledge, insights, and enthusiasm to always help were invaluable and also a great inspiration to me. I would also like to thank the other senior staff members in the QO group Michiel de Dood, Gerard Nienhuis and Han Woerdman, for many useful advices and comments throughout my PhD. Michiels advice on among others sourcemeters was truly priceless.

The samples used in Chapters 5-9 were realized with great care and professionalism by Ajit Barve in the group of Larry Coldren in UCSB, whom I owe a very big thanks.

During my PhD I have had the enjoyment, and also great benefit, of supervising three students. Henk Snijders performed his bachelor research project on realizing the new oxidation furnace and oxidation monitoring technique in 2012, which directly lead to Chapters 3 and 4. Later in 2014, he rejoined the group as a PhD student, and made large contributions to among others Chapter 8. Ajan Ramachandran visited us from India in 2013 and worked on the first low temperature sample characterizations with the new cryostat system. From these we learned a lot in order to improve future samples and getting the setup to work nicely without vibrations. Thomas Ruytenberg performed his master research project on 'The One QD' in 2014. During an uppermost productive time we were able to set up many new measurements, increased the setups complexity by an order of magnitude, and obtained many results that directly lead to Chapters 6 and 7, and preliminary work that lead to results in Chapters 8 and 9. And a nice poster prize in Arnemuiden.

I owe much gratitude to Wolfgang Löffler for all his support, basically from the beginning to the end of my PhD. His knowledge of a wide range of topics, and his enthusiasm to help and share his ideas, are a great example to me. Later, after he 'rejoined' the group, we had many many discussions and he made large contributions to the work presented in Chapters 5-9. Cristian Bonato I would like to thank for among others learning me a lot on optics and cryogenics when I just started. All the other current and former members of the Quantum Optics group I thank for being part of such a great place to work. The many seminars, lunch meetings, social activities and coffee breaks provided a truly inspiring academic climate.

I studied at the Zernike Institute at the University of Groningen which provided me with both much knowledge, but also inspiration to continue with PhD research. I have especially good memories on my time working in the Physics of Nanodevices group with Maksym Sladkov and Caspar van der Wal, and I would like to thank

Caspar for also being a great source of inspiration throughout my PhD.

I enjoyed much and very professional support from the Fine Mechanical Department. I would like to thank Arjen Geluk and Ewie de Kuyper for always being very supportive and coming up with good plans on how to tackle the various challenges. Gijs Verdoes realized the oxidation monitoring furnace and the cryogenic setup in a very professional way, and is a great person to work with. He made, in the most literal sense, this thesis possible. For the many 'quick' services, and the many other not so 'quick' problems, I would like to thank Fred Schenkel, Harmen van der Meer, Emiel Wiegers, and all the other FMD members. I would like to thank Marcel Hesselberth and Daan Boltje for their help in the 6^{th} floor cleanroom. I would like to thank René Overgauw, Arno van Amersfoort, Raymond Koehler, Peter van Veldhuizen and all the other members of the Electronics Department for their professional and great help. Henriëtte van Leeuwen I would like to thank for all the secretarial support.

Finally, I would like to thank my parents, my sister Lene, and my other family members and friends for their constant love and support throughout my PhD.